

Characterization of Reflection Seismic Systems in Glaciology by Data Analysis of the PALAOA-Observatory

Masterarbeit im Studiengang Geowissenschaften

Fachbereich Geowissenschaften

Universität Bremen

angefertigt am

Alfred-Wegener-Institut für Polar- und Meeresforschung

von

Maximillian Grahs

Bremen, 2020

1. Gutachter

Prof. Dr. Olaf Eisen

2. Gutachter

PD Dr. Karsten Gohl

Fachbetreuer:

Dr. Coen Hofstede

Abstract

With the critically intensifying global climate change the scientific interest in the Arctic and Antarctic increases continuously. Polar ice sheets are in a constant dynamic state and flow, depending on conditions of the subglacial bed. Information about the subglacial bed are important for estimating the ice sheet evolution and climate modelling.

Seismic observations are basic methods to estimate spatial and physical properties of the subglacial bed. Different parameters that depend on the material and system characteristics like the attenuation, reflection coefficient and source amplitude drive the behaviour of elastic waves and furthermore the assessment of the results in glaciology. This leads to large uncertainties in defining the subglacial material. The PALAOA observatory is a set of calibrated hydrophones placed within the water column beneath the Ekström Ice Shelf, Antarctica. Its main purpose is to identify the underwater sea life soundscape, but can also be used for recording seismic shots triggered at the ice surface. The unique location of the hydrophones provides new opportunities of observing seismic signals, due to different ray paths in comparison to conventional methods.

24 shots triggered by a Vibroseis truck at the ice surface at 6 different locations are analysed. Ray paths and travel times of four signals of various reflections at each shot point are calculated and identified in the seismograms. The analysis of amplitudes of different signals in correlation with known properties of ice and water aims to provide estimations about attenuation of seismic waves depending on the shot point distance.

This thesis presents a new method for analysing seismic data. The results highlight, that the time delay between the first signal arrival and the highest amplitudes (main signal) of single shots increases with an increasing shot distance. This is caused by sp-converted waves at the ice – water interface. Amplitudes show a strong decrease with increasing offsets. Several uncertainties complicate the seismogram interpretation which are discussed. Finally this thesis depicts in a first approach, how the usage of hydrophones could complement methods in observations of seismic data in glaciology and further constitutes the basis of prospective future studies.

Kurzfassung

Der während der letzten Dekaden sich intensivierende Klimawandel verstärkt das wissenschaftliche Interesse in das Verständnis polarer Regionen. Eisschilde in der Arktis und Antarktis fließen kontinuierlich in Abhängigkeit des sich darunter befindlichen Materials. Genaue Kenntnisse über subglaziale Fazies sind eine wichtige Grundlage vergangener und zukünftiger Eisschild- und Klimamodellierung.

Seismische Untersuchungen dienen der Analyse räumlicher und physikalischer Eigenschaften des Untergrundes. Kenngrößen wie Dämpfung, Reflektionskoeffizient und Quellamplitude beeinflussen die elastischen Wellen und führen besonders in der Glaziologie zu Ungenauigkeiten, die eine Materialbestimmung des Untergrundes erschweren. Bei der PALAOA-Horchstation handelt es sich um Hydrophone, die unterhalb des schwimmenden Ekström-Eisschelfs in der Antarktis in der Wassersäule platziert sind. Sie können neben der Observation mariner Lebewesen auch der Aufzeichnung der mittels an der Eisoberfläche durch Vibrationen ausgelösten seismischen Signale genutzt werden. Die besondere Lokation der Hydrophone ermöglicht eine neue Strategie zur Untersuchung seismischer Signale durch andere Laufwege im Vergleich zu herkömmlichen Methoden. Mittels Laufzeitberechnungen können einzelne Signale in den Seismogrammen zugeordnet werden. Die Messung der Amplituden verschiedener Signale liefert im Einklang mit bekannten physikalischen Eigenschaften von Eis und Wasser Informationen über die Dämpfung in Abhängigkeit des Laufweges.

Die Arbeit präsentiert eine neuartige Messmethode zur Analyse seismischer Studien. Die Untersuchung der Seismogramme weist einen zunehmenden Versatz zwischen Ersteinsatz und Hauptsignal mit starken Amplituden mit zunehmender Entfernung der Schusspunkte auf. Dies lässt sich mit der Ankunft von an der Eisunterkante sp-konvertierten Wellen erklären. Die Amplituden verschiedener Signale zeigen deutliche Abnahmen mit zunehmenden Laufwegen. Die durch die neuartigen Grundlagen entstehenden Komplexitäten werden mit der Arbeit aufgezeigt. Abschließend veranschaulicht die Arbeit den möglichen Nutzen der Hydrophone als vielversprechendes Messelement und bildet die Grundlage neuer Studien.

Danksagung

An dieser Stelle möchte ich mich bei all denjenigen bedanken, die mich während der Masterarbeit unterstützt und mir diese ermöglicht haben.

Zunächst gilt mein Dank Herrn Prof. Dr. Olaf Eisen für die Bereitstellung des äußerst interessanten Themas, für die Begutachtung der Arbeit sowie die schnelle Beantwortung meiner Fragen.

Ebenso möchte ich mich bei Herrn PD Dr. Karsten Gohl bedanken, der die Zweitprüfung übernommen hat.

Ganz besonderer Dank gilt meinem Betreuer Herrn Dr. Coen Hofstede, der mich während des gesamten Bearbeitungszeitraums unterstützt hat und stets für Fragen bereit stand. Ebenso stand er in häufigem Kontakt mit weiteren Mitarbeitern, um beispielsweise das Prozessingproblem mit Paradigm zu beheben, oder offene Fragestellungen zu beantworten.

Weiterhin möchte ich mich ganz herzlich bei meiner Familie bedanken, sowie bei meinen Freunden: Jerry, Yannis, Cedric, Kai und Andi, die nicht nur ein offenes Ohr für Fragen bezüglich der Arbeit hatten, sondern auch stets für die notwendige Ablenkung sorgten. Danke euch!

Außerdem gilt ganz besonderer Dank an Judith, die mich während der gesamten Masterarbeit unterstützt und ermutigt hat.

Ich danke euch allen ganz herzlich.

Acknowledgement

**The author would like to thank Emerson E&P Software, Emerson Automation Solutions,
for providing licenses for the seismic software Paradigm in the scope of the Emerson
Academic Program**

Erklärung gem. § 10 Abs. 11 Allg. Teil d. Master-PO vom 27.10.2010

Ich versichere hiermit, dass ich meine Masterarbeit selbständig verfasst und keine anderen als die angegebenen Quellen und Hilfsmittel benutzt habe. Wörtliche oder dem Sinn nach aus anderen Werken entnommene Stellen sind unter Angabe der Quellen kenntlich gemacht.

Die Arbeit wurde nicht in einem anderen Prüfungsverfahren eingereicht.

Weiterhin erkläre ich, dass die Masterarbeit in unveränderter Fassung der Öffentlichkeit zur Verfügung / ~~nicht zur Verfügung~~* gestellt werden kann. *Zutreffendes bitte markieren

A handwritten signature in black ink, appearing to be 'A. Pauls', written over a horizontal line.

Bremen, 13.05.2020

Ort, Datum

Unterschrift

Table of Contents

1. Introduction	1
1.1. Structure of ice sheets and ice shelves	3
1.2. Densification from firn to ice	6
1.3. Seismics in glaciology – state of the art	7
1.4. Motivation and structure of the thesis	9
2. Theoretical background	11
2.1. Seismic waves	12
2.1.1. Body waves	12
2.1.2. Surface waves	13
2.2. Wave propagation characteristics	14
2.3. Seismic source	18
2.3.1. Vibroseis signal	18
2.3.2. Cross-correlation	20
2.4. Receivers	21
2.4.1. Surface geophones	21
2.4.2. PALAOA hydrophone	22
3. Database and Methodology	23
3.1. Field site	23
3.2. Data acquisition and measurement setup	24
3.3. Travel time and ray path calculations	27
3.4. First arrival analysis	32
3.5. Amplitude calculation	33
4. Results	34
4.1. Timing correction and geometry	35
4.2. Ray paths and travel times	36
4.3. Event detection	40
4.4. Event Amplitudes	43
5. Discussion and Interpretation	50
5.1. Geometry and velocities	50
5.2. Seismogram interpretation	52
5.3. Error analysis of event arrival times	54
5.4. Amplitude interpretation	58
5.5. Critical discussion	61
6. Conclusion	63
7. Outlook	64
8. Bibliography	65
9. Appendix A	70

1. Introduction

With the critically intensifying global warming since the beginning of the pre-industrial era at the middle of the 19th century, the interest in scientific questions and observations of the polar regions increases constantly. Over this timespan, the average worldwide temperature rose by about 1.0 °C and it accelerates with an increasing rate especially during the last 30 years (IPCC Special Report on Global Warming; Masson-Delmotte et al., 2019). The evolution of the temperature differs depending on the location. It increased more than twice as much at the poles than on the global average within the last two decades (IPCC SROCC; Pörtner et al., 2019, in press). The polar ice sheets in the Arctic and Antarctic would not only cause a global sea level rise of about 65 m due to their immense size if they would melt (Cuffey and Paterson, 2010), but they would also indirectly impact the whole worldwide ecosystem. Because ice acts as a kind of mirror that reflects solar radiation back into the space, the energy and heat will not be absorbed in the atmosphere and the environment. If ice is melting, the mass changes its state of aggregation from brighter ice or snow to darker water. Whereas ice or snow-covered surfaces have a high albedo (a parameter that characterizes the strength of backscattering solar radiation) of 68-90%, water has an albedo of less 30-35 % so the ocean absorbs the radiation of the sun instead of reflecting it like ice or snow (Kishtawal, 2013). Less ice causes less backscattering and thus more heat is absorbed in the atmosphere, cryosphere and hydrosphere and that increases the temperature that furthermore decreases the ice covered areas so the processes amplify themselves.

Because polar regions are very important for the worldwide ecosystems, scientists of different specialisations like geophysicists, meteorologists, chemists etc. around the world perform local scientific campaigns for in situ (in direct, natural state) observations for a better understanding of the processes that drive the behaviour of ice sheets. All different aspects of the cryosphere have to be taken into account to connect the information and finally make assumptions of future ice sheet development and sea level rise. There are three kinds of the ice masses like inner ice sheets, ice shelves (floating part of the ice) or continental glaciers. Different properties affect the dynamic state of ice sheets like spatial distribution, mass balance, internal structures and the subglacial bed. Several methods are used to examine the most important physical parameters like snow accumulation rate, surface and basal melting, temperature and density profiles and further flow velocity and strain rates. Furthermore, in addition to the analysis of ice, the physical properties of the subglacial bed like basically spatial distribution, density, porosity, roughness and water content are exceedingly important, because the dynamic features of ice sheets are facilitated by sliding or motion at their beds or deformation of the ice above the subglacial bed (Smith and Murray, 2009). Because of the spatial extent of the East Antarctic ice sheets of more than 1000 kilometres in length and width and a thickness up to 4500 m

maximum (Lüthi et al., 2017), only point measurements by drilling are possible to reach direct contact to the subglacial bed. Boreholes are cost-intensive, time consuming and just give a local point information. However, they can provide a lot of detailed information that can be combined with geophysical methods.

Seismic is a geophysical method commonly used and based on the propagation of elastic waves. It is used to display and analyse the internal spatial structures and layering of englacial and subglacial material (Booth et al., 2013). A seismic source transmits elastic waves triggered by an Air-Gun offshore, in polar cases with an impulse source like explosives charges or with vibroseismic trucks (Vibroseis). The waves penetrate into the ground and be reflected at an interface of two different media. Geophones placed at the surface record the incoming seismic signals and provide information about the ground like its thickness or velocity. Due to a lack of specific quantitative knowledge about the effective source amplitude, attenuation and reflection coefficient of seismic campaigns on ice, scientists often make several assumptions that cause large uncertainties that prevent an accurate identification of the subglacial material (Holland and Anandakrishnan, 2009). Especially the attenuation of the waves within the ice is an important factor based on its sensitivity to lithology, anisotropy, fluid content, porosity and temperature (Peters et al., 2012).

The *Perennial Acoustic Observatory in the Antarctic Ocean* (PALAOA) Observatory now consists of two calibrated hydrophones that are arranged in the ocean cavity below the Ekström Ice Shelf in East Antarctica. After Kindermann et al., (2008) PALAOA contained originally four hydrophones but two of them are now defect. Since 2005 the hydrophones observe the underwater soundscape of marine sea life below the ice shelf (Kindermann et al., 2008). In 2010 seismic shots and Vibroseis sweeps were triggered on the ice surface that were recorded by the PALAOA hydrophone. By analysing the records of vibroseismic shots, only one way travel time downwards the hydrophone has to be examined. The aim of the thesis is to characterize the acoustic records of PALAOA by observing the amplitudes of different seismic events and further to quantify the source amplitude and the amount of the attenuation by traveling of the waves through the ice shelf. The amplitudes of several reflections will be compared with the results of the surface geophones, in dependence of an increasing offset. Finally the work aims to decrease the general uncertainties in seismic surveys in glaciology like the source amplitude and the attenuation of the seismic waves through the ice.

1.1. Structure of ice sheets and ice shelves

Fundamentals of glaciers

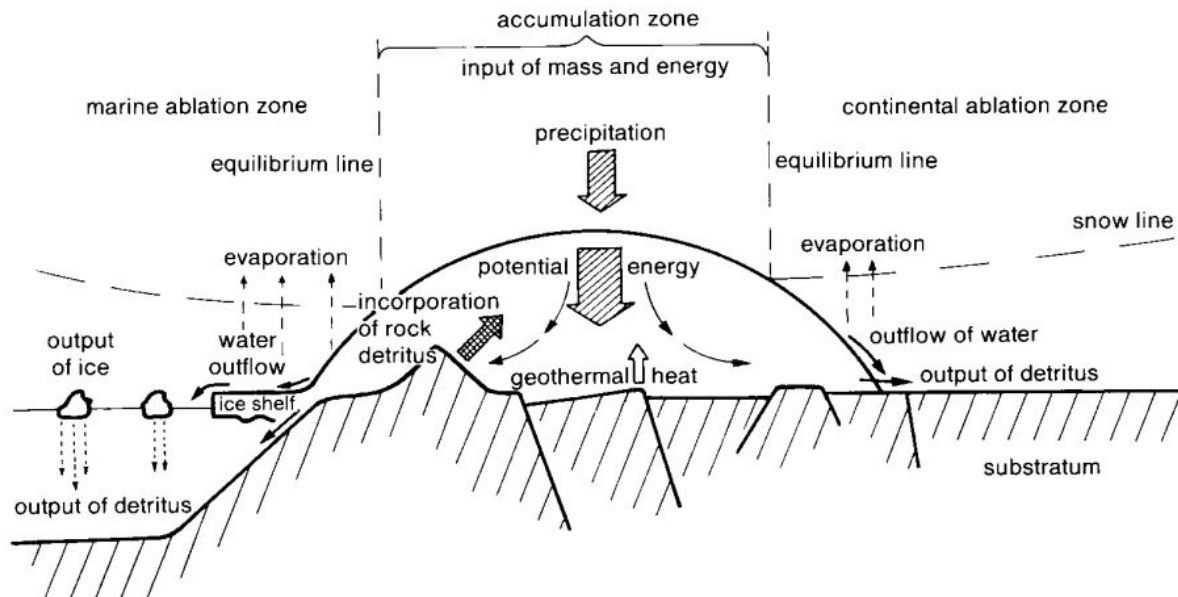


Figure 1: Sketch of different domains in an ice sheet (Brodzikowski and van Loon, 1990).

In the following discussion ice sheets and glaciers are described after Benn and Evans (2010). Glaciers can be divided into three main types: ice sheets and ice caps (unconstrained by topography), glaciers constrained by topography and ice shelves. Furthermore several subclasses like outlet glaciers, ice domes, valley glaciers etc. exist. Glaciers basically contain a mass gaining (accumulation zone) and a mass dispensing (ablation zone) area. They are divided by the equilibrium line of altitude (ELA) which position depend on the location and height of the glacier as well as climate and geographical factors. The accumulation zone has an annual average positive mass balance, so the snowfall or windblown snow as a form of precipitation adds more mass to the region as it is losing by surface and basal melting. The ELA marks the line where the annual accumulation is in equilibrium with the annual ablation. The accumulation zone is accordingly located at the inner and / or higher elevation part of the glacier or ice sheet (Figure 1) with extents for hundreds of kilometres in length and width and some kilometres in height (Kuhn, 1995). The ablation zone contains in the most cases the lower (and older) part of the glacier as well as the floating ice shelves. In the ablation zone the glacier loses mass. The distribution of the accumulation and ablation zone and finally its flow behaviour describe the dynamic state of the glacier (Cuffey and Paterson, 2010; Benn and Evans, 2010). The ice divides (ID) are boundaries with an opposing ice flow direction. Whereas the flow along the ice divide is zero, it is on either sides orientated in the opposite direction (Benn and Evans, 2010). The flow direction depends on the surface slope orientation and the

gravitational force. The ice flows from the ID towards the coast where the ice starts sliding in form of ice streams. When the ice streams pass the grounding line (the area that marks the boundary between grounded and floating ice) they become floating ice shelf. Ice shelves will be explained in detail in the following.

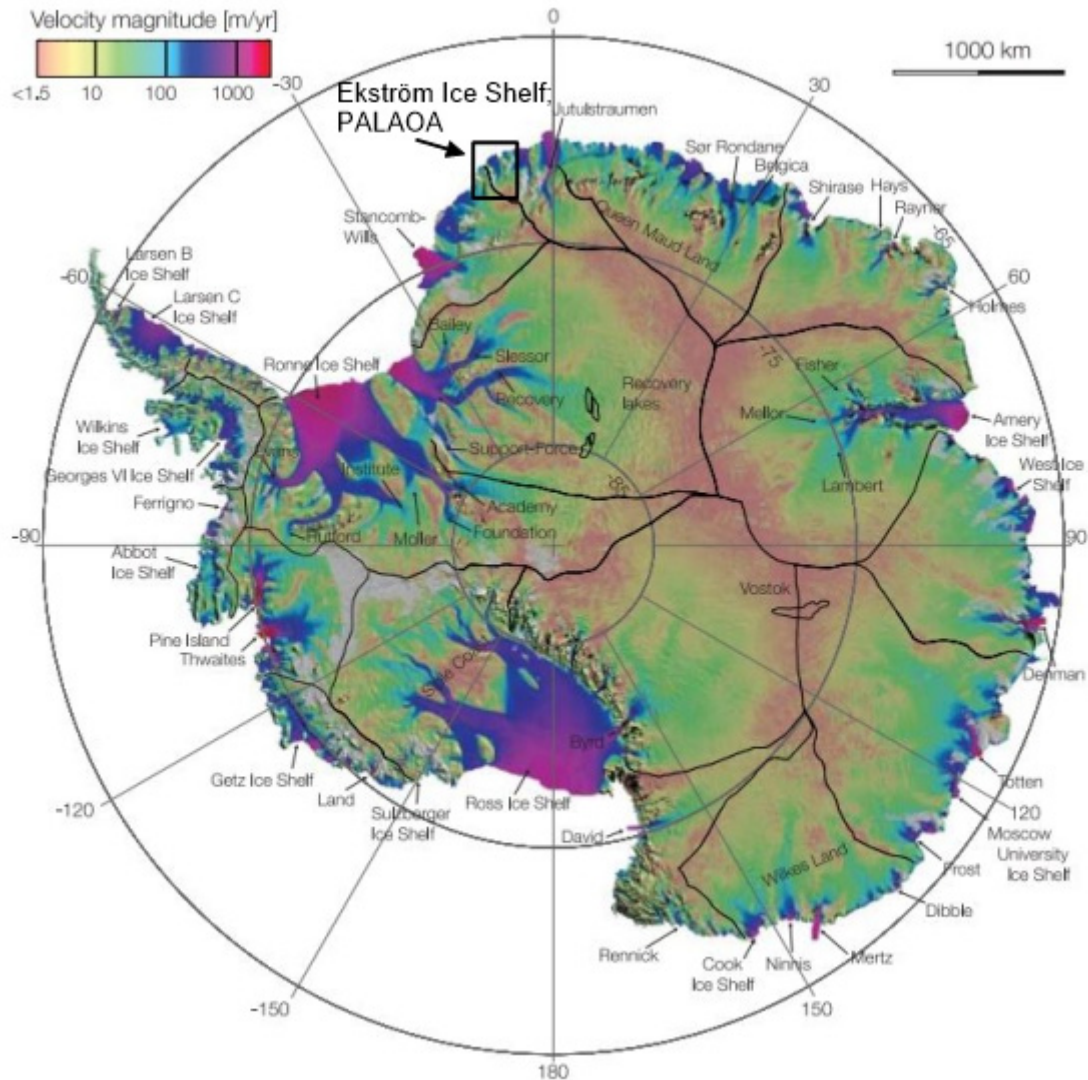


Figure 2: Map with flow velocities of the Antarctic ice sheets modified after by Rignot et al., (2011). Ice shelves at the surrounding edge of the continent show higher velocities than the inland ice sheets. Black lines mark ice divides. Ekström ice shelf and the location of PALAOA is mentioned in the black rectangle.

Ice Shelves

Ice shelves are floating ice masses and fringe about 74% of the Antarctic’s coastline (Hogg and Gudmundsson, 2017). They are the interacting part between the land ice and the ocean. As the ice is already floating and displacing water, it is calving or “break off”, so the loss of larger ice bergs or melting, does not directly affect the global sea level. Ice shelves act as a barrier that buttress the grounded ice masses located upstream (Hogg and Gudmundsson, 2017). Calving

of ice shelves causes an acceleration of grounded ice (Rignot et al., 2004) and thus increases the masses adding to the ocean that once again affect the global sea level. One example is the giant break off in 2017 of the new ice berg *A18* at the *Larsen C* ice shelf on the Antarctic Peninsula (Hogg and Gudmundsson, 2017).

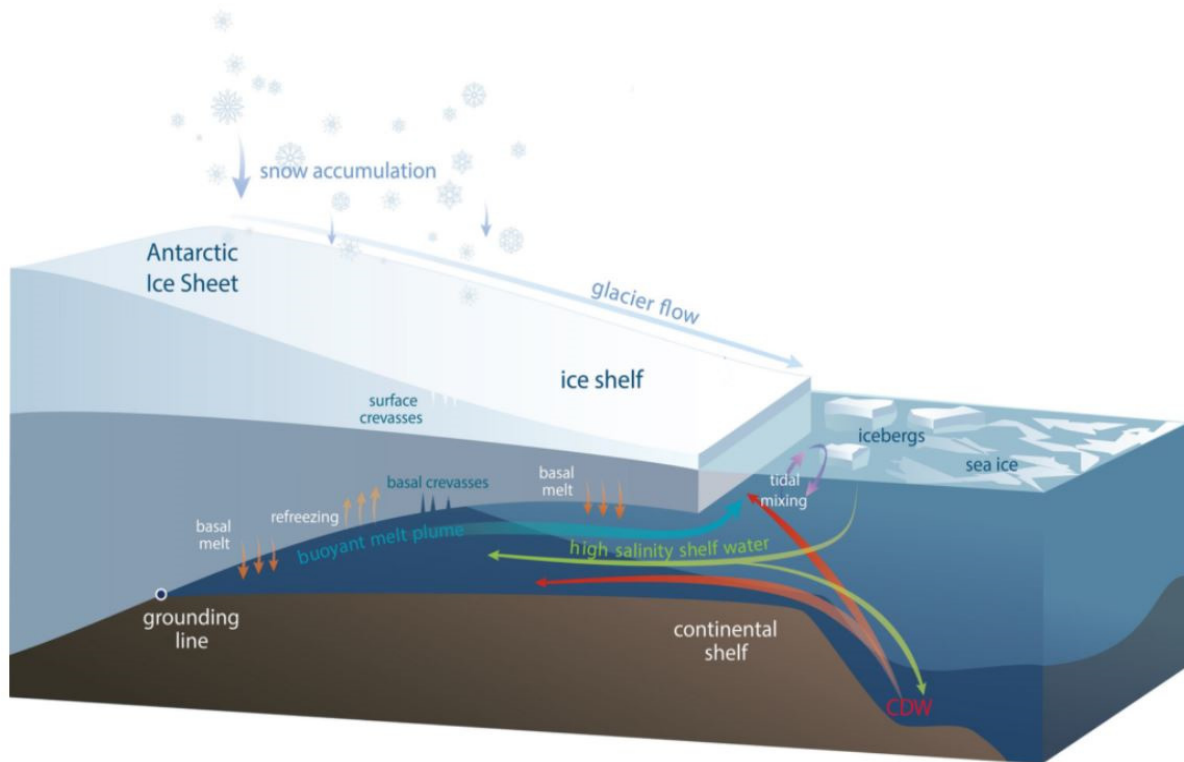


Figure 3: Sketch of an ice shelf with its state driving processes (modified after Padman et al., 2018).

Different processes at the surface and the base impact the state of ice shelves. Ice has fluid and elastic properties. The flow of ice can be described by internal deformation, basal sliding and soft bed deformation caused by dipping angles of the subglacial bed, basal melt and the gravitational force (Jiskoot, 2011). Several processes drive the effective anisotropy of the ice in ice shelves. The top layer consist of snow or ice crystals including a high amount of air particles in the pores. Furthermore fabric anisotropy is caused by the stress regime with higher depths (Diez et al., 2014). Melting and refreezing in the upper firn constitute different layers with changing sizes and formations of crystals up to the surface. Finally a consequent densification with depth builds a single layer with different densities and velocities that consequences will be explained later.

Percolating warmer ocean currents may melt ice at the base of the shelf. On the other hand the ice can refreeze water once again. Freezing and melting changes the volume of the ice shelf and furthermore the fresh water content and thus the ocean water conditions (Marshall and Speer,

2012). Surface rifts can be reinforced by basal and surface melting that are possibly followed by ice berg calving (Figure 3).

1.2. Densification from firn to ice

The surface of glaciers commonly consists of freshly fallen or wind transported snow. With adding mass and force by settled snow the densification and transformation process to ice begins. The porosity and content of air bubbles decreases with depth while the grain size increases (Cuffey and Paterson, 2010). Freshly fallen snow under calm conditions accumulates with a density of 50-200 kg/m³ due to its high porosity (Figure 4). Settled snow that survived one melt season without being transformed into ice is called firn (Cuffey and Paterson, 2010; Benn and Evans, 2010). Firn has a density of 430 – 800 kg/m³ (Cuffey and Paterson, 2010).

With increasing depth a gradual increase in density occurs up to the maximum density of pure ice that is about 917 kg/m³ (Benn and Evans, 2010) and thus lower than the density of water. After Herron and Langway (1980) and Arnaud et al. (2000) three main stages of densification exist during the transformation from firn to ice. The first and main stage occurs up to a “first critical density” of $\rho = 550$ kg/m³ (Figure 4). Getting to this density, the shape of the snow crystals changes from dendritic, hexagonal flakes to spheres by adhesion because of the principle of the state of smallest free energy (Arnaud et al., 2000; Benn and Evans, 2010). Further the almost perfect spheres slide at each other and decrease the porosity to 40% to a maximum random packing. At the second stage, the interconnected air bubbles get separated to single bubbles because of the continuative densification (Herron and Langway, 1980). The third stage, below the pore close-off zone, describes the mechanical compression of the separated and conserved air bubbles. At this stage the firn has a density of >830 kg/m³ and is called ice (Herron and Langway, 1980).

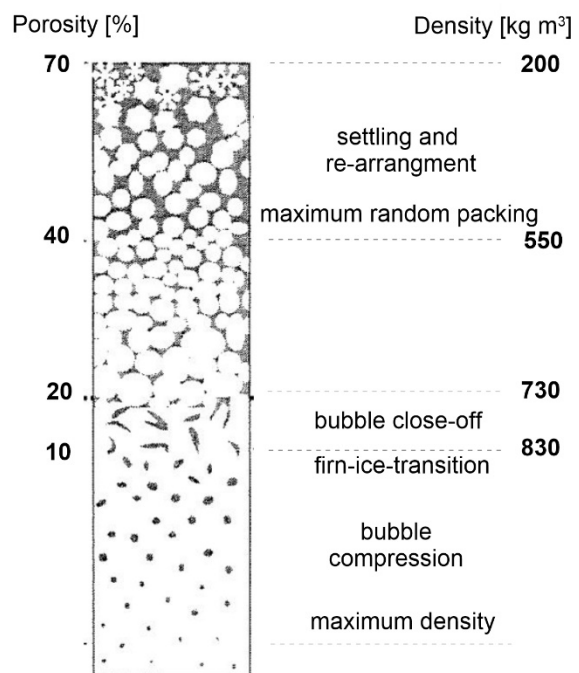


Figure 4: Different densification stages from firn to ice (modified after Blunier and Schwander, 2000)

Finally the maximum density of pure ice at a temperature of 0° C and low pressures is $\rho = 917$ kg/m³. For massive polar ice sheets with lower temperatures and higher pressures because of

their immense size, the maximum density can vary up to 922 kg/m^3 (Cuffey and Paterson, 2010).

1.3. Seismics in glaciology – state of the art

Several studies with seismic campaigns were carried out in different regions and glaciers during the last decades. Explosive shots within a borehole were always common. In addition a vibration system (Vibroseis) was used for the first time by the *Alfred-Wegener-Institut für Polar- und Meeresforschung* (AWI) in 2010, also a detonation cord became more feasible later (Hofstede et al., 2013). The first applications at the beginning of the 21st century prove that a vibrator as a seismic sources works on ice in the Antarctic (e.g. Eisen et al., 2010a (unpublished report); Kristoffersen et al., 2010; Hofstede et al., 2013; Eisen et al., 2015). In comparison to explosive shots, a vibration system has some benefits. While for detonation charges holes with a depth of 2-5m have to be drilled (Hofstede et al., 2013), that is time consuming, a vibration system is a fast repeatable method for seismic profiling. It is also non-pollutive and decreases risks and transport effort (Hofstede et al., 2013). Furthermore explosive shots create a noisy signal called “ghost” that describes a wave moving up to the ice surface and then downwards creating holes in the frequency spectrum (Eisen et al., 2010a) that does not occur with sources triggering shots at the surface like Vibroseis. On the other hand in comparison to explosive shots, the frequency bandwidth of a vibrator is limited for higher frequencies so the resolution of explosives is superior that makes englacial reflections more clearly visible (Hofstede et al., 2013). Over a long time period of studying the technique of seismic campaigns is being proved for its meaningful and accurate predictions about spatial conditions in glaciology. Several studies during the last decades depict the importance about uncertainties regarding to different physical parameters that will be explicated below.

Subglacial reflection coefficient

Seismic waves triggered at the surface propagate through the ice column and reflect or refract at an interface. The reflection coefficient gives the relative amplitudes (so the ratio) of the incident and reflected waves (Dobrin and Savit, 1988). A lack of knowledge of the absolute source amplitude and the attenuation of the waves causes uncertainties in calculating the reflection coefficient that further makes it impossible to absolutely identify a subglacial material (Holland and Anandakrishnan, 2009).

The angle dependent reflection coefficient can be calculated with the receiver amplitude, the source amplitude, the ray path and the attenuation. Holland and Anandakrishnan (2009)

described new methods to calculate englacial reflection coefficients without a prior knowledge of the source amplitude or the englacial attenuation. A number of previous studies like Smith (1997; 2007) and others used calculations based on dependences between attenuation and energy. One method is to quantify the changes in energies between multiple bed reflections based on the assumption that the attenuation does not change within normal incident angles (Smith, 1997). Holland and Anandakrishnan (2009) illustrated the important difference between linking the attenuation to the amplitude instead of the energy. The attenuation is defined relative to the amplitude (Sheriff and Geldart, 1995). Because the amplitude ratio is the square root of the energy ratio (Dobrin and Savit, 1988), this causes wrong estimations about the reflection coefficient at the interface of ice the subglacial material. The second approach is the direct path method where the offset-dependent decrease of the amplitude of the arriving direct wave along the surface is observed. With respect to the spherical divergence the ratio of the amplitudes of different distant receivers can be extrapolated and give information about the source amplitude.

Temperature dependence of attenuation

Holland and Anandakrishnan (2009) mentioned the need to know the seismic attenuation α of seismic waves. Without a prior knowledge about the attenuation it is not possible to distinguish between a crystalline rock and unconsolidated sediments as a subglacial material (Holland and Anandakrishnan, 2009). Peters et al. (2012) further showed the sensitivity of the attenuation or internal friction to the temperature regime within the ice column and the ice crystal orientation. Using a spectral ratio method they calculated the seismic quality factor Q and generated a temperature profile with depth. They show results with a good agreement between their calculated temperature profiles dependent on the quality factor and given temperature profiles of boreholes. Peters et al. (2012) showed that their method can be used to determine the thermal regime within an ice sheet that further enables the evaluation of the attenuation. Because they link their results to existing borehole data, it is difficult to make general estimations as boreholes are cost intensive and only give point measurements. Furthermore Peters et al. (2012) disregarded uncertainties by the undefined absolute coupling to the ground as described by Holland and Anandakrishnan (2009). The unique location of the PALAOA Observatory gives the motivation of the thesis.

PALAOA Observatory

The Ekström Ice shelf (EIS) is well studied because of the German scientific station *Neumayer III* and the previous *Neumayer II* station. Several seismic surveys on the EIS were executed (e.g.

Eisen et al., 2010a; Hofstede et al., 2013; Kristoffersen et al., 2014). In 2005 four hydrophones were set up beneath the ice shelf to study the underwater soundscape (Kindermann et al., 2008). First impressions show that the hydrophone is able to record seismic shots and finally becomes the fundamental idea of this thesis. As it is different to other seismic campaigns, the coupling of the hydrophone to the surrounding water is very good. The reflection coefficient that is exceedingly important for seismic analysis in this study is well known.

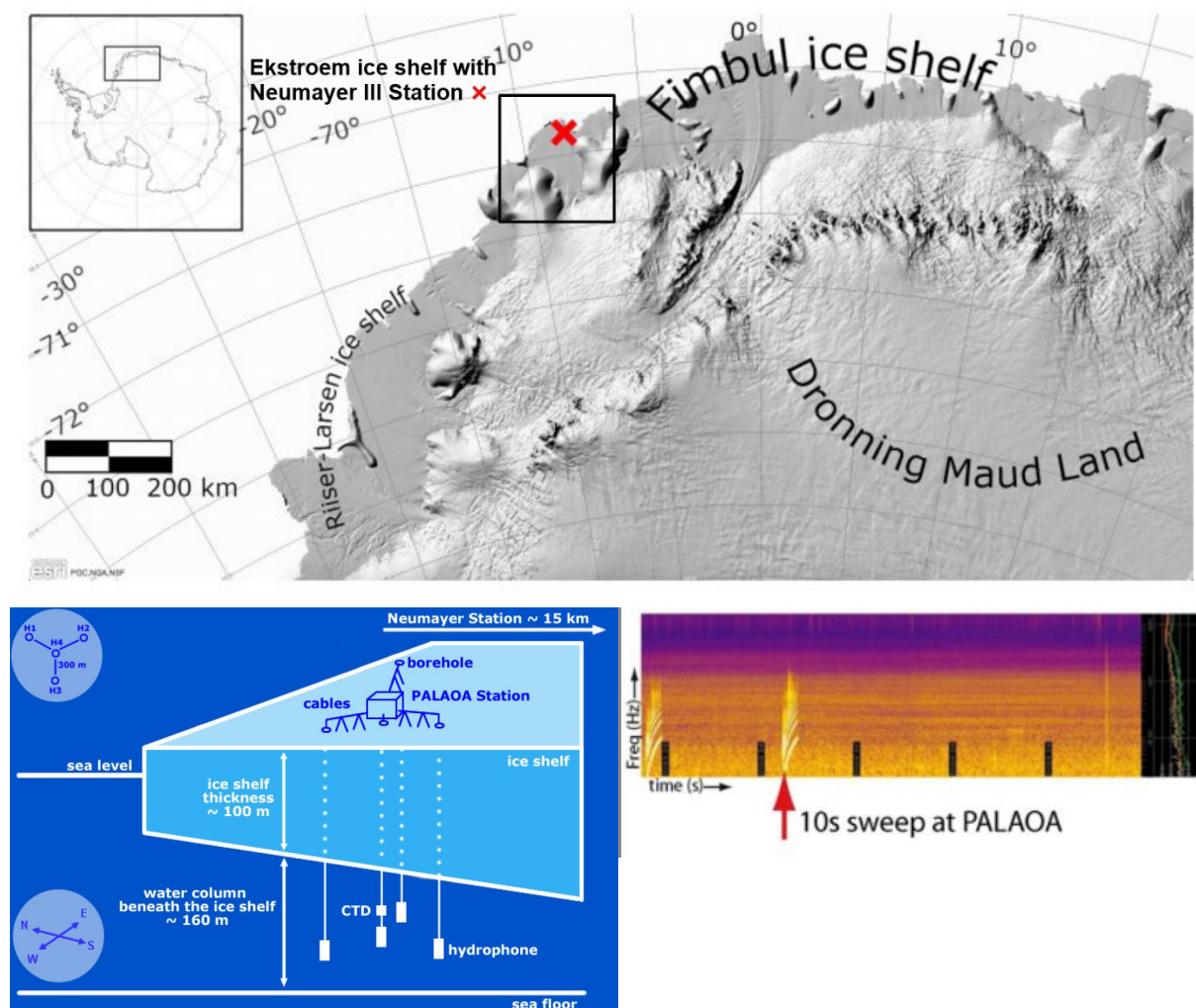


Figure 5 (upper): The map shows the survey area located on the Ekström Ice Shelf in Dronning Maud Land in the Antarctic. The red cross marks the location of the Neumayer III Station (modified after Jacobs et al., 2019). Lower, left: Configuration of PALAOA (Kindermann et al., 2008). Lower, right: Vibroseis sweep recorded with the PALAOA hydrophone on 4th February 2010 (Eisen et al., 2010a).

1.4. Motivation and structure of the thesis

Because of the location and configuration of the PALAOA hydrophone this thesis presents a new way of analysing glaciological seismic data on ice. Several uncertainties are common in glaciological seismic surveys on ice like the source energy that penetrates into the ice and the amount of seismic attenuation.

The primary aim of the thesis is to interpret the seismograms recorded by one PALAOA hydrophone (Figure 5) and calculate amplitudes of different event arrivals, e.g. the direct wave or seafloor reflection. For this, the ray paths and travel times of different events will be calculated before. During the survey in 2009/10 also a surface geophone streamer was used. The approach of the streamer data is to get an overview about the ice thickness along the shot points and ice shelf and further the seismic velocity in the ice shelf. Details about the source, geophone streamer and hydrophone configuration are mentioned in chapter 3. This is important to get the basics of the geometry of the ray paths and the velocity of the seismic waves. Before calculating travel times, the spatial conditions have to be reviewed.

Given that the hydrophone is placed in the water column, the seismic waves follow a ray path that enables a new way of observing and analysing their physical properties. With well-known values of ice and water density and velocity and *Snell's Law* (1621), the travel times of different events can be calculated. Three different amplitudes will be calculated: (1) Maximum Amplitude (Max), (2) Root-Mean-Square Amplitude (RMS) and (3) Average Amplitude (Avg.) within different time gates at the time of arrival of the different events. In combination with the shot geometry with increasing offsets (= distance between source and receiver / hydrophone) to the fixed PALAOA hydrophone the changes of amplitudes are analysed to give an outlook about the impact of the attenuation of the seismic waves through the ice column and the representation of the results as an alternative way to advance seismic on ice shelves.

2. Theoretical background

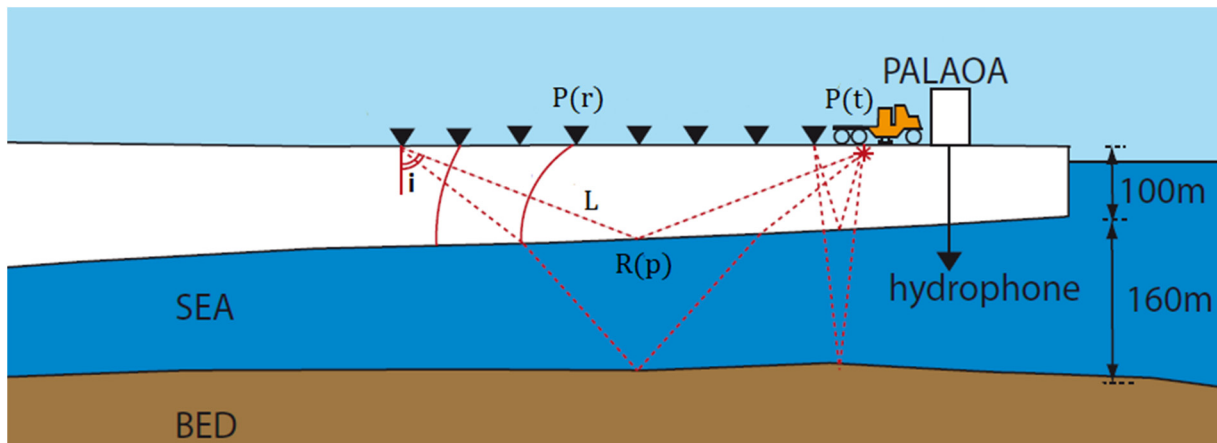


Figure 6: General remarks of seismic campaigns on ice shelves (white) floating on sea water (blue) with thicknesses matching the spatial conditions on Ekström Ice Shelf. The source $P(t)$ transmits seismic waves with a wavefront (red lines) and the travel path L (red dashed lines) that propagate through the media in the ground where they reflect based on the reflection coefficient ($R(p)$) at the ice-water interface and move back towards the receivers $P(r)$ (modified after Eisen et al., 2010a). The incident angle i depends on the position of the source and the particular receiver.

The main purpose of seismic observations is the determination of different lithology's and their thicknesses and physical properties. The setup of the surveys consists of a source and receivers. Sources can vary in type of signal triggering but all function aiming an identical purpose. Receivers are generally geophones or hydrophones (in marine seismics) placed as a group within a streamer so a single shot is measured by a plurality of receivers. With an assumed velocity and the downward – upward travel time, the two-way traveltime (TWT), of the reflected waves the proper subsurface structure can be constructed.

The seismic wave field consists of two different types of waves (body waves and surface waves), each separated into two subclasses (body waves = compressional and shear waves; surface waves = *Rayleigh*- and *Love*-waves). Body waves propagate through a medium away from the surface and surface waves arise at an interface of two media like the earth's surface and move along them. In all cases the propagation takes place by an elastic displacement of particles but in a different direction of motion of the particles with respect to the direction of wave propagation. Each of the four types of seismic waves follows *Huygen's Principle* (1678) of wave propagation. The principle indicates that in a single medium every point of a wavefront can be regarded as a new spherically spreading wave front (Dobrin and Savit, 1988; Lowrie, 2007). In a homogenous, isotropic medium, the wavefront spreads spherically with a constant curvature at the same time and distance to the source where all particles vibrate in the same phase. As the energy from a point source spreads spherically with increasing distance r , the energy decays with a factor $1/r^2$ and the amplitude, being proportional to the root of the energy, decays with a factor $1/r$. The

loss in energy and amplitude caused by the spreading of the wavefront is called *spherical divergence* and its correction is a basic part in seismic data processing (Yilmaz, 1987) (in Figure 6 is $r = L$). The direction perpendicular to the wavefront is the *raypath* and a central part of observation and analysis in this work. The physical properties of the different waves will be explained in the following.

2.1. Seismic waves

2.1.1. Body waves

Body waves can be classified into compressional and shear waves. Compressional or longitudinal waves have the highest velocity of all wave types within the same medium and are the first or primary (P-waves) waves arriving in seismometers or geophones (Haldar, 2013). The direction of the particle motion is the same as the direction of propagation of the wavefront (longitudinal) so they are one-dimensional waves (Figure 7). Let the moving direction F_x of the wavefront A_x be the x-axis (Figure 7), the medium experiences a stretching and compressing parallel to the x-axis. The distance between the particles in x-direction changes. P-waves appear in all three phase states of a medium (solid, fluid, gas). The velocity of compressional waves depends on the elastic moduli and can be expressed after Lowrie (2007) as:

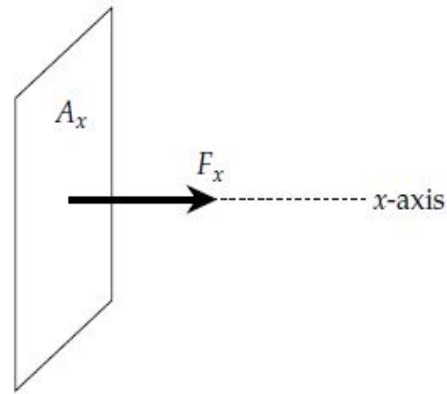
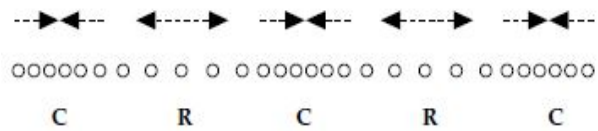


Figure 7: The propagation of compressional (P-waves) occurs in a stretching and compressing of the medium (upper part) parallel to the moving wavefront direction (x-axis in the lower part) (Lowrie, 2007).

$$v_p = \sqrt{\frac{k + \frac{4}{3}\mu}{\rho}}, \quad (2.1.1)$$

with the bulk modulus k , the shear modulus μ and the density ρ .

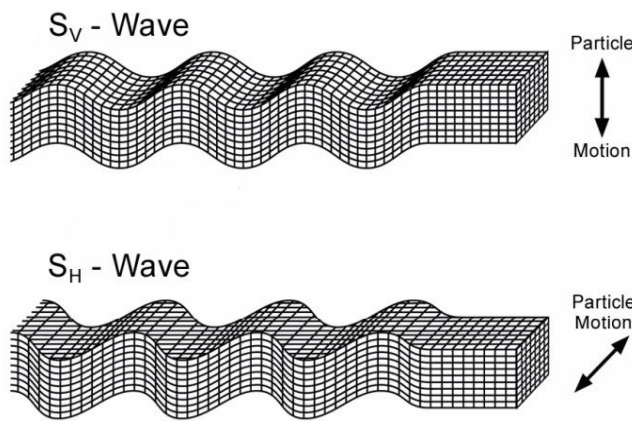


Figure 8: Shear or transversal waves (S-waves) occur with a horizontal or vertical movement of the particles perpendicular to the propagation direction through a solid medium (modified after Steeples, 2005)

Shear or transversal (S-waves) waves are the second type of body waves but differ in their properties to compressional waves. The particle motion does not occur in a stretching and compressing parallel to the direction of propagation but perpendicular to it in y- or z-direction (Lowrie, 2007). There are two types of shear waves. S_V waves describe shear waves with particles moving in a vertical direction, whereas S_H waves indicate a horizontal particle motion (Figure 8). The velocity of shear waves can be expressed as:

$$v_s = \sqrt{\frac{\mu}{\rho}} \quad (2.2.2)$$

The parameters are explained in equation 2.2.1 above. Because the shear modulus becomes zero in liquids and gases, S-waves only occur in rigid bodies (Lowrie, 2007). The bulk modulus stays always positive so the velocity of shear waves is lower than for P-waves ($v_p > v_s$) so they occur later in seismograms or at geophones but with higher energies.

2.1.2. Surface waves

There are two types of surface waves named *Rayleigh-* and *Love* waves that differ in their particle motion (Figure 9). Whereas P-waves swing one-dimensionally in propagation direction and S-waves two-dimensionally in the propagation direction and vertically (S_V) or horizontally (S_H) perpendicular to it, the surface waves can be regarded as a combination of both (Lowrie, 2007). The particles within a Rayleigh-wave experience a combination of a P-wave and a S_V -wave and move in a retrograde ellipse perpendicular to the surface. Love-waves propagate parallel to the free surface and perpendicular

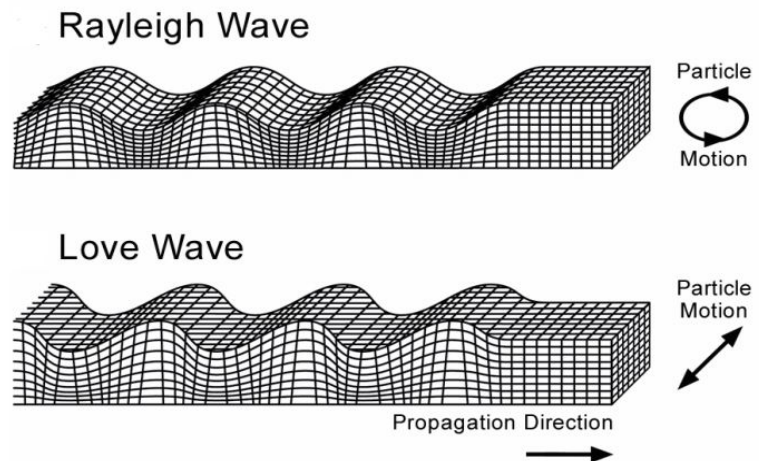


Figure 9: Particle motion of Love- and Rayleigh waves (surface waves) in dependence of the propagation direction (modified after Steeples, 2005).

to the propagation direction as a combination of a P-wave and S_H -wave. Surface waves occur at surfaces and interfaces and move with lower velocities along it. They are frequency dependent and have the highest amplitudes and energies and are visible in seismograms showing up as large and responsible for damages.

2.2. Wave propagation characteristics

Acoustic Impedance

As mentioned before propagating seismic waves follow *Huygen's Principle* (1678). This implies that each ray has a unique travel path and is calculated by the medium velocity and the time after the shot was fired. Figure 10 shows a spherically spreading wavefront propagating in a medium. A basic assumption for simplified ray paths is that the medium is homogeneous and isotropic so its density and the acoustic velocity or the orientation of the particles does not change within the medium. As the wavefront propagates spherically the rays move in every direction of all three dimensions with the travel path r (Telford et al., 1991; Lowrie, 2007). The energy and amplitude of the waves depends on the travel path r . When a seismic shot was fired at the surface of a solid medium (e.g. on an ice shelf) the P- and S-waves propagate into the ground through different media with changing physical properties. The acoustic impedance Z of a medium is given by its density ρ and velocity v and defined as:

$$Z = \rho * v. \quad (2.2.3)$$

At an interface of two media with an abrupt change in their acoustic impedance reflection and transmission takes place (Figure 11).

Snell's Law

An incident P- or S-wave reflects at a media interface and travels back to the upper surface. The angle of incidence θ_1 (in Figure 11 it is i_p) is equal to the angle of reflection. The amplitude decreases depending on the acoustic attenuation and travel path and furthermore the reflection coefficient that is also depending on the angle of incidence. A refracted wave propagates into the lower medium at a media interface and changes its angle of travel path according on *Snell's law*:

$$\frac{\sin\theta_1}{v_1} = \frac{\sin\theta_2}{v_2}. \quad (2.2.4)$$

Snell's Law depends on the sine of the incident angle θ_1 and the velocity v_1 of the upper medium and the refracted angle θ_2 and velocity v_2 in the lower medium (Dobrin and Savit, 1988; Lowrie,

2007). The angles θ_1 and θ_2 are directed to the lot perpendicular to the layer boundary (in Figure 11 it is $i_{p,s}$ and $r_{p,s}$). An incident P-wave can also be converted into a refracted S-wave at the layer interface (P-S-Conversion) and inverse (S-P-Conversion).

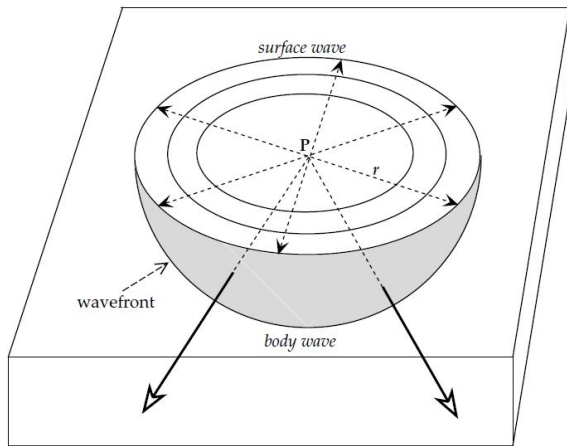


Figure 10: When a seismic shot is triggered with a source at the point P the waves propagate on a sphere in every dimension with the distance r to the source. The spherical wavefront is built by body and surface waves (Lowrie, 2007).

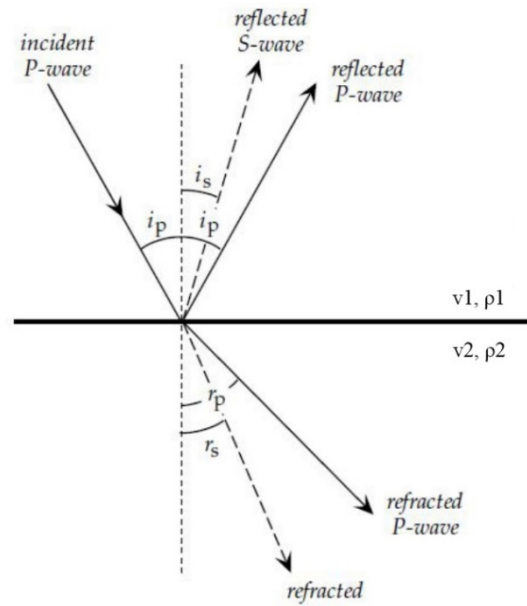


Figure 11: An incident P-wave creates different kinds of refracted and reflected waves at a layer interface where physical properties (density and / or velocity) change (modified after Lowrie, 2007).

Diving waves

Diving waves occur in regions where the density is constantly increasing within a single medium like firm. A diving wave is a constantly refracted wave, as *Snell's law* predicts. This makes the waves propagate in a different ray (Figure 12). Diving waves occur in seismic data in the upper part so they can overlay and disturb important signals like direct waves or reflections. For sweeping signals of a Vibroseis this can be decreased as the energy is propagated directional downwards.

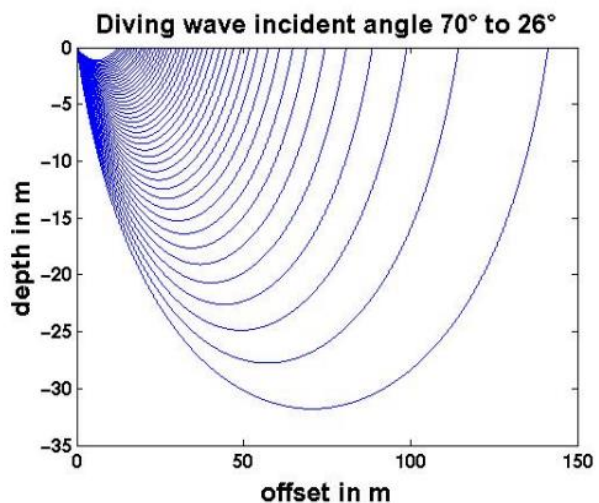


Figure 12: Travel path of diving waves within a single medium caused by constant changing density and / or velocity (e.g. on an ice shelf) (Diez, 2013).

Travel time curves

Different types of waves have different characteristics. The direct wave propagates directly from the source to receiver. Direct waves are the first signals in receivers and useful for calculating seismic velocities of the medium. With lower offset and thus shorter travel paths of the seismic waves the first arriving signal at the receiver is the direct wave. With increasing offsets at a critical point the critically refracted wave overtakes the direct one because of its higher velocity in the lower medium (in two layered media conditions with $v_1 < v_2$ (also Figure 13)). The reflected waves are the last signals and not arriving in a linear delay with respect to the offset but as a hyperbole caused by the *normal move out* (NMO) that will be explained later (Figure 13).

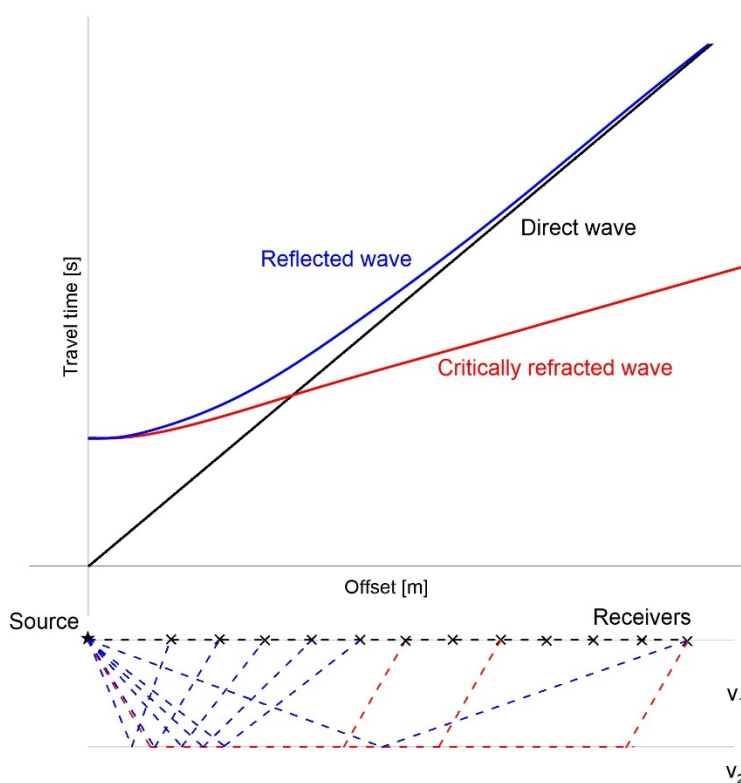


Figure 13: Travel time curves of direct, reflected and refracted P-waves (upper part) and their travel paths within a homogenous and isotropic medium (2 layers) and $v_1 < v_2$ (lower part).

Reflection (RC) and transmission (TC) coefficient at normal incidence

As similar to reflected waves, the amplitude of refracted waves changes depending on the physical properties. Because in this study the hydrophone stays in the lower medium, the transmission coefficient is important. The reflection and transmission coefficients depend on the acoustic impedance Z . Near normal incidence angles up to about 15° do not make significant changes in the amplitude (Lowrie, 2007), but with increasing angles (larger offsets, so larger distances between the source and receiver), the reflection coefficient changes. Then,

the partitioning of energies at a media interface follows the *Zoeppritz*-Equations, a set of complex equations (Aki and Richards, 2002; Dobrin and Savit, 1988). The reflection angle is always equal to the incident angle because the medium velocity is the same (Dobrin and Savit, 1988). In case of normal incidence the ratio of reflected energy E_r and incident energy E_i of two media is given by the impedances (equation 2.2.3) according to:

$$\frac{E_r}{E_i} = \frac{(\rho_2 v_2 - \rho_1 v_1)^2}{(\rho_2 v_2 + \rho_1 v_1)^2} \quad (2.2.5)$$

The square root of equation 2.2.5 depicts the amplitude ratio of the incident and reflected waves and thus the reflection coefficient R of incident waves at an interface of two media. The reflection coefficient can be positive or negative due to the velocity or density of the lower medium. If the velocity is lower than in the upper medium the reflection coefficient contains a 180° shift phase and becomes negative (Dobrin and Savit, 1988). It can be recognized by the following equation:

$$R = \frac{\rho_2 v_2 - \rho_1 v_1}{\rho_2 v_2 + \rho_1 v_1} = \frac{Z_2 - Z_1}{Z_2 + Z_1} \quad (2.2.6)$$

The reflection coefficient is given by the impedance Z_1 , velocity v_1 and density ρ_1 of the upper medium and the impedance Z_2 , velocity v_2 and density ρ_2 of the lower medium.

After Holland and Anandakrishnan (2009) the reflection coefficient especially for seismics in glaciology should be calculated in an alternative way with the following equation:

$$R(\phi) = \frac{A_1(\phi)}{A_0} r(\phi) e^{\alpha r(\phi)} \quad (2.2.7)$$

Here the angle dependent reflection coefficient $R(\phi)$ depends on the source amplitude A_0 , the receiver amplitude A_1 , the ray path r and the temperature dependent wave attenuation α . The equation is more specific as the very dominant and important attenuation α is taken into account.

The transmission coefficient T gives the amplitude change of traveling waves caused by different velocities of two media. The transmission coefficient stays always positive and can be calculated with equation 2.2.8. The sum of R and T at an interface is always 1. Variables match that ones in equation 2.2.6.

$$TC = \frac{2Z_1}{Z_2 + Z_1} = \frac{2\rho_1 v_1}{\rho_2 v_2 + \rho_1 v_1} \quad (2.2.8)$$

2.3. Seismic source

2.3.1. Vibroseis signal

Vibrator seismic (Vibroseis) is commonly used on land, as it is non-destructive, non-pollutive and a fast reducible method. The *AWI* in Bremerhaven was the first and the only institute using vibration systems in glaciology (Kristoffersen et al., 2014; Polom et al., 2014). There are some difference between other conventional methods. First is the duration of a Vibroseis signal known as a *sweep* with a time duration T of several seconds. Thus the analysis and interpretation of the data is different to other methods as the generated sweep has to be cross-correlated with the source sweep to make amplitude peaks in time or frequency domain visible (chapter 2.3.2). There is a better source control using a baseplate in comparison to explosive charges. Further the motion of the plate is purely vertical so the signal penetrates efficiently downwards. Because the source is at the surface, there is no ghost as mentioned before that disturbs the signal. In most cases a Vibroseis truck on ice by the *AWI* is used with a geophone streamer behind it. Preparation and signal triggering just takes several minutes as soon as the shot point (SP) is reached (Eisen et al., 2010a). The driving force is generated by an electrodynamic, hydraulic or magnetic system applied to the baseplate that is connected with a top plate and a reaction mass (Figure 14) (Baeten, 1989). The connection of the baseplate to the ground depends on the ground conditions like roughness and porosity.

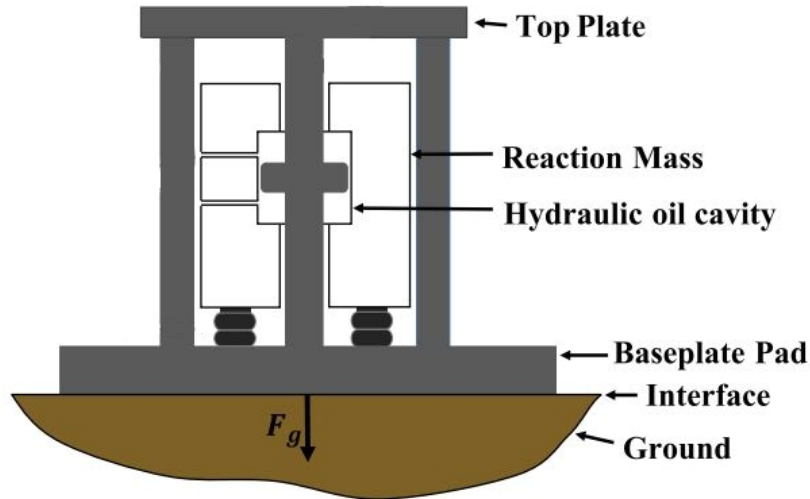


Figure 14: Sketch of the operating method of a seismic vibrator system (Modified after Huang et al., 2018).

A sweep consists of a sine wave with a linearly increasing frequency (Figure 15). An increasing frequency leads to a decrease in the wavelength, the mathematical form of a sweep can be expressed [After Baeten (1989)] as:

$$s(t) = a(t) \sin [2\pi\theta(t)], \quad (2.3.1)$$

with the sweep signal $s(t)$, a taper function $a(t)$ and the time dependent frequency function $\theta(t)$. The amplitude stays at the same value during the sweep generation. The taper function reduces mathematical errors at the edge of filtering known as the *Gibbs'* phenomenon that describes a ringing caused by the Fourier transformation.

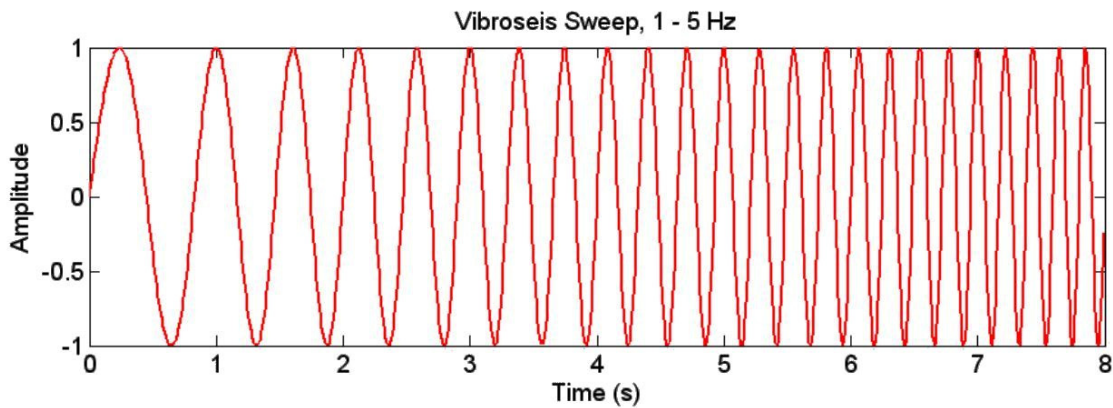


Figure 15: Example of a sweep triggered by a Vibroseis with a linearly increasing frequency range from 1 to 5 Hz over a time gate of 8 seconds (modified after Braile, 2016).

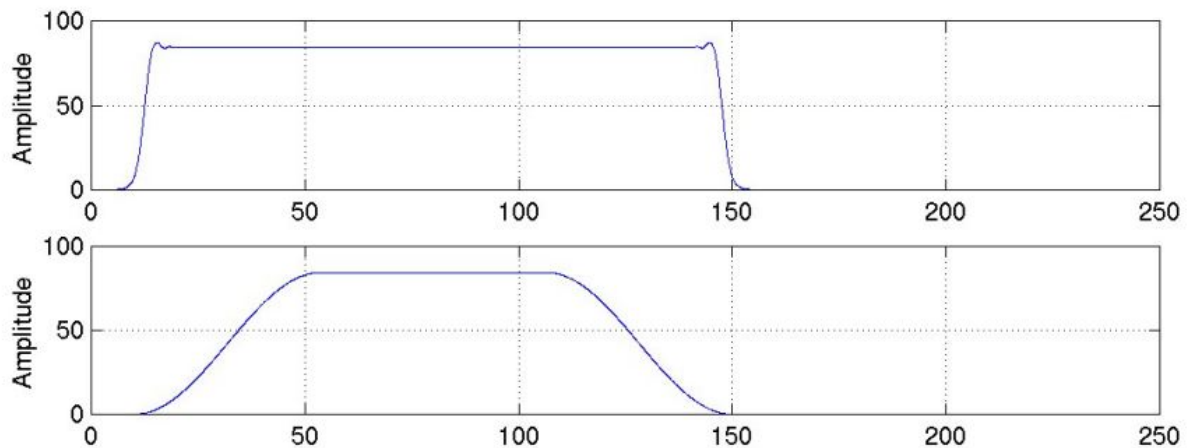


Figure 16: Synthetic linear sweeps with a taper function of 0.5 seconds (upper) and 5 seconds (lower) (Brittle et al., 2001).

2.3.2 Cross-correlation

To make the source signal of Vibroseis shots visible, a cross-correlation has to be applied. It is a standard method to filter the original signal out of the seismogram. The source sweep signal $s(t)$ with the time duration T penetrates with a linearly increasing frequency into the ground. Different layers with abrupt changing impedances reflect the source signal to the receiver that sums all incoming reflected signals at different interfaces within a timespan (Figure 17 “recorded seismogram”). A cross-correlation of two identical sweeps is an auto-correlation. Using the cross-correlation, a synthetic signal with the same fundamentals of the source sweep ($T = 10$ s, frequency range: 10 – 100 Hz were used during the data acquisition this thesis deals with) superimposes the recorded seismogram over time. If the synthetic sweep completely matches the recorded signal, the cross-correlation sums the multiplication of both signals. This creates a time dependent signal with peaks that represent the summed amplitude of different reflection events. A large positive peak represents a nearly complete match of the earth responded source sweep and the synthetic one. Because the whole sweeps are multiplied and summed, the resulting amplitudes become very large on the orders of 10^6 and higher (e.g. amplitudes of explosive charges are in orders of 1-10).

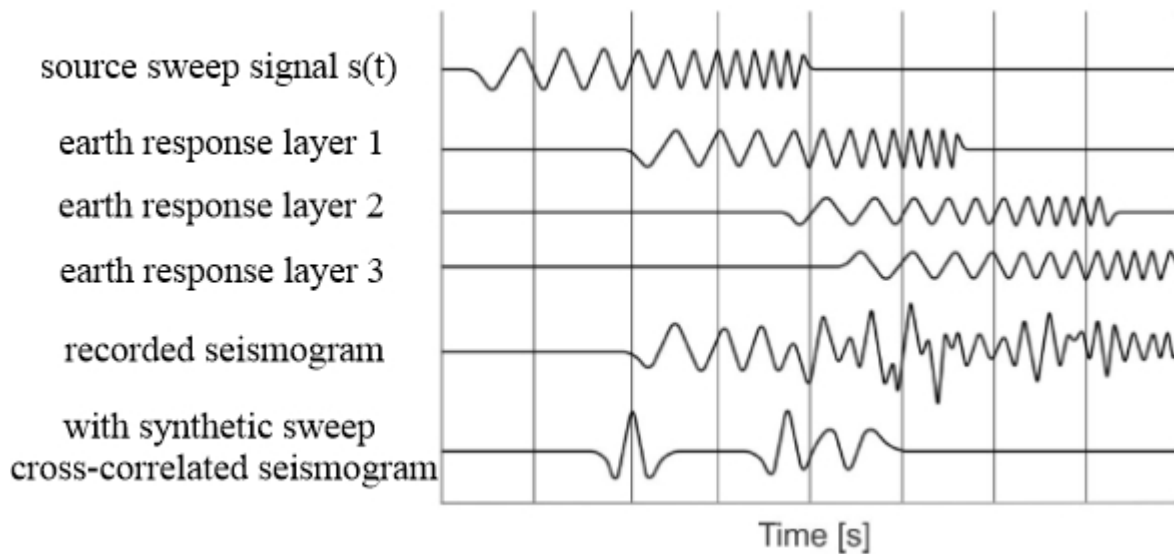


Figure 17: Sketch of the principle of a cross-correlation. A source sweep (pilot sweep) with a linearly increasing frequency reflects at exemplary different layers as earth response. The lowest graph shows the seismogram of the input trace cross-correlated with a synthetic sweep (modified after Lindseth, 1968).

2.4 Receivers

2.4.1 Surface geophones

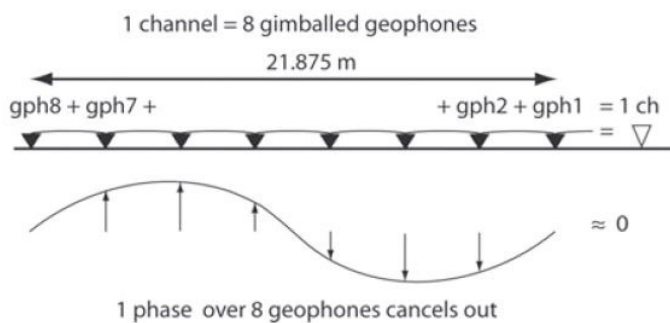


Figure 18: Ground roll suppression by eight geophones grouped in a channel (Hofstede et al., 2013).

In general seismic waves are recorded by geophones on land and by hydrophones in marine observations. Geophones detect arriving energy in form of ground motion transformed into an electrical impulse (Onajite, 2013). The geophone contains a magnet within a coil creating a permanent magnet field. Arriving seismic waves accelerate the magnet relatively to the coil caused by ground

motion. This induces a voltage proportional to the particle motion in the ground (Onajite, 2013). Because the measured energy of a single geophone is very small, several geophones are grouped together in a *channel*. Furthermore ground roll of surface waves that disturb the results can be decreased. Thus, the sum of amplitudes within one phase that matches the length of the geophone chain becomes zero (Figure 18). On the other hand this configuration has a disadvantage: With large offsets the wavefronts arrive in low angles at the geophones that induces spatial aliasing. To avoid this, the streamer configuration was changed (explained in chapter 3). A number of channels with a given distance to each other are grouped together in a *streamer*. This allows the record of a single shot with several geophones along a distance at the

surface. The electric signals are transferred to the data acquisition, including analogue to digital conversion.

2.4.2 PALAOA hydrophone

In contrast to the grouped channels of geophones in a streamer the PALAOA station has a different setup. PALAOA contains actually two active hydrophones of which one is used for this work. The exact location is shown in chapter 3 (Figure 20, 21, 24). The hydrophone is a *Teledyne Reson TC4033 Spherical Reference Hydrophone* (Eisen et al., 2010b, unpublished report). It measures the acoustic waves triggered by the seismic source using a piezoelectric sensor element. The piezo effect describes an electric signal generated by the movement of electric charges. Basically there are two regions in the element: one partially positive loaded and one partially negative loaded. Without any impacts the loads are balanced so there is no electricity. If a seismic or acoustic wave arrives at the enclosing membrane the piezo element gets compressed and the two partially loaded regions are moved with respect to each other. Thus, on both sides an excess of electrical load arises and triggers an electrical signal. The acquired signal is calibrated and thus directly proportional to the sound pressure level in the water. The hydrophone has a frequency range from 1 Hz – 140 kHz with a sensitivity of -203 dB re 1 μ Pa/V.

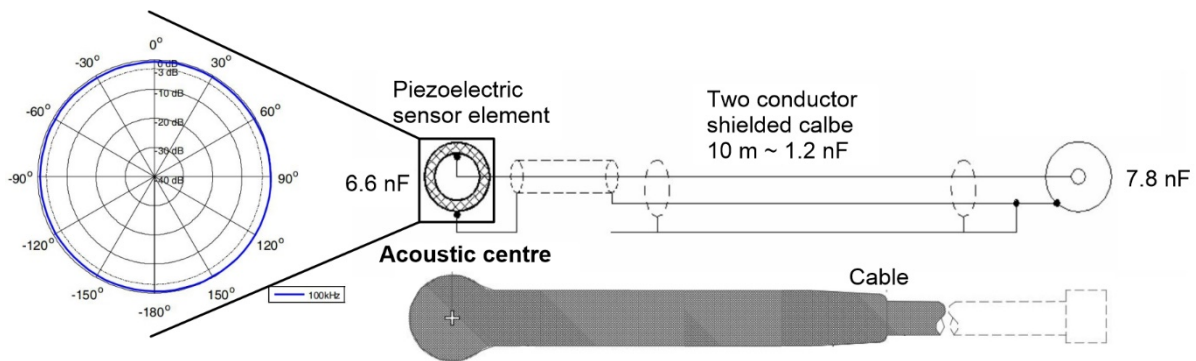


Figure 19: Schematics of Teledyne Reson TC4033 Spherical Reference Hydrophone. It consists of a piezoelectric sensor element that builds the acoustic centre. It is coupled to a cable that is connected with digital systems at the ice surface (modified; from: <http://www.teledynemarine.com/reson-tc-4033>; last call: 21.04.2020)

3. Database and Methodology

3.1 Field site

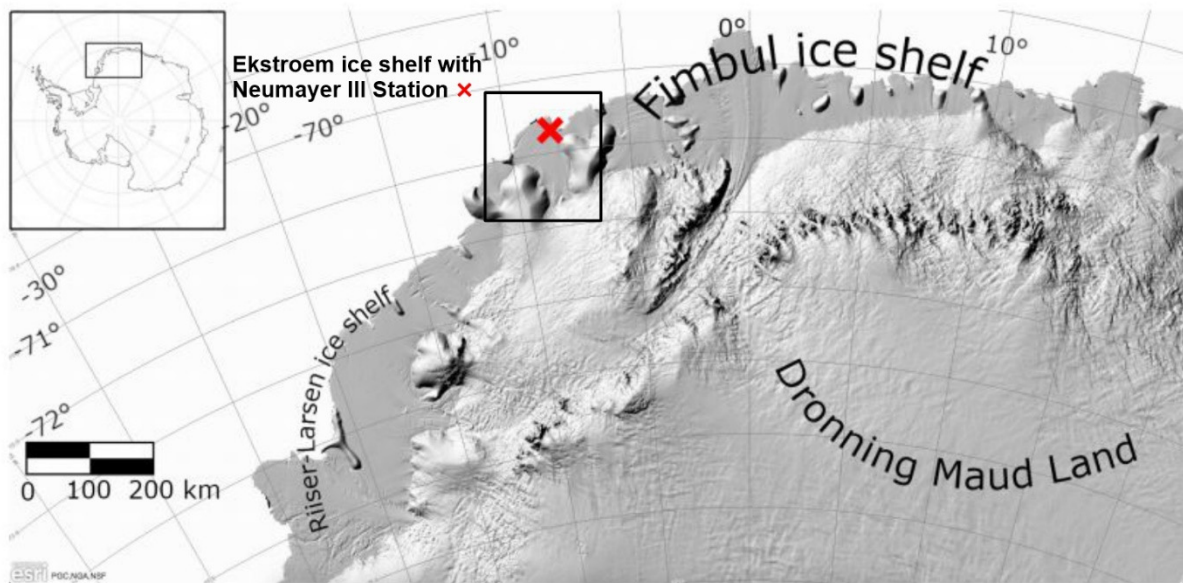


Figure 20: The map shows the survey area located on the Ekström Ice Shelf in Dronning Maud Land in Antarctica. The red cross marks the location of the Neumayer III Station (modified after Jacobs et al., 2019).

The data was acquired during the *LIMPICS* (Linking micro-physical Properties to macro features in ice sheets with geophysical Techniques) ANT 2009/10 campaign that was focussed on a Vibroseis survey on the Ekström Ice Shelf (EIS) and a seismic survey with explosive charges in combination with low-frequency radar Halfvarryggen ice dome (HID) (*LIMPICS*). The Ekström Ice Shelf is located in the East Antarctic at the north-western Dronning Maud Land (DML) (Figure 20) and thus part of the Antarctic coastal zone. With a size of about 6800 km² the Ekström Ice Shelf measures about 60 km in east-west direction and 120 km from north to the south so it is a comparatively small ice shelf (Neckel et al., 2012). The shelf reaches into the Atlantic Section of the southern ocean. Several studies estimates an average ice thickness of about 100 m at the edge of the shelf increasing to almost 1000 m towards the inland ice sheet. The underlying water column exhibits thicknesses of about 160 m at the area of interest

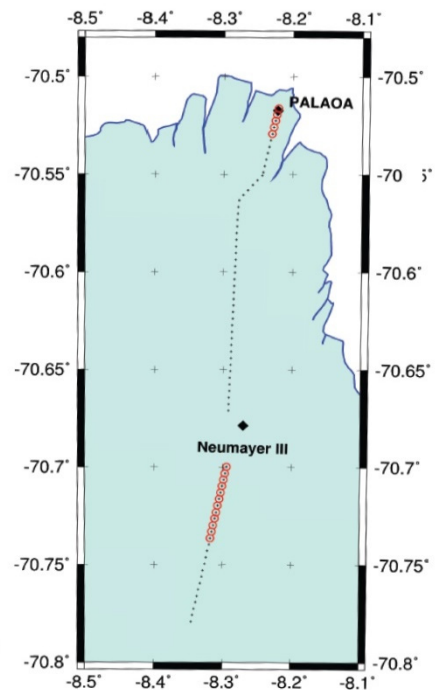


Figure 21: Location of seismic shots during *LIMPICS* ANT 2009/10 campaign between the PALAOA hydrophone and Neumayer III Station. Red circles mark explosive shots, black dots show Vibroseis shots (Eisen et al., 2010a).

(Sandhager and Blindow, 2000; Kindermann et al., 2008; Eisen et al., 2010a; Smith et al., 2020). On the EIS different surveys were operated. At PALAOA two surveys from the 4th to the 6th of February 2010 with different streamer configurations were operated. One of them was operated in the south of *Neumayer III Station* (STR) between the 29th of January and the 2nd of February but not recorded with PALAOA. The data used for this work was acquired between the PALAOA hydrophone at the northern edge of the shelf and the Neumayer III Station that is positioned 15 km to the south (Figure 21) named as the *PALAOA Traverse* (PTR). The exact locations of the shots are shown in Table 2.

3.2 Data acquisition and measurement setup

The seismic shots were acquired with the Failing 1100 Vibrator Vibroseis truck of the University of Bergen with a full weight of 16 tons (Eisen et al., 2010a). The data were recorded with a 60 channel streamer. Eight 14 Hz geophones (gimballed SM4 geophones) build one channel. The use of a streamer is very important for amplitude studies and the information about the ice and water velocity and thickness. The shot information is listed in Table 1.

The streamer was placed behind the truck with a distance (=offset) of 44 m between the first geophone and the source. The streamer has had a full length of 1500 m including 60 channels with a spacing of 25 m. Because the upper 500 m was the zone of interest, the streamer was towed in a loop so reflections in deeper regions will not arrive the geophones. It was also applied to minimize the channel spacing and thus spatial aliasing. This creates an effective streamer length of 750 m with a channel spacing of 12.5 m. Therefore, channel 30 has had the largest offset to the source while channel 60 was the closest one (see Figure 23). Two sweeps were triggered at every shot point (SP). After two shots the truck moved by 6.25 m (as half the distance of two channels) while the streamer stayed at the same position and another two shots were triggered. This simulated a 120 channel streamer with a spacing of 6.25 m and 4 shots per SP. The distance between groups of four shots was 375 m.

Altogether 98 shot points with each two sweeps were triggered in this streamer configuration. The source generated a sweep with a 10 second duration and a frequency range of 10 to 100 Hz and a sample rate of 1 ms. Data were recorded with the surface geophones with a length of 12 seconds.

The first shot was located 130 m in the North of PALAOA and the survey direction was to the southern in direction of the Neumayer III station (see Figure 24). The PALAOA data on the other side was not coupled to the source so the data for the work are audio files converted into segy-data by Dr. Veit Helm (AWI) with a record length of 20 seconds and a different sample rate of 0.5 ms that include the shot signal (Figure 22).

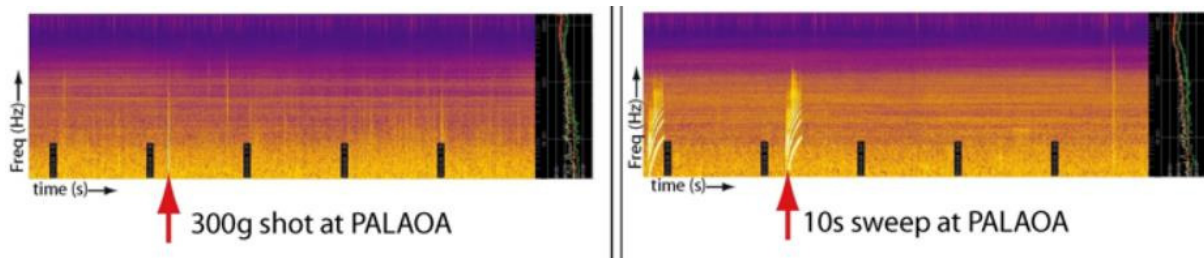


Figure 22: One explosive shot (left) and Vibroseis sweep (right) recorded with PALAOA at the 4th February 2010 (Eisen et al., 2010a)

The streamer configuration is illustrated in the following.

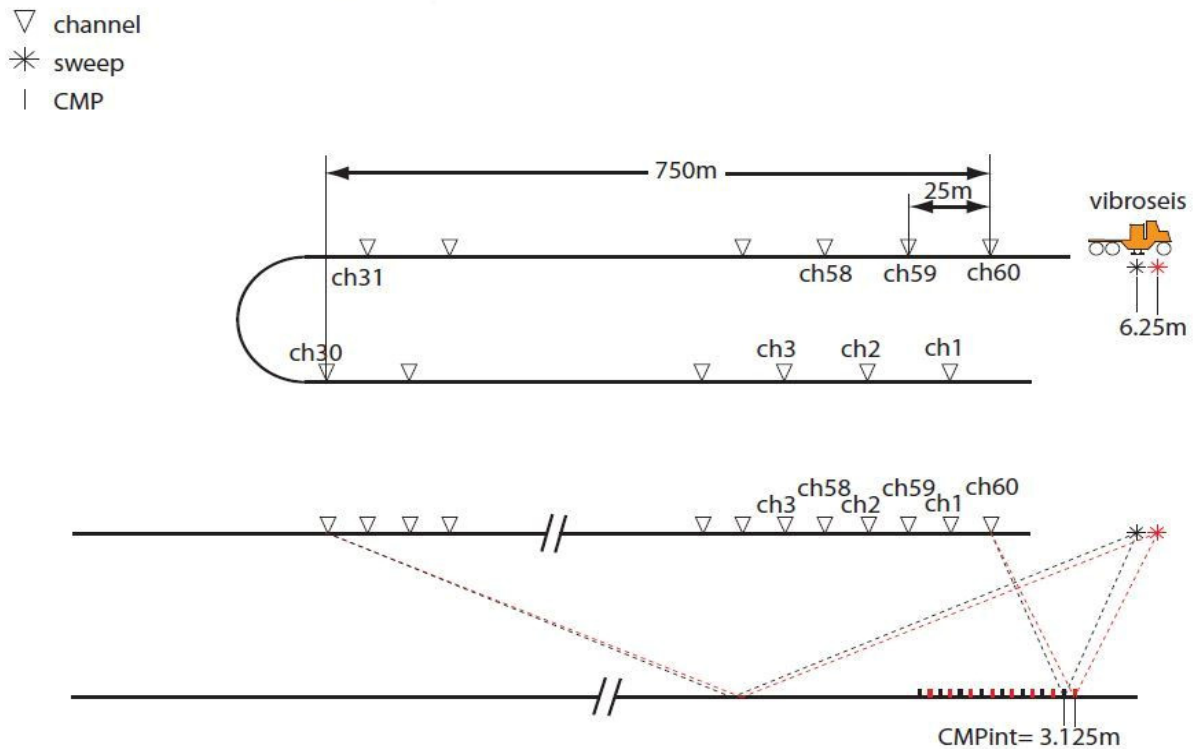


Figure 23: Streamer configuration during the PALAOA Traverse data acquisition (modified after Hofstede et al., 2013)

Table 1: Source and receiver setup information during PTR in February 2010.

Sweep	10 – 100 Hz
Taper	500 ms
Sweep length	10 s
Record length	12 s
Sample rate	1 ms
Physical channel spacing	25 m
Effective channel spacing	12.5 m
Number of channels	60
Physical streamer length	1500 m
Effective streamer length	750 m

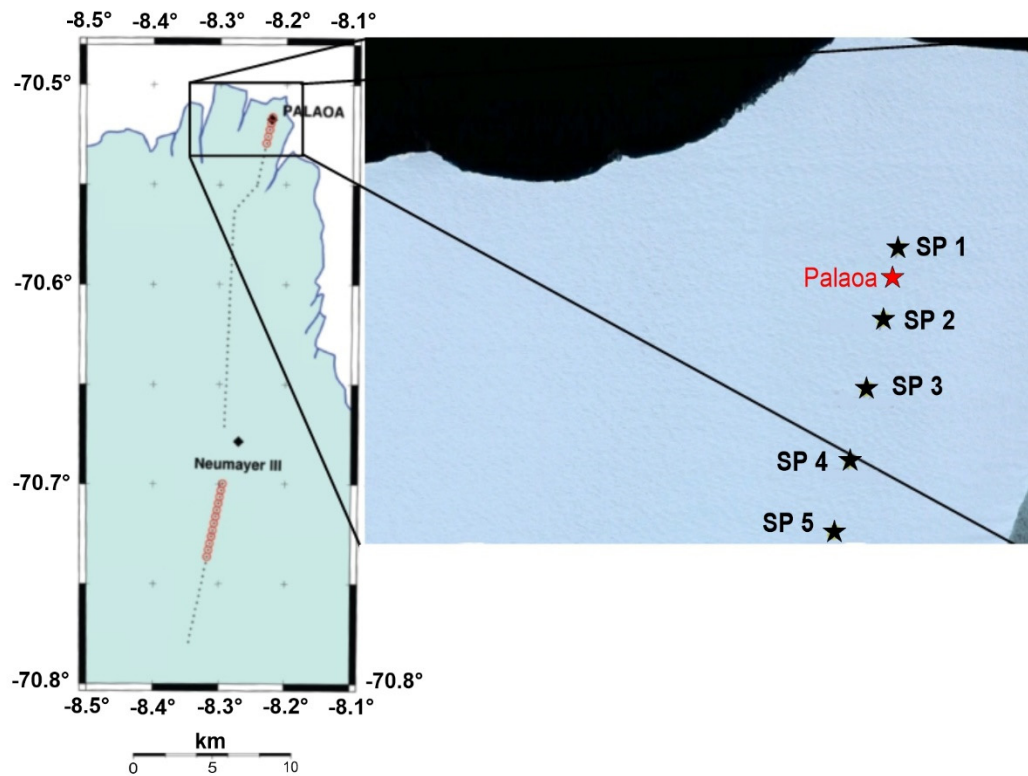


Figure 24: The Figure shows the first 5 shot points with each 4 shots (each 2 points with a distance of 6.25 m). Between every signed shot point is a distance of 375 m. The red star beneath PALAOA shows the locations where the hydrophone is placed in the water column (modified after Eisen et al., 2010a).

Several processing steps from the streamer data were applied by Dr. Emma Smith and Dr. Coen Hofstede at AWI to create a seismic profile. This was used to get a visual overview of the research area and to compare the thickness of the ice shelf and the water column with the calculated values of the single shots (chapter 4.1). The processing steps will not be explained here because it was not part of the thesis. We used the first six sweep locations of the PTR profile recorded by PALAOA hydrophone. Every sweep locations contains four sweeps. Detailed information about the different shots are shown in Table 2 below.

Table 2: Detailed information of several shots including their coordinates, time of triggering [UTC] and horizontal distance to PALAOA hydrophone [m]. Date of data acquisition was the 4th of February 2010.

Shot Point	Shot name	Time [hh:mm]	PALAOA Offset [m]
1	PTR001a	20.41	130
1	PTR001b	20.45	123.75
2	PTR002a	21.50	247
2	PTR002b	21.53	253.25
3	PTR003a	22.24	615
3	PTR003b	22.27	621.25
4	PTR004a	22.52	991
4	PTR004b	22.54	997.25
5	PTR005a	23.19	1369
5	PTR005b	23.21	1374.25
6	PTR006a	23.53	1774
6	PTR006b	23.56	1780.25

3.3 Travel time and ray path calculations

Several studies roughly indicate values but especially the mean P- and S-wave velocities within the ice body need to be accurately known. To calculate the correct ray paths and travel times, detailed information about the thickness and velocity of the ice and water body are necessary. To accomplish this, we use the streamer data. With familiar source and streamer geometry, the P- and S-wave velocities can be calculated in a first step. The velocities are necessary for calculating further the ice shelf thickness and the depth of the seafloor. All four shots of each of the first six shot points are spectated. Figure 25 below shows the first two shots of the survey (PTR001b) acquired with the 60 channel snow streamer, processed by Dr. Emma Smith and Dr. Coen Hofstede.

To calculate the compressional and shear wave velocity within a medium, the direct P-wave and direct S-wave can be examined. Both are identifiable by a linear trend in time and distance. Other reflections are visible as hyperbola (see Figure 25 and also Figure 13 in chapter 2.2). As the Vibroseis truck is located at the surface, the direct waves travel along a ray path at the snow surface to the geophones. Its velocity v can be calculated by the equation:

$$v_{p,s} = \frac{s_2 - s_1}{t_2 - t_1} = \frac{\Delta s [m]}{\Delta t [s]} = \frac{\Delta x}{\Delta y} \quad (3.3.1)$$

The variable x indicates the distance s [m] and y gives the travel time t [s]. Note, that Figure 25 shows the two-way travel time but for calculating the velocity, one-way travel time has to be used. To get values for $x_{1,2}$ and $y_{1,2}$ a horizon can be picked (Figure 25) along the identified P- and S-wave. Every shot point contains 2 locations with a distance of 6.25 m (Table 2). Because this displacement has no significant impact on the whole travel path of the seismic rays, both locations (e.g. PTR001a and PTR001b) build one shot point and its offset to PALAOA is assumed to be 130 m. Each shot contains 2 vibration shots, so every shot point contains 4 shots (e.g. shot point one contains 2 shots at PTR001a and PTR001b). The shot with the best visible data at every shot point was used to calculate the velocities. This gives six values for the P- and S-wave velocity in ice and the ice thickness along the survey direction.

The ice base marks the interface between the ice shelf layer and the water column. To get information about the ice thickness, two different signals can be used: the difference of the multiple P-wave reflection of the ice base and the seafloor reflection and further the S-wave reflection of the ice base. The reflection from the ice base of the P-wave can't be used because its arrival superimposes with several surface waves so it is quite difficult to distinguish between the signals. Both signals are visible as hyperbolic reflections in the data. The reflection from the ice base of the S-wave occurs later because of its lower velocity. The ice base reflection of the S-wave is very distinctive because of the high amplitudes of the S-waves. By converting the equation 3.3.1 the ice shelf thickness can be calculated with now familiar information about the velocity and the two travel time through the ice shelf.

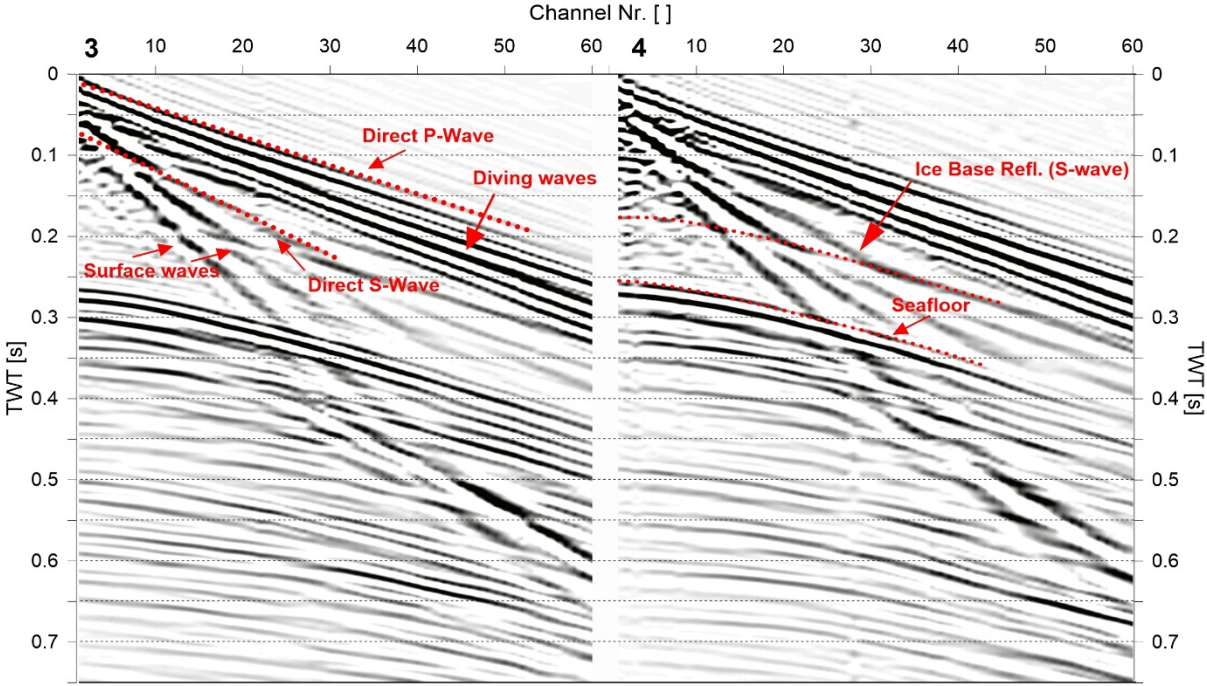


Figure 25: Shot gather of Vibroseis shots 3, 4 (PTR001b) measured by the surface streamer containing 60 channels. Dashed red lines mark direct waves and reflections caused by P- and S-waves. X-axis shows resorted streamer channel numbers 1-60, y-axis shows two-way travel time in seconds.

In the streamer data, the direct P-wave is characterized as the first arriving signal and constitutes a linear signal in the shot gather, followed by later arriving and bended diving waves (Figure 12). The direct S-wave and surface waves are also characterized by a linear shape but with a larger time delay and higher amplitudes. The direct S-wave is faster than the surface waves. Reflections occur in a hyperbolic shape caused by the *Normal Move Out* (NMO). This is clarified by an increasing time delay of a horizon (e.g. the ice base reflection) because of the increasing travel path caused by an increasing distance of the channels to the source.

Because the PALAOA hydrophone stays within the water column, the rays follow a different travel path as if they are recorded with surface geophones. The rays propagate through the ice shelf layer into the water column refracted based on *Snell's Law* (chapter 2.2). The theoretical ray paths are derived below. The simplest path is the direct one, which is just refracted at the ice – water interface and thus different to the direct wave recorded by surface geophones. Other ray paths, (=“events”) which include multiple reflections, and their travel times can be theoretically calculated, according to the actual geometry (Figure 26-28).

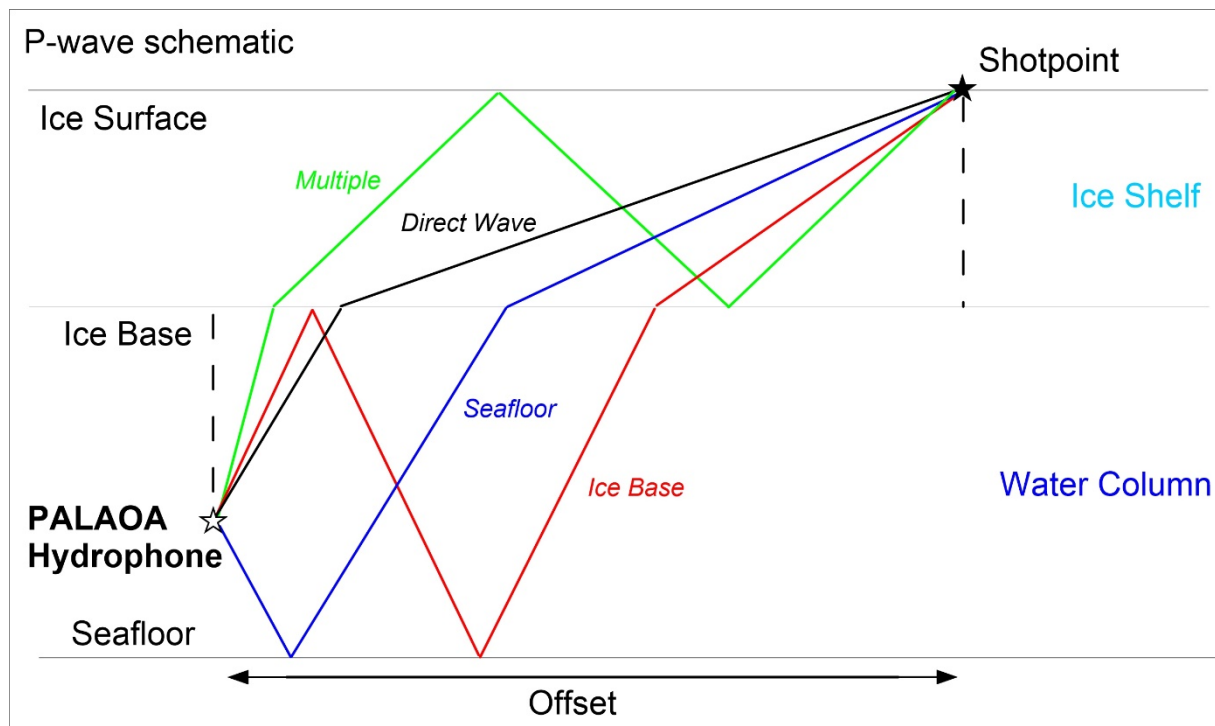


Figure 26: Rays of P-waves which propagate from the shot point at the ice surface to the PALAOA hydrophone through the ice shelf and are refracted at the ice base. Based on their different travel path, the traveltime of different events can be calculated. The reflection and refraction angles do not match the real values because the sketch just illustrates the theoretical shape of the ray paths. Colours indicate different paths with the names indicated as used in the text.

The geometry of the PALAOA experiment is well constrained, because the lateral and vertical position of the hydrophone is known as well as the ice shelf thickness and water depth, so the theoretical ray paths and travel times of different events can be calculated. The ray paths can be calculated theoretically by dividing them into two areas given by the ice shelf and water column medium. As shown in Figure 27, the ray path can be expressed as the hypotenuse of two rectangular triangles whose shapes are based on the incident and refracted angle at the ice – water interface, which again depends on the medium velocities and *Snell's Law*.

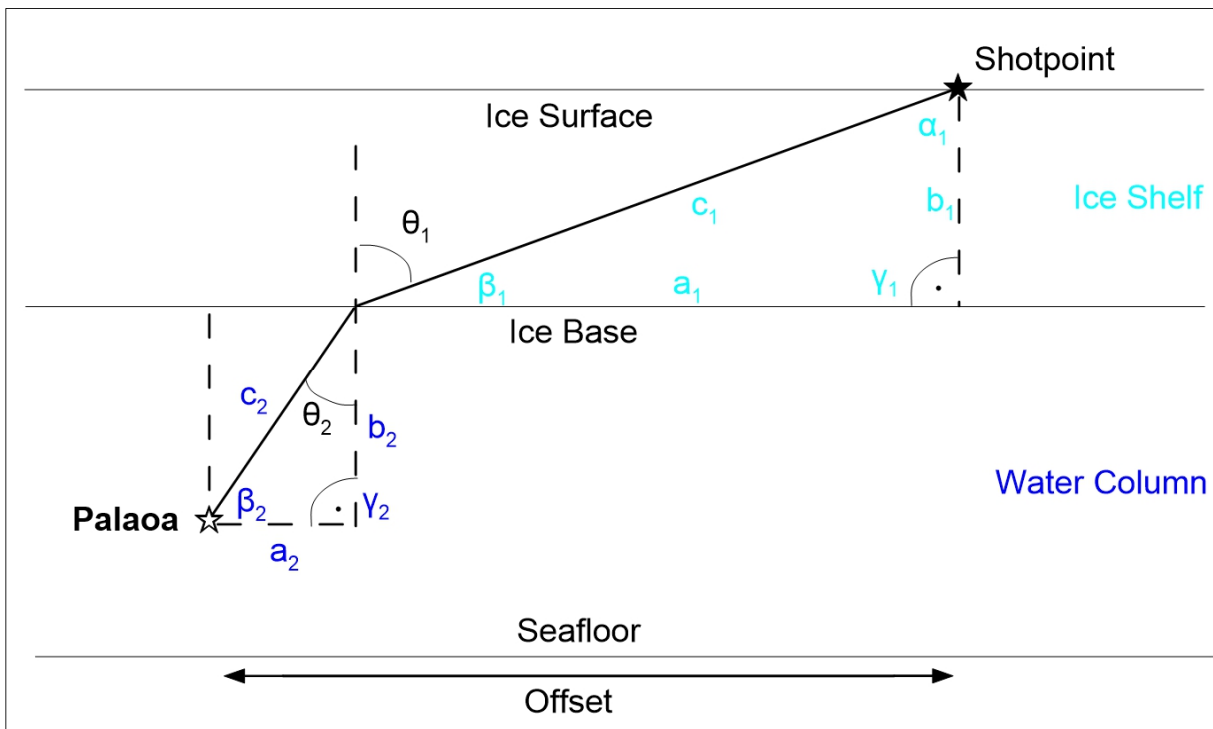


Figure 27: Mathematical principle for the P-wave ray path and travel time calculation. The ray path corresponds the hypotenuse of two rectangular triangles in the ice and water column and thus became the sum of c_1 and c_2 . The angles within the triangles base on θ_1 and θ_2 that once again base on the seismic velocities.

Because the interfaces at the ice – air, ice – water and water – seafloor are assumed to be perfectly horizontal, the triangles comply the principle of Pythagoras so the hypotenuses of the triangle in the ice becomes (Figure 27):

$$c_1 = \sqrt{a_1^2 + b_1^2}. \quad 3.3.2$$

With the distances a , b and c , and for the triangle in the water:

$$c_2 = \sqrt{a_2^2 + b_2^2}. \quad 3.3.3$$

Because of geometrical conditions, the incident angle θ_1 matches α_1 in *triangle 1* (in the ice). The angle β_1 is given with respect to the knowledge of α_1 and γ_1 . Because the distance b_1 matches the available ice thickness, the distance a_1 (further “*Offset ice*”) can be calculated with:

$$a_1 = \frac{b_1 * \sin \alpha_1}{\sin \beta_1}. \quad 3.3.4$$

Therefore the hypotenuse c_1 becomes the combination of equations 3.3.2 and 3.3.4 as:

$$c_1 = \sqrt{\left(\frac{b_1 * \sin \alpha_1}{\sin \beta_1}\right)^2 + b_1^2}. \quad 3.3.5$$

Comparable conditions are valid in *triangle 2* in the water. The angle of refraction θ_2 is known to depend on *Snell's Law*. With respect to rectangle conditions, β_2 becomes

$$\beta_2 = 180^\circ - \theta_2 + \gamma_2, \quad \text{with } \theta_2 = \alpha_2. \quad 3.3.6$$

The distance b_2 matches the depth of the PALAOA hydrophone. The information is given by Kindermann et al. (2008) and Eisen et al. (2010a). Therefore, the distance a_2 forms the “*Offset water*” and can be calculated with:

$$a_2 = \frac{b_2 * \sin \alpha_2}{\sin \beta_2}. \quad 3.3.7$$

As in equation 3.3.5, the hypotenuse c_2 becomes the summary of equation 3.3.3 and 3.3.7 as:

$$c_2 = \sqrt{\left(\frac{b_2 * \sin \alpha_2}{\sin \beta_2}\right)^2 + b_2^2}. \quad 3.3.8$$

Finally the ray path x becomes the sum of both hypotenuses (equation 3.3.5, 3.3.8) as:

$$x = \sqrt{\left(\frac{b_1 * \sin \alpha_1}{\sin \beta_1}\right)^2 + b_1^2} + \sqrt{\left(\frac{b_2 * \sin \alpha_2}{\sin \beta_2}\right)^2 + b_2^2}. \quad 3.3.9$$

With given parameters for ice shelf b_1 and water column b_2 thickness, velocities for each medium and the offset (horizontal distance between the shot points and PALAOA location, the sum of a_1 and a_2), there is just one possible ray path that exactly reaches the hydrophone. Its ray path can be calculated with respect to *Snell's Law*. All calculations can be found in the appendix. Three more events are characterized: (1) The ray path “*Multiple*” that travels from the source to the ice base, reflecting back to the surface, reflecting again at the ice – air interface

and then propagates to the PALAOA hydrophone with a refraction at the ice – water boundary. (2) The event “*Seafloor*” that describes a ray refracting at the ice – water interface and then reflecting at the seafloor. (3) The finally event is the “*Ice Base*” that follows the “*Seafloor*” event and afterwards reflecting back at the water – ice interface down to the PALAOA hydrophone (Figure 26).

As the sweeps generated both P- and S-waves, we also derived the ray paths for generated S-waves which were converted into P-waves at the ice - water interface. The experiment has the same geometry (source, hydrophone location etc.) but the shear waves have a lower velocity in ice than compressional waves in water. This leads to different incident and refracted angles at the ice – water interface and so the ray paths theoretically follow a geometry as schematically shown in Figure 28 below.

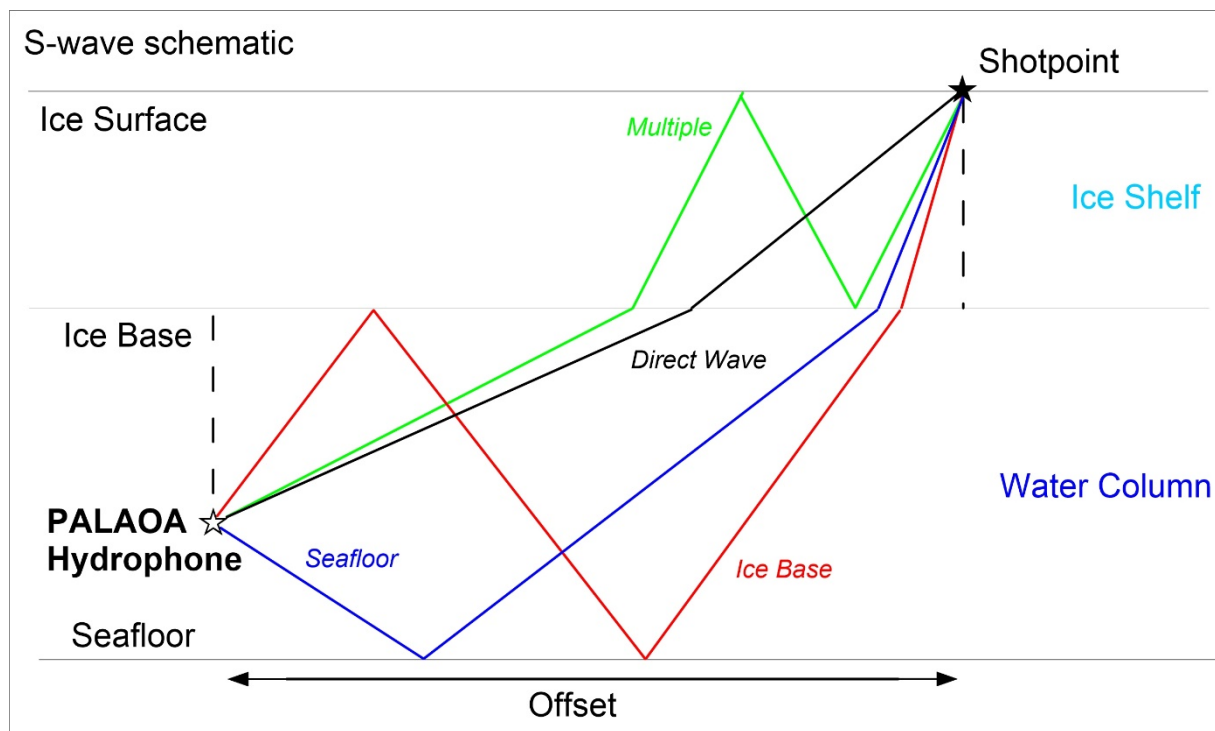


Figure 28: S-waves propagate from the shot point at the ice surface to the ice base and cause a SP-conversion. In the water column they continue as P-waves to the PALAOA hydrophone. Basing on their different travel path, the travel time of different events can be calculated. The relations, reflection and refraction angles do not match the real values because the sketch just illustrates the theoretical shape of the ray paths.

3.4 First arrival analysis

The PALAOA hydrophone records continuously. The data provided for the study are converted segy-files of the audio data of PALAOA that contain a time window of 20 seconds that include the Vibroseis sweep. There is no synchronisation between the hydrophone and the source

triggering a sweep so the signals have to be corrected to the same time level manually. More specifically, the first arriving signals were approximately identified, correlated with a synthetic source sweep and reduced to an identical time window (Figure 29). As P-waves are the fastest ones, the first arrival of each shot has to be the “*direct*” P-wave which was only refracted at the ice base (Figure 26). After the signal identification and timing correction all shots are set to the same time (Figure 29). The events can be identified based on their ray paths and thus travel times with respect to the arrival of the direct P-wave.

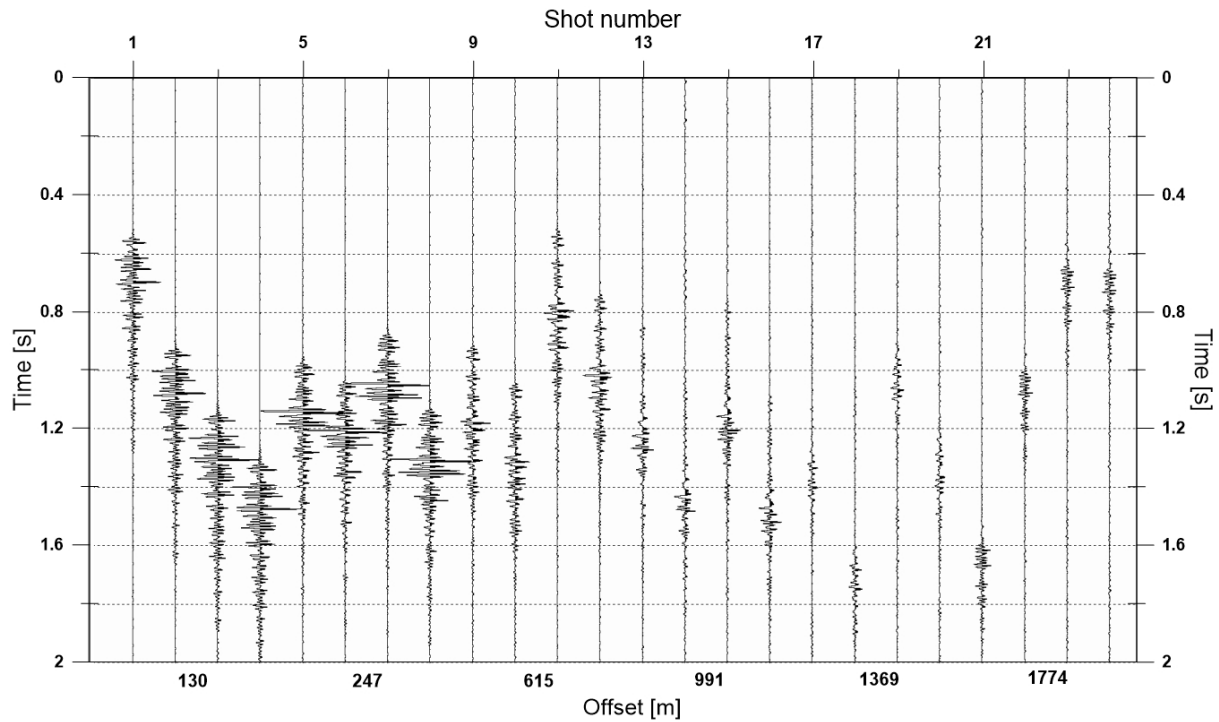


Figure 29: Cross-correlated Vibroseis shots 1 - 24 recorded at PALAOA. The time windows of 10 s include the arriving signal. The signals have to be statically corrected manually.

3.5 Amplitude calculation

Three different amplitude calculations are made for four different events at 6 shot points with each 4 shots: (1) Maximum amplitude (Max Amp.) that calculates the largest value of a single peak. (2) Root-Mean-Square amplitude (Rms. Amp.) that is defined as the arithmetic mean of a square of a set of numbers and thus in this case the set of amplitudes within a single peak. (3) Average amplitude (Avg. Amp.) calculates the arithmetic mean of a set of amplitudes within a single peak over a specified time (in the following = time average).

After calculating the travel times, the peak and thus the event can be identified in the seismogram. A time window (usually some milliseconds) is set that contains the whole identified peak in the seismogram (Figure 30). Within this peak, all amplitudes are used for calculating the RMS- and Avg. amplitude value. The highest value within this time window

comes up to the Max Amp. value for the event. Absolute values are used, so negative amplitudes become positive. This is made for eight events at six locations. The peak of each event is observed and the starting and ending time is used to calculate all three amplitudes within this time gate. For example at shot point one, the *pp-Multiple* event arrives at a time of 0.061 s after the *pp-Direct* wave (Figure 30). There is a negative peak with a maximum at $t = 0.062$ s in the seismograms of the shots 1 and 3. This event is identified as the Multiple P-wave. The negative peak appears between 0.056 s and 0.064 s. This values are used as the borders of the time window for calculating the amplitudes for this event. The time windows base on the shape of the peaks. If the peak is wider, the number of samples within the peak increases.

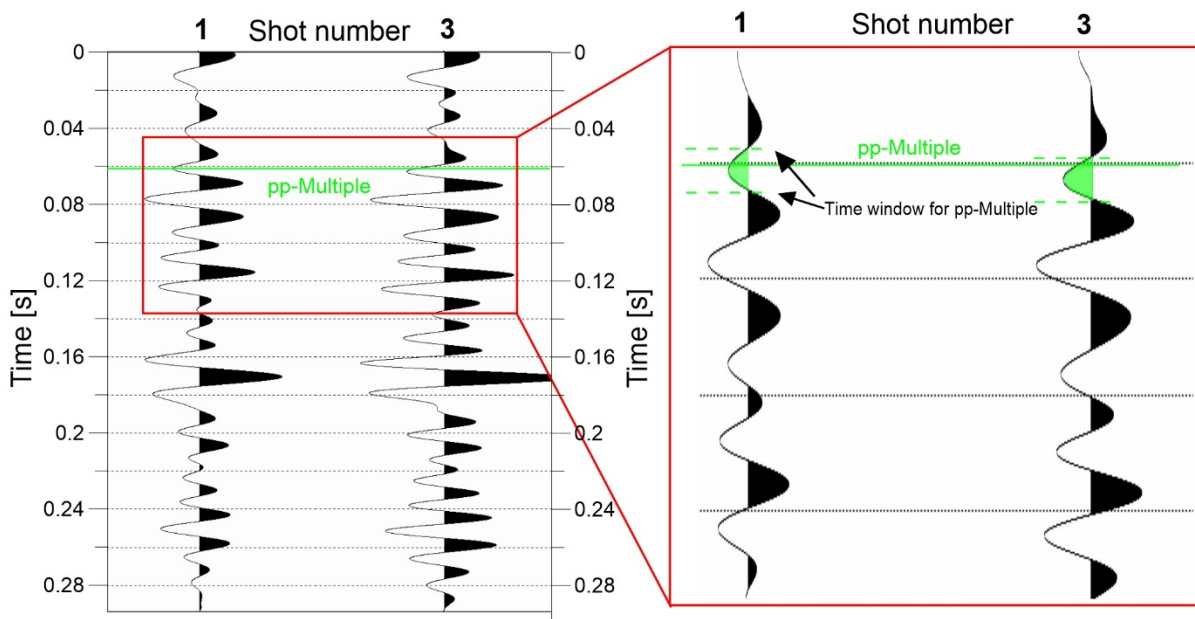


Figure 30: Example of amplitude calculations for the *pp-Multiple* event at shot 1 and 3. The right window is a part of the whole seismogram (left). The greenish area marks the peak. All amplitudes within this area, restricted by the dashed lines, are taken into account for the calculations. Y-axis shows travel time [s].

4. Results

The primary aim of the thesis is to identify different events in the seismograms and to calculate their amplitudes. This chapter is structured as the following: At first, the ice thickness and the P-wave and S-wave velocities of the ice are calculated by the shot gathers of the streamer data. With this information, the ray paths and travel times of different events are calculated to identify them in the seismograms. After identification of the events, three different amplitudes of each event at different offsets are calculated.

Two shots were triggered at the same point and another two with a distance of 6.25 m while the streamer stayed at the same position to simulate a 120 channel streamer. Spatial difference is further not considered as the difference of 6.25 m does not make any significant changes in the travel times but it simplifies assumptions and evaluations so each shot point assumes to contain

four shots at exactly the same location. It can be recognized with respect to Figure 31 below as the signals occur in a group of four with more or less the same shape. First impressions indicate that the main signal arrives in an increasing time delay with an increasing offset. While four shots show peaks with comparable amplitudes at exactly the same time these cannot be followed within the signals of larger offsets. To identify different events, their travel time is calculated for each offset.

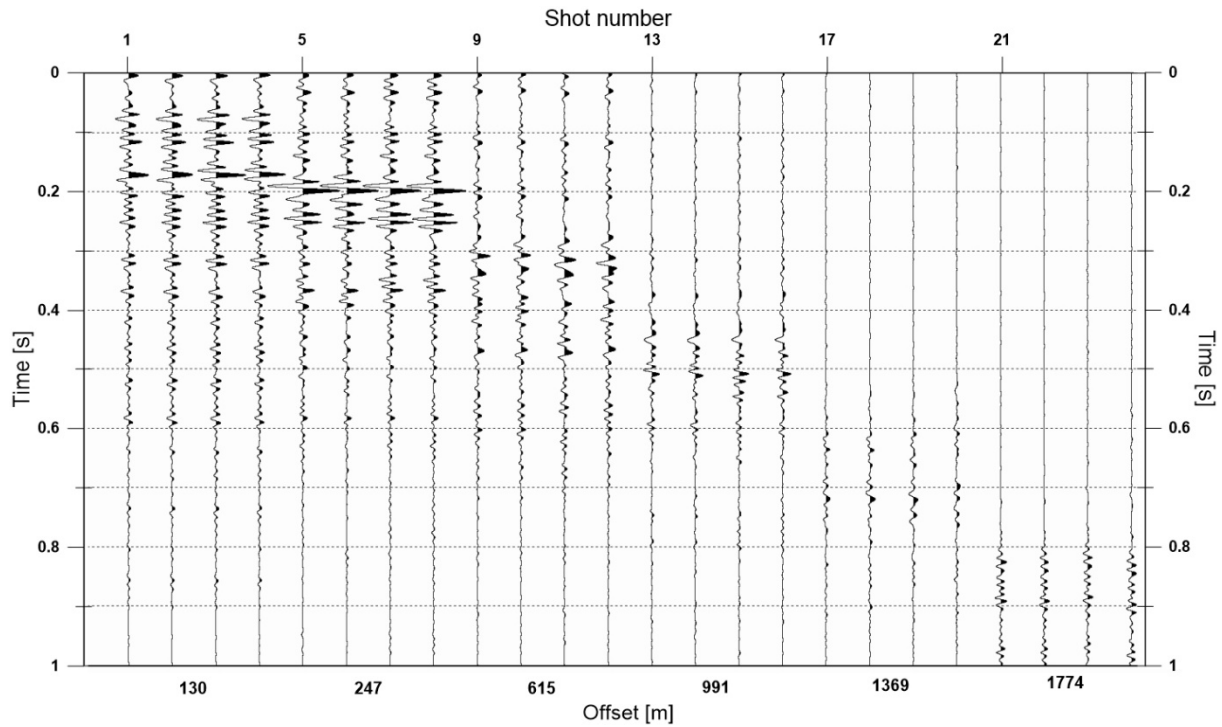


Figure 31: Visualisation of the first 24 Vibroseis shots after time correction recorded with PALAOA. The first arriving signal is identified and set to $t = 0$. Titles and axis labelling is manually modified afterwards. The lower x-axis illustrates the horizontal (not including vertical) distance of the shot point to the hydrophone. Note that four shots were triggered at the same point (and thus offset). The upper x-axis indicates the shot number of each single shot. Y-axis show the one-way travel time [s].

4.1 Timing correction and geometry

Each shot point location contains four Vibroseis shots in the following, all four shots at each offset are named as shot group 1 - 6. In the streamer data, shots with the best data quality each shot point are used to identify the direct P- and S-wave and furthermore the ice base reflection to calculate the velocities and ice thickness (see Figure 22). The shots for analysis were chosen regarding their visual quality and ability of event identification. The results of the velocities and ice thickness are listed in Table 3.

Table 3: Calculated, non-averaged, P- and S-wave velocities [m/s] and the ice shelf thickness [m] based on streamer data analysis (Figure 25):

Shot group []	Offset [m]	v_p [m/s]	Ice thickness [m]	v_s [m/s]	Ice thickness [m]
1	130	3550	122	1329	126
2	247	3571	122	1327	123
3	615	3594	124.9	1339	119
4	991	3627	120.6	1322	115
5	1369	3584	124.5	1310	123.7
6	1774	3753	132	1331	128.5

The P-wave velocity varies between 3550 and 3753 m/s and the S-wave velocity between 1310 and 1339 m/s. The ice thickness is calculated with equation 3.3.1. It depends on the picked velocities of the shot gathers and the two-way travel time of the ice base reflection measured by the first channel. The ice base reflection caused by the S-wave is extremely sharp in all shot gathers and thus useful to calculate the ice thickness. Its values vary between 115 and 128.5 m. This furthermore gives a hint for the two-way travel time of the P-wave ice base reflection. Based on its velocity it has to occur at 0.06 - 0.08 s TWT in the shot gather. Table 3 shows the raw calculated values at each offset. Because the rays do not pass the ice - water interface directly below the shot point (Figure 26, 28), the values for the P-waves, S-waves and the ice thickness are averaged and listed in Table 4 (e.g. the P-wave velocity for rays triggered at an offset of 247 m is the average of the calculated P-wave velocity at an offset of 130 m and 247 m, etc).

Table 4: Averaged values of the parameters summed in Table 3 for all offsets; the average ice thickness contain both values calculated by P-wave and S-wave velocity:

Shotpoint []	Offset [m]	Avg v_p [m/s]	Avg v_s [m/s]	Avg Ice Thickness [m]
1	130	3550	1329	124
2	247	3560	1328	123
3	615	3572	1331	123
4	991	3585	1329	123
5	1369	3585	1326	123
6	1774	3613	1327	123

4.2 Ray paths and travel times

With the given information by Eisen et al., (2010a) and Smith et al., (2019) the ray paths and travel times can be calculated. Table 5 sums the parameters the calculations are based on.

Table 5: Summary of necessary parameters and their reference literature as the base for ray path and travel time calculations:

Parameter	Reference	Value
Ice shelf thickness [m]	Calculated	123
Water column [m]	Eisen et al. (2010a)	150
PALAOA above seafloor [m]	Eisen et al. (2010a)	69
v_p (ice) [m/s]	Calculated	3550 - 3753
v_s (ice) [m/s]	Calculated	1326 - 1331
v_p (water) [m/s]	Smith et al. (2019)	1451

Based on the given and calculated parameters, the equations 3.3.2 to 3.3.9 are used to calculate the ray paths and travel times to the hydrophone of different events. Their characteristics can be recognized in Figure 26 – 28 above. The resulting values are listed in Table 6.

Table 6: Summary of the calculated values for the length of the ray path x [m] and the corresponding total travel time t [s] at six shot points (SP) [] / offsets [m] with use of values shown in Table 4 and 5:

Event		Offset [m] SP Nr []					
		130 / SP 1	247 / SP 2	615 / SP 3	991 / SP 4	1369 / SP 5	1774 / SP 6
pp-Direct	x [m]	246	335	681	1052	1427	1832
	t [s]	0.104	0.131	0.228	0.331	0.435	0.544
pp-Seafloor	x [m]	368	442	774	1143	1518	1922
	t [s]	0.195	0.221	0.317	0.419	0.524	0.631
pp-Ice Base	x [m]	523	577	884	1252	1625	2028
	t [s]	0.305	0.329	0.421	0.523	0.628	0.733
pp-Multiple	x [m]	466	516	778	1114	1473	1866
	t [s]	0.108	0.180	0.254	0.347	0.448	0.553
sp-Direct	x [m]	241	320	651	1020	1396	1802
	t [s]	0.175	0.234	0.471	0.731	0.994	1.261
sp-Seafloor	x [m]	364	422	704	1051	1417	1817
	t [s]	0.260	0.303	0.504	0.750	1.007	1.271
sp-Ice Base	x [m]	519	561	795	1113	1462	1850
	t [s]	0.346	0.399	0.566	0.791	1.037	1.293
sp-Multiple	x [m]	467	512	762	1091	1452	1857
	t [s]	0.366	0.381	0.565	0.807	1.066	1.338

The results of Table 6 are visualised in Figure 32 below. Different events caused by P-waves in the ice column (further “pp-event name” events) show an almost linear shape between the

increasing shot point offset and the travel time. S-waves converted to P-waves at the ice-water interface (further “sp-event name” events) show larger travel times caused by the lower velocity within the ice column. The relative time differences between the P-wave events do not change significantly with increasing offsets. This is also recognizable for the S-wave events. This becomes clearer, depicting the relative travel time difference between the events with respect to the first arrival of the P-wave (Figure 33).

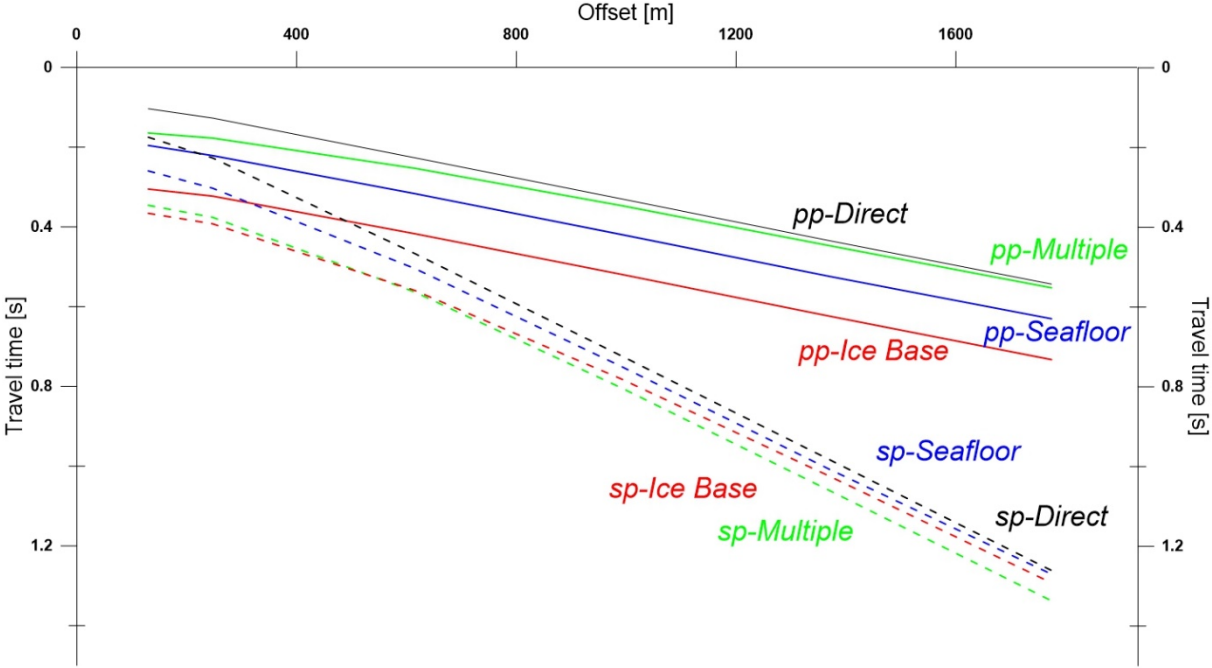


Figure 32: Absolute travel times of different pp-events (straight lines) and sp-converted events (dashed lines) based on values from Table 6. X-axis shows the offset [m] as the horizontal distance between the shot point and PALAOA. Y-axis show the travel time [s].

Table 7: Relative time delays [s] of events with respect to direct P-wave arrival for each offset (= time difference between P-wave travel time and particular event travel time):

Event	Offset [m]					
	130	247	615	991	1369	1774
pp-Seafloor	0.092	0.091	0.089	0.089	0.088	0.087
pp-Multiple	0.061	0.050	0.027	0.017	0.012	0.009
pp-Ice Base	0.201	0.196	0.190	0.189	0.189	0.189
sp-Direct Wave	0.071	0.100	0.240	0.394	0.549	0.718
sp-Seafloor	0.156	0.172	0.277	0.419	0.572	0.728
sp-Multiple	0.242	0.249	0.337	0.474	0.626	0.794
sp-Ice Base	0.262	0.265	0.333	0.452	0.590	0.749

As the previous results show, the direct P-wave is the first signal arriving at PALAOA (Table 6, Figure 32). It's travel time is subtracted from the travel time of events at the same offset and thus gives a relative delay for each following event. The arriving pp-events reach the hydrophone at relative time delays between 0.005 s (*pp-Multiple* at large offsets) and 0.201 s (*pp-Ice Base*). SP-events however reach the hydrophone at travel times between 0.070 s (*sp-Direct* wave at small offset) and nearly 0.800 s (*sp-Ice Base*, *sp-Multiple* at large offsets). The *pp-Multiple* is the first signal that arrives after the *pp-Direct* wave. Whereas all events reach the hydrophone in a delay between 0.061 and 0.262 s for the smallest offset, the time differences between pp-events and sp-events increases with an increasing offset.

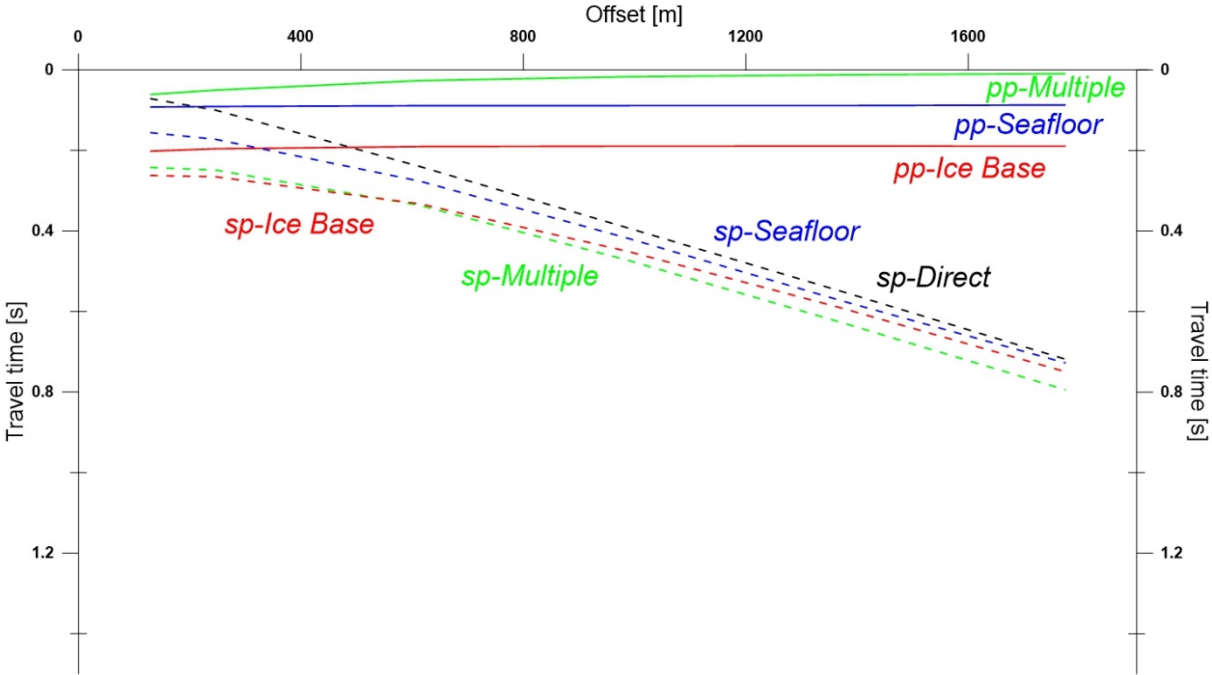


Figure 33: Relative travel times (time delay) of different pp-events (straight lines) and sp-converted sp-events (dashed lines) with respect to the direct P-wave travel time for each offset depending on the values listed in Table 7. X-axis shows the offset [m] as the horizontal distance between the shot point and PALAOA. Y-axis show the travel time [s].

To identify the events in the seismogram, the travel time curves are inserted into the seismograms. Figure 34 gives an overview of the evaluated results.

4.3 Event detection

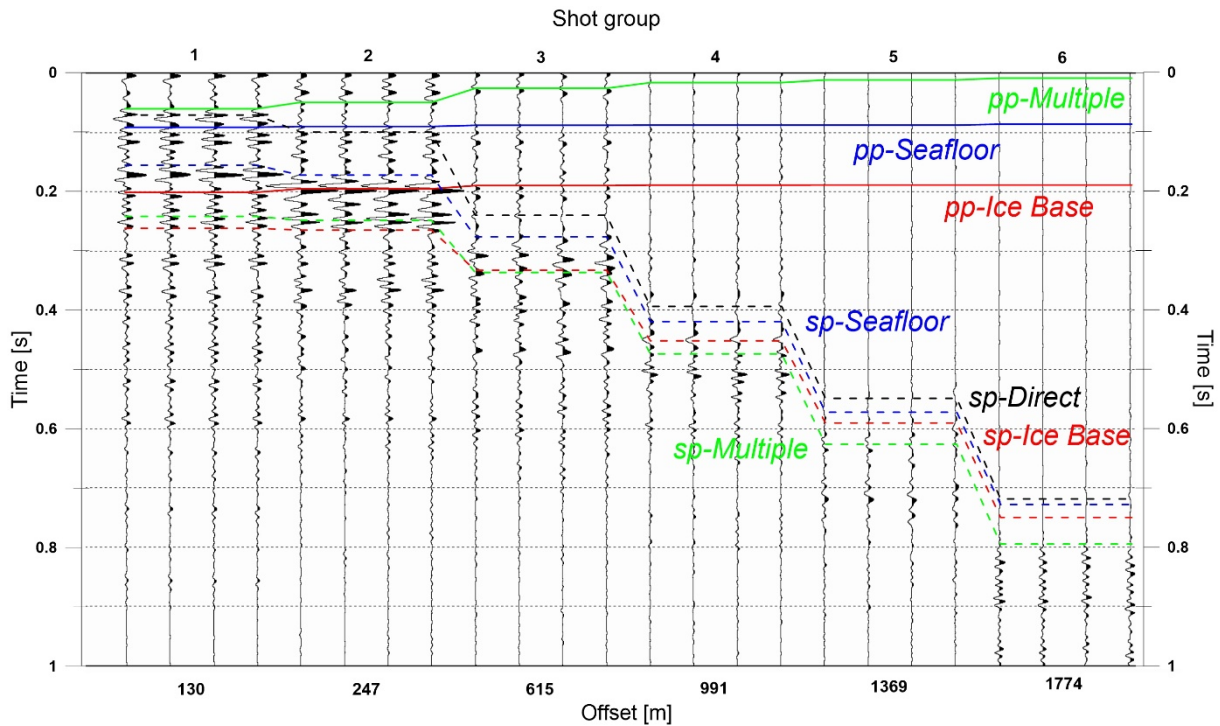


Figure 34: Relative travel time of different events with respect to direct P-wave travel time and their arriving point in the corresponding seismograms. Upper x-axis shows the shot group containing 4 shots (so shot group 1 matches shot point location 1). Lower x-axis indicates the horizontal offset of a group of four shots. Y-axis show the travel time [s]. Event names were explained within the Figures 26 and 28. Because four shots are in one shot point and grouped, they have the same offset which increases linearly by more or less 375 m between the groups. The ray paths, travel times and the time differences appear similar in each group, but in a different step-like shape between groups (in comparison to Figure 32 and 33 which had continuous offsets).

The travel times for the events are the same in each shot group. The offsets increase to the next shot group and location. This forms a stepwise increase of time delay for the sp-events (Figure 33). Seismograms of shots with small offsets (130 m, 247 m) illustrate that the calculated travel times for the events match the main signal (so the strongest peaks). With an increasing offset the main signal appears at an increasing time delay also like the sp-events. However, the travel time of the events do not match with the strong peaks at larger offsets. As the time delay of the pp-events does not increasing with larger offsets, their signals appear in the upper part (< 0.2 s) of the seismograms and thus they do not match with the strong peaks. In the following the shot groups will be investigated in more detail.

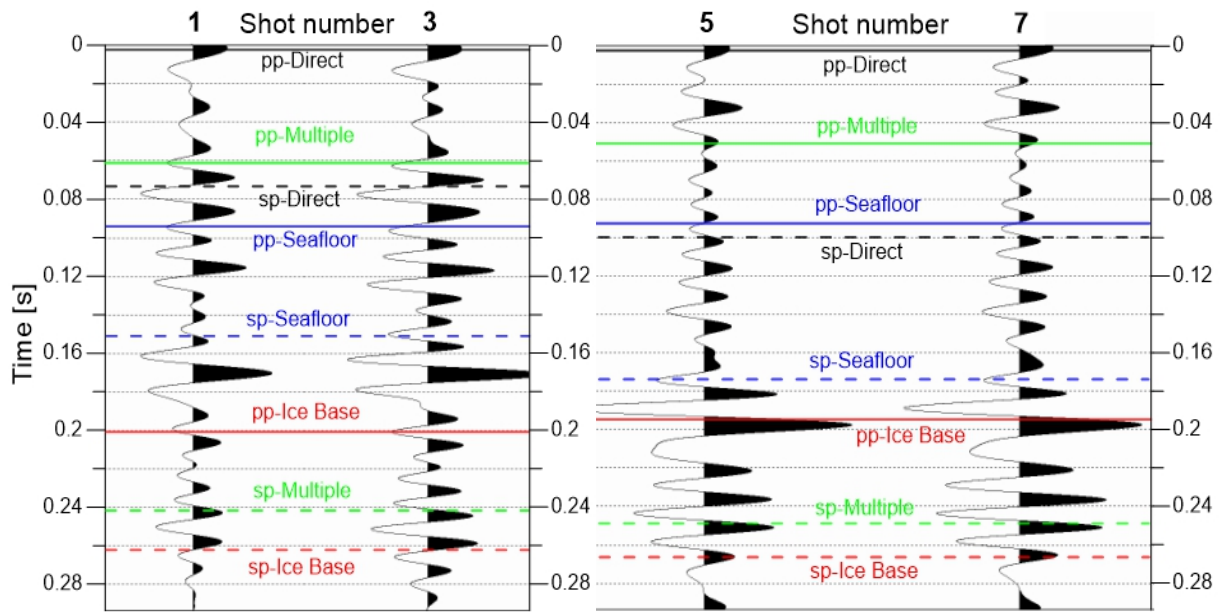


Figure 35: Particular view of Vibroseis shots 1, 3 at the first shot point (=130 m, left) and shots number 5, 7 at the second shot point (offset = 247 m, right) measured with PALAOA. Pp-Direct wave first arrival is set on $t = 0$. Coloured lines indicate the time of arrival of different events depending on their dime delay (see Table 7, Figure 32-34). Solid lines show pp events, dashed lines show sp events. X-axis shows the shot number; y-axis show the travel time [s]. Data plotting mode in the program is "Trace".

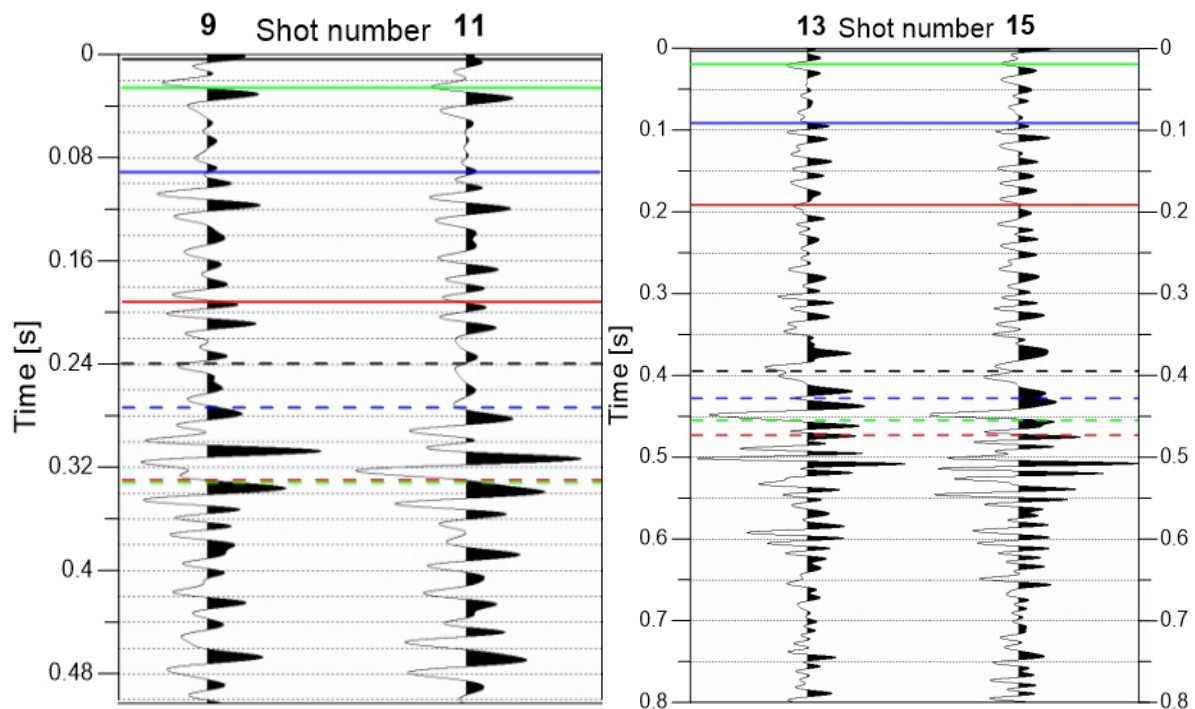


Figure 33: Particular view of Vibroseis shots 9, 11 at the third shot point (=615 m, left) and shots number 13, 15 at the fourth shot point (offset = 991 m, right) measured with PALAOA. Pp-Direct wave is set to $t = 0$. Coloured lines indicate the time arrival of different events depending on their dime delay (see Table 7, Figure 32-34). Solid lines show pp events, dashed lines show sp events. Compare Figure 35 for annotation.

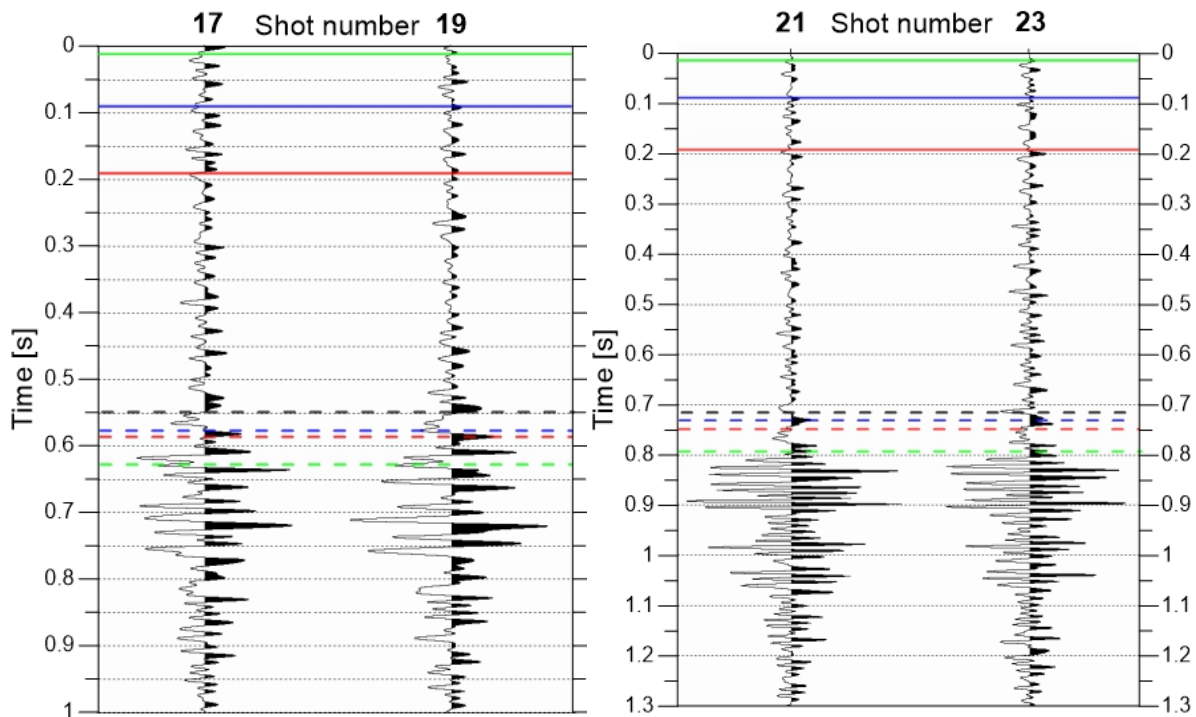


Figure 37: Particular view of Vibroseis shots 17, 19 at the fifth shot point (=1369 m, left) and shots number 21, 23 at the sixth shot point (offset = 1774 m, right) measured with PALAOA. Pp-Direct wave is set to $t = 0$. Coloured lines indicate the time arrival of different events depending on their dime delay (see Table 7, Figure 32, 34). Solid lines show pp events, dashed lines show sp events. Compare Figure 35 for annotation.

The seismograms of all four shots within a shot group at each shot point are similar with only minor differences. Amplitudes vary by a small magnitude only. However, seismograms of the different shot groups show large differences in the shape or amplitude of signals.

Shots 1 and 3 (Figure 34, 35 left) show four well defined and sharp positive peaks ($t = 0.068, 0.083, 0.118, 0.170$ s) except the first arriving signal. The peaks are always preceded and followed by a sharp but smaller negative peak. However, there is no synthetic event that matches with these peaks in timing.

The seismograms of the shots 5 and 7 (Figure 34, 35 right) have a different shape. There are not four major peaks but on extremely large and striking peak starting with a less strong negative peak at $t = 0.190 - 0.198$ s. Stronger signals of the shots 1 and 3 cannot be followed and thus identified in the seismograms of the shots 5 and 7. Shots of both offsets have the main signals over a time span of roughly 0.28 s.

The third shot point at an offset of 615 m (Figure 34, 36 left) shows seismograms with a generally weaker signal but several major events at $t = 0.035, 0.118, 0.279, 0.305$ and $t = 0.328$ s. Comparable to the shots 1 and 3 the positive peaks are preceded and followed by a weaker negative peak. However, the peaks do not match with the travel time of different synthetic events as it is also the case at the first offset signal.

The next shot point (offset = 991 m) shows a signal arriving in a delay up to 0.700 s with respect to the first arrival of the direct pp-event. Several stronger peaks appear between 0.380 and 0.600 s with partially stronger negative peaks (e.g. $t = 0.500$ s). Signals with smaller delays are weaker. Shots 17, 19 and 21, 23 at larger offsets of 1369 (Figure 37, left) m and 1774 m (Figure 37, right) show likewise seismograms as the shots 13 and 15. The main signal arrives at a delay of 0.550 to 0.900 (shots 17, 19) and 0.800 to 1.20 s (shots 21, 23) with respect to the first arrival of the direct pp-event. Four shots show several strong positive and negative peaks within these time spans. The previously arriving signals are very weak and thus hard to distinguish between event signals and background noise. At larger offsets pp-events and sp-events are visibly separated, but do not match with the strong main signals. Nevertheless, closest peaks to the predicted arrival time of calculated events are picked and analysed in the following section for further investigations.

4.4 Event Amplitudes

In total, 8 events were identified within 24 seismograms at six different offsets. In a first step the raw amplitude values for individual shots for pp-events (Figure 38) and sp-events (Figure 41) are presented. Furthermore, four values of each shot point (so each offset) are averaged (=shot group average. Notice: time average = Avg. amplitude over a specified time window in a single seismogram; shot group average = average amplitude value of an event in four seismograms of a shot group). This is made for three kind of amplitudes for each pp-event (Figure 39) and sp-event (Figure 42). Afterwards, the offset dependent percental distribution with respect to the direct waves for each pp-event (Figure 40) and sp-event (Figure 43) is analysed. To compare pp- and sp-events, four events of both wave types are summed within an individual Figure in a linear and logarithmic amplitude scale (Figure 44). All graphs are adjusted with a spline function that makes the graphs proper viewable. At an Offset of 615 m there was no peak identifiable for the *sp-Sea floor* and *sp-Ice Base* event so there is no data (Figure 41-43).

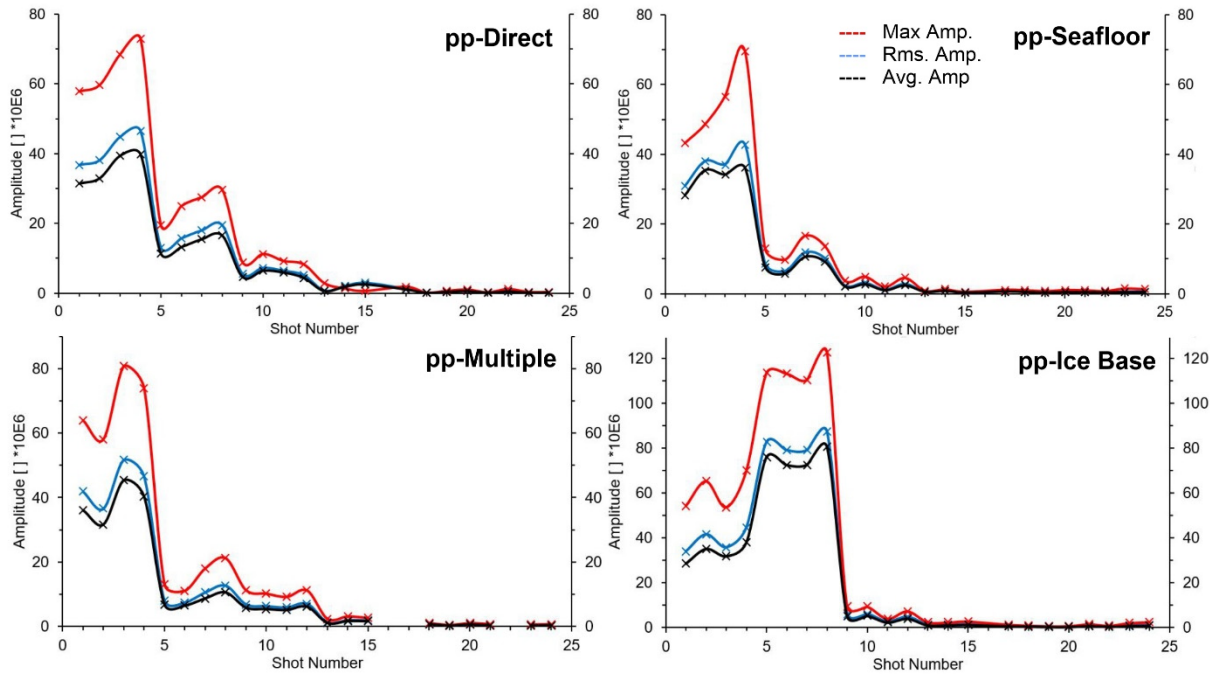


Figure 38: Illustration of raw amplitude values for pp-events for every shot. Every panel shows three amplitudes for a single event. Annotations are explained in the panels. X-axis illustrates dimensionless amplitudes without a unity. Y-axis indicates shot numbers 1-24. Note that there is no data in shot number 16 caused by a program error.

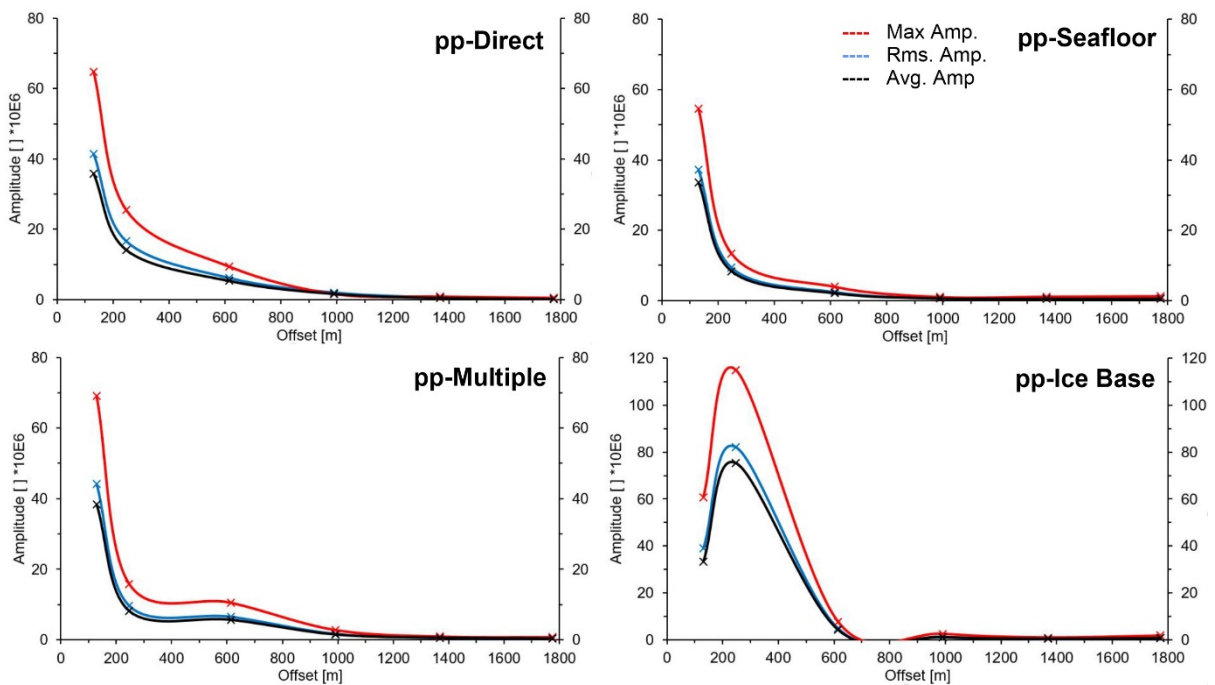


Figure 39: Illustration of shot group average amplitudes containing four shots each shot point. Every panel shows three amplitudes for a single event. Compare Figure 38 for annotations.

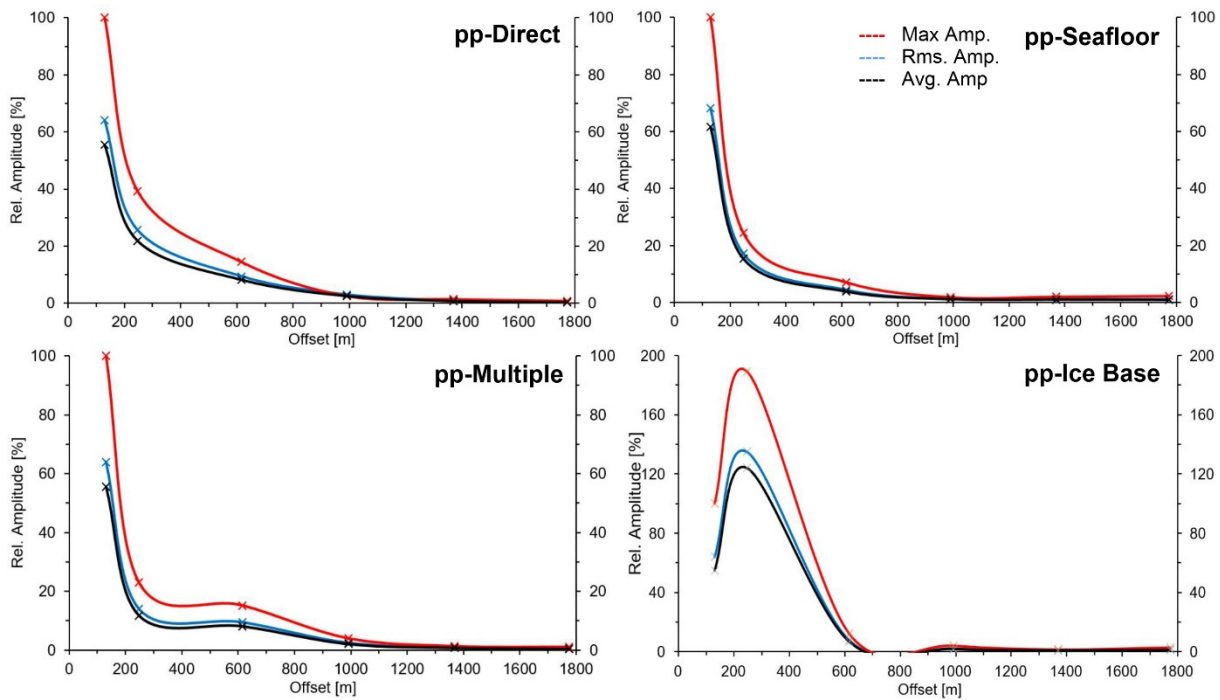


Figure 40: Illustration of percental shot group average amplitudes containing four shots each shot point. Maximum amplitude at the first offset is set to 100%. All values are normalised to this value. Every panel shows three amplitudes for an individual event. Compare Figure 38 for annotations.

Three different amplitudes for four events at 24 shot points (except shot 16) are evaluated. The amplitude values are dimensionless. There is no data at shot 16 because of an output error problem caused by the program so the shot group average amplitude values for the fourth offset of three shots instead of four is taken. The results show a general decrease in an exponential shape in the amplitudes with an increasing offset (in Figure 38 given by increasing shot numbers). Maximum amplitudes show the highest values whereas Rms. - and Avg. - amplitudes are smaller. Different amplitudes indicate equal trends with an increasing offset. The Maximum amplitude shows values between 58^6 - 72^6 at the first offset of 130 m. The Rms. - and Avg. amplitudes at the first offset vary between 30^6 - 48^6 whereat the Rms. amplitude is somewhat higher than the Avg. amplitude. The highest amplitudes can be seen at the shot points 3 and 4 for the events *pp-Direct*, *pp-Seafloor* and *pp-Multiple*. The *pp-Ice-Base* event shows maximum peaks for the shot numbers 5 – 8 up to values of 110^6 – 120^6 . This is visible as a strong peak in Figure 39. With larger distances to PALAOA (shot numbers 13 - 24) the amplitude values become less than 5^6 that makes the graphs difficult to distinguish and identify their trend. The general trend can also be recognized in the shot group averaged amplitude graphs (Figure 39) and their percental representation (Figure 40). In this Figure the Maximum amplitude at offset 1 is set to 100%. In all events the Rms. - and Avg. - amplitudes have an amount of 55-70% of the Maximum amplitude at the first offset. With an increasing offset up to 615 m (shot point 3) the relative amplitudes decrease to 10-20% and then become lower amounts of less than 10%.

The highest amplitudes are for the *pp-Ice-Base* in Figure 39 - 40 that matches the strongest peak in the seismogram.

Similar amplitude calculations are made for sp-events. The results are illustrated in the Figures 41-43. The events show basically an identical trend in form of decreasing amplitudes with an increasing offset similar to pp-events. There are partially stronger amplitude variations of single shots with similar offsets especially for the *sp-Sea-floor*, *sp-Multiple* and *sp-Ice-Base* at smaller offsets (see Figure 41). Similar to pp-events shots 3 and 4 show the largest amplitudes. The *sp-Direct* wave event shows higher values of 80^6 – 120^6 at an offset of 130 m whereas different events show comparable amplitudes of 35^6 – 80^6 . With larger offsets (991 m – 1774 m) the amplitudes decrease in a logarithmic trend and values of 1^6 – 5^6 (Figure 41, 42). The *sp-Sea-floor* event shows some variations in comparison to the *pp-Sea-floor* event as the amplitudes do not decrease that strong within the first three offsets (130 m – 615 m). Comparable to pp-events the Rms. – and Avg. amplitudes at the first offset vary between 55-65 % of the Maximum amplitude. Similarly at large offsets the amplitudes become 1 – 3.5 % of the first offset Maximum amplitude. As the values become very weak with large offsets, some events could not be identified within the seismogram (visible as missing dots in Figure 38).

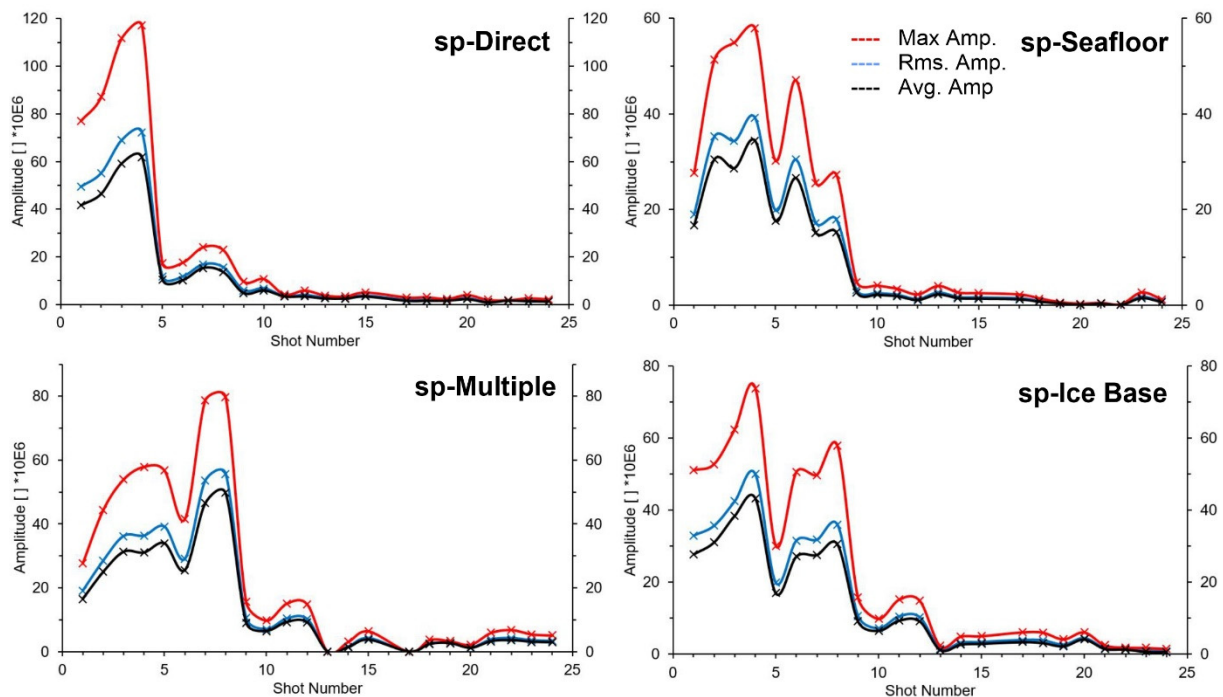


Figure 41: Illustration of raw amplitude values for sp-events for every shot. Every panel shows three amplitudes for a single event. Annotations illustrated within the panels. X-axis illustrates dimensionless amplitudes. Y-axis indicates shot numbers 1-24.

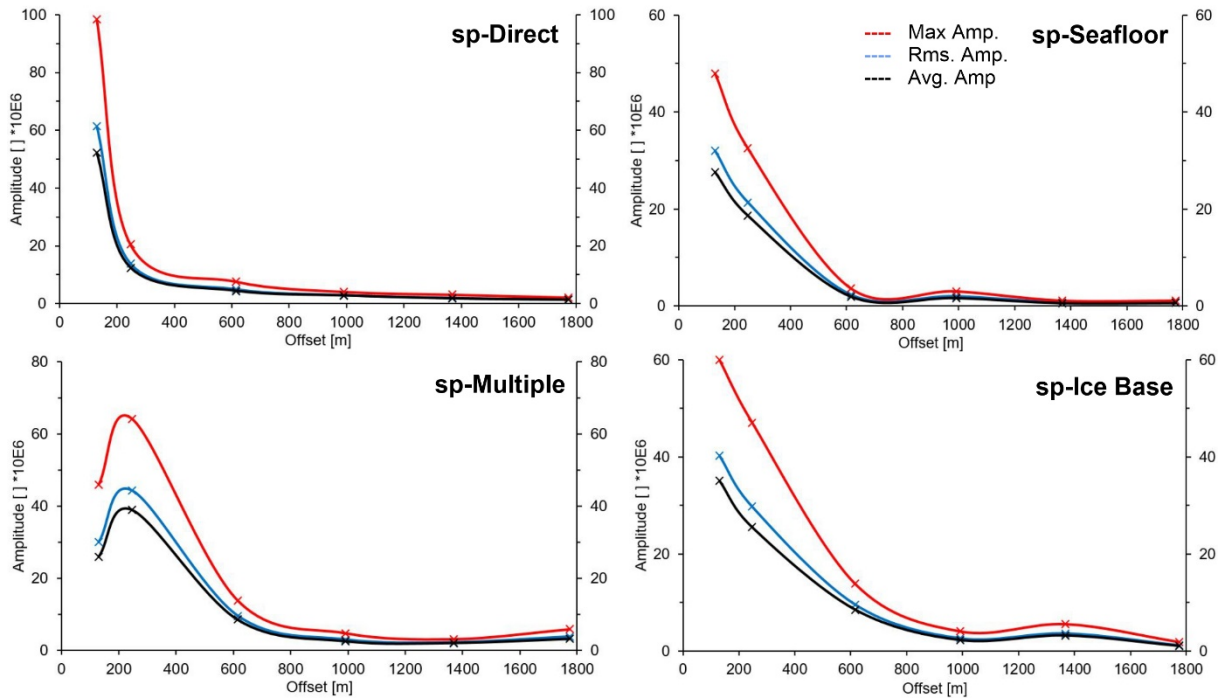


Figure 42: Illustration of the shot group averaged amplitudes containing four shots each shot point. Every panel shows three amplitudes for a single event. Compare Figure 41 for annotations.

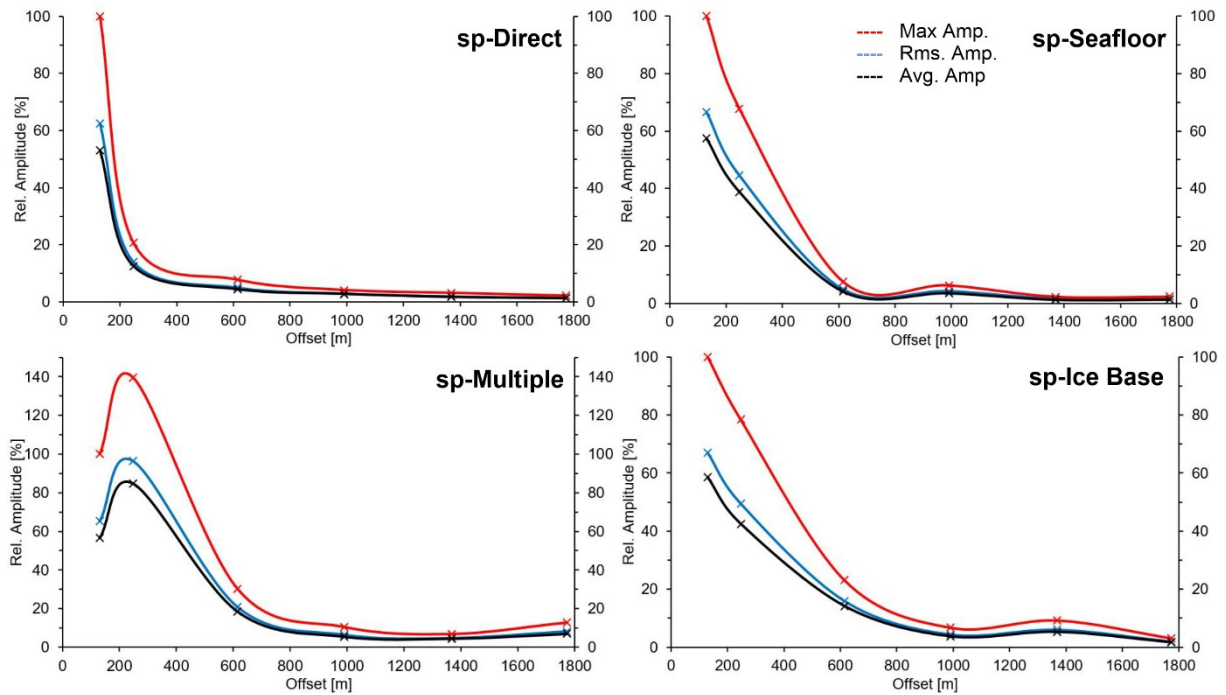


Figure 43: Illustration of percental shot group average amplitudes containing four shots each shot point. Maximum amplitude at the first offset is set to 100%. All values with respect to this value. Every panel shows three amplitudes for an individual event. Compare Figure 41 for annotations X-axis illustrates amplitudes without a unity. Y-axis indicates the shot point offset (marked by dots within the curves) to PALAOA [m].

To compare pp-event and sp-event amplitudes, Rms. – and Avg. – amplitudes of all 8 events are shown together (Figure 44). Furthermore the amplitude scale is changed into a logarithmic one. The amplitude of the pp-Direct wave event at the first offset is set to 100%. The Figures illustrate the percentual amount of the events with respect to the *pp-Direct* wave event. As in previous results basically an exponential decrease of the amplitudes can be recognized. All events show lower amplitudes than the *pp-Direct* wave except the *sp-Direct* (145 – 148 %) and the *sp-Multiple* (107 %) wave events at the first offset, and further the pp-Ice Base (195%) at the second offset (note that this value is disregarded in Figure 44 for better visualisation).

While analysing the logarithmic scaled illustration a roughly linear trend can be seen. With larger offsets the event amplitudes become more different and a general trend is not easily identifiable anymore. The relative amplitudes are listed in Table 8 and 9 below.

Table 8: Percental values of average amplitudes of all events. Amplitude of *pp-Direct* wave event at the first offset is set to 100%, all values normalised with respect to this value.

Event	Offset [m]					
	130	247	615	991	1369	1774
pp-Direct Wave	100.00	39.39	14.90	4.61	1.49	0.63
pp-Seaflor	93.51	23.31	5.83	1.73	1.49	1.36
pp-Multiple	106.96	22.67	15.69	4.06	1.54	0.93
pp-Ice Base	92.97	-	11.62	3.06	1.26	1.98
sp-Direct Wave	145.48	34.61	12.22	7.77	4.89	3.63
sp -Seaflor	76.76	51.87	5.48	4.75	1.72	1.79
Sp-Multiple	72.43	-	23.74	7.13	5.80	8.97
Sp-Ice Base	97.80	71.06	23.74	6.30	8.92	2.87

Table 9: Percental values of Root-Mean-Square (Rms) amplitudes of all events. Amplitude of *pp-Direct* wave event at the first offset is set to 100%, all values normalised with respect to this value.

Event	Offset [m]					
	130	247	615	991	1369	1774
pp-Direct Wave	100.00	39.90	14.69	4.61	1.46	0.69
pp-Seaflor	89.62	22.55	5.82	1.62	1.49	1.45
pp-Multiple	106.44	23.28	15.75	4.05	1.53	0.99
pp-Ice Base	93.86	-	11.68	3.12	1.27	2.10
sp-Direct Wave	147.89	33.49	12.03	7.19	4.80	3.49
sp -Seaflor	77.01	51.45	5.52	4.80	1.73	1.79
Sp-Multiple	72.27	-	23.06	7.16	5.32	9.11
Sp-Ice Base	96.90	71.59	23.07	6.33	8.74	2.86

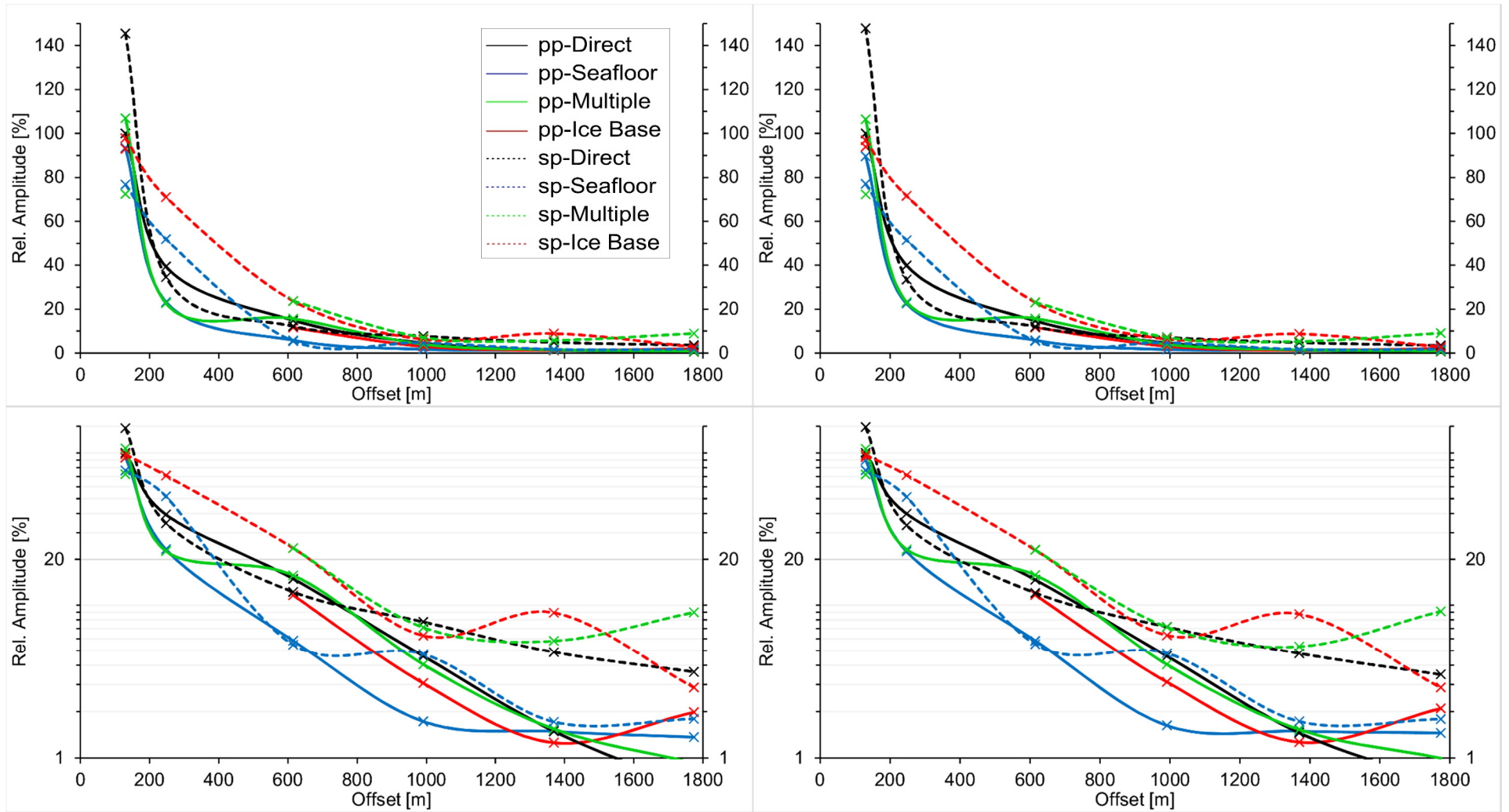


Figure 44: Combined illustration of the percental amplitudes of all 8 events. Values from Table 8 (left) and 9 (right). Amplitude of *pp-Direct* wave event is set to 100%, all amplitudes normalised with respect to this amplitude. Solid lines indicate pp-events, dashed lines show sp-events. Colours match event names in Figures 23, 25. Left graphs show average (Avg.) amplitudes, right graphs show Root-Mean-Square (Rms.) amplitudes. Relative amplitudes on the x-axis (upper graphs linear, lower graphs on a logarithmic scale); Y-axis shows the offset [m] of the shot points marked by coloured crosses on top of the lines.

5. Discussion and Interpretation

5.1. Geometry and velocities

As the base of the calculations and final results, the evaluation of the P- and S-wave velocities and further the geometry of the study area are discussed and compared with previous studies. Several studies dealt with Vibroseis measurements on Ekström Ice Shelf and the Halvfarryggen ice dome, a local grounded ice dome beneath the Ekström Ice Shelf (e.g. Eisen et al., 2010a; Hofstede et al., 2013; Diez, 2013; Eisen et al., 2015), and also in other glaciological study areas (e.g. Polom et al., 2014; Hofstede et al., 2018), before.

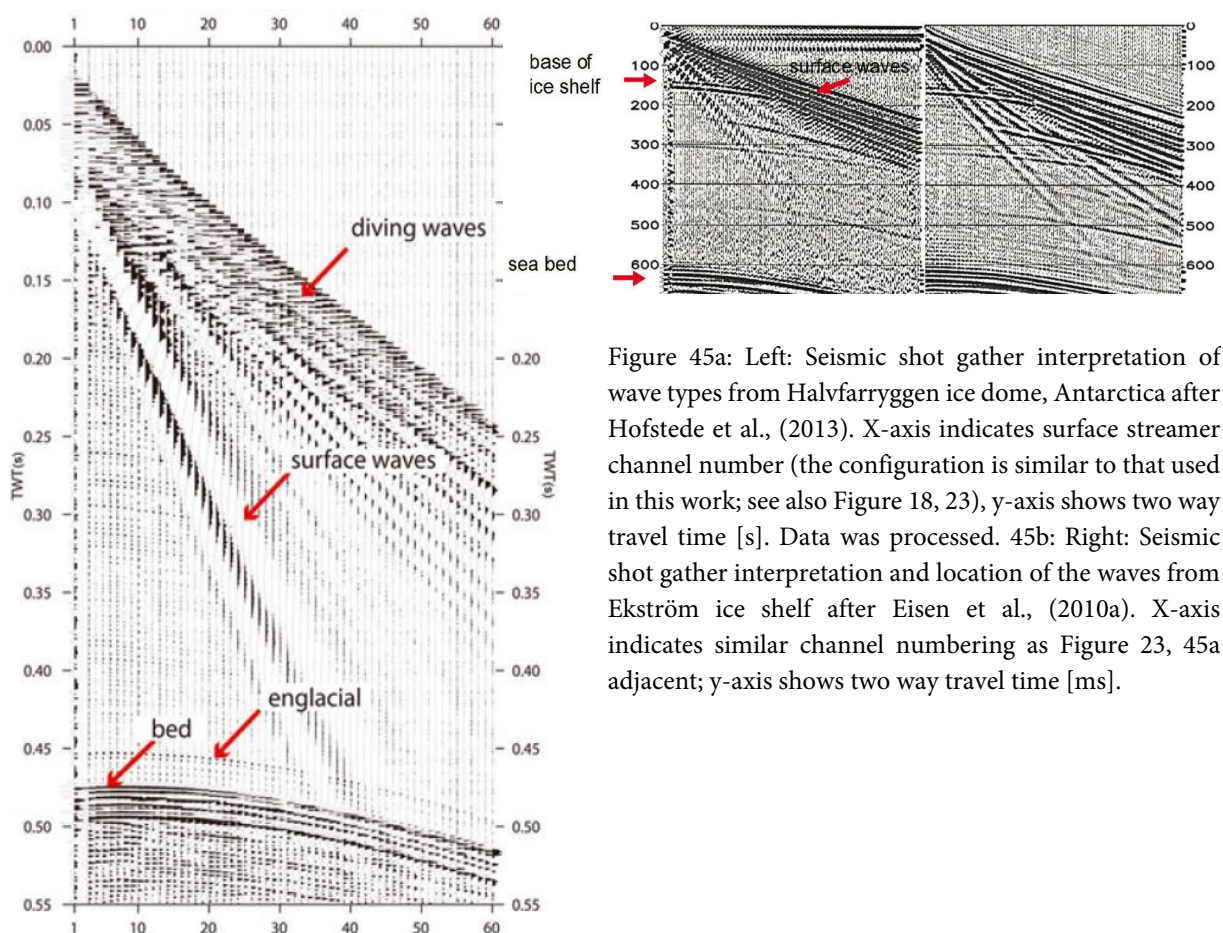


Figure 45a: Left: Seismic shot gather interpretation of wave types from Halvfarryggen ice dome, Antarctica after Hofstede et al., (2013). X-axis indicates surface streamer channel number (the configuration is similar to that used in this work; see also Figure 18, 23), y-axis shows two way travel time [s]. Data was processed. 45b: Right: Seismic shot gather interpretation and location of the waves from Ekström ice shelf after Eisen et al., (2010a). X-axis indicates similar channel numbering as Figure 23, 45a adjacent; y-axis shows two way travel time [ms].

Hofstede et al., (2013) interpreted the main signals in seismic shot gathers with a nearly linear and weak bended shape in the upper area as diving and surface waves referring to the wave type that matches the interpretation of the shot gathers in this thesis (Figure 45a). Eisen et al., (2010a) named this signals as surface waves referring to the location of the waves within the illustration (Figure 45b) but there is no contradiction because in comparison to basic seismology where the wave source (e.g. an earthquake) is located in great depths within the ground, in Vibroseis

surveys the source is at the surface so the direct P-wave, S-wave and diving waves can be considered to be close to the surface as well. The steeper a signal appears within a shot gather the lower the velocity of the wave becomes because it arrives at a same receiver (so distance) later. Surface waves (Love- and Rayleigh) have lower velocities than shear waves (Safani et al., 2005; Lowrie, 2007) but larger amplitudes. This proves that the shear wave has to appear between the steep and concise surface waves (Figure 45a, b; Figure 25) and the ground roll caused by diving P-waves.

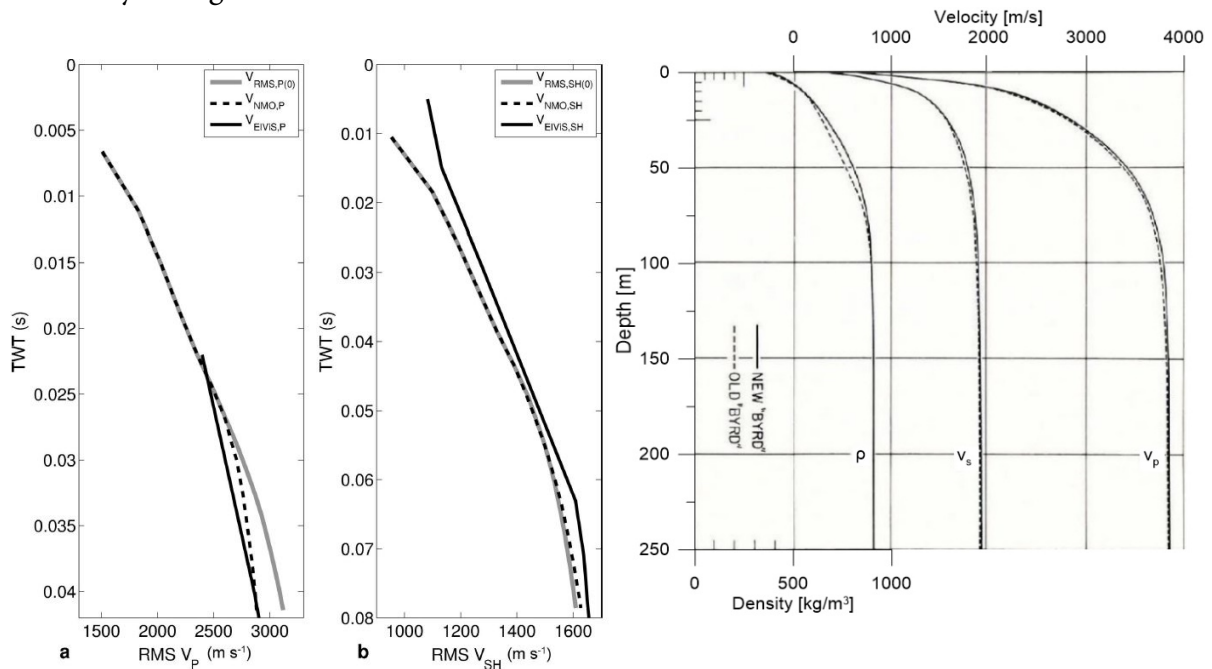


Figure 46a (left): Different RMS P- (a) and S-wave velocities (b) from Alpine glacier Colle Gnifetti by Diez et al., (2014). X-axis show velocity [m/s], y-axis show two-way travel time [s]. Both graphs indicate a depth of about 100m. 46b (right): P- and S-wave velocities from Byrd Station (Antarctica). Upper x-axis shows velocity [m/s], lower x-axis shows density [kg/m^3]; y-axis shows depth [m]. Modified after Kohnen and Bentley (1973).

P- and S-wave velocities are significantly affected by the firn densification (e.g. Kohnen and Bentley, 1973; King and Jarvis, 2007; Eisen et al., 2010a). After Kohnen and Bentley (1973) and Diez et al., (2014) the P-wave velocities in the upper 100 m, as it is the case on the ice shelf, ranges from about 1000 – 1500 m/s at the surface to 3000 m/s and higher within an depth of 100 m (see Figure 46a, b). The increasing velocities are caused by the firn densification that always takes place in glaciology if snow accumulates continuously. However the P-wave velocity beneath firn-ice transition can reach values of 3770 m/s and higher (e.g. Kohnen and Bentley, 1973; Polom et al., 2014). After Hofstede et al. (2013) a continuous velocity model of 3800 m/s can be used for seismic analysis. As the calculated P-wave velocities range between 3550 – 3753 m/s (Figure 46b) they match with values near firn-ice transition in previous studies and are thus much higher than typical P-wave velocities of snow.

S-wave velocities are derived from the shot gather information (chapter 3.3, 4.1) and show values between 1310 m/s and 1339 m/s. After Kohnen and Bentley (1973) and Diez et al. (2014) they increase with depth caused by the firn densification likewise as P-wave velocities. However, in the range differs from 500 – 1950 m/s after Kohnen and Bentley (1973) and from 1000 – 1600 m/s (Diez et al., 2014). The calculated S-wave velocities in this thesis match the velocity ranges of Kohnen and Bentley (1973) and Diez et al., (2014) and further the small range of 1310 – 1339 m/s indicates that the same signal is picked within the different shot gathers.

Because Hofstede et al. (2013) dealt with data from Halvfarryggen, Figure 45b cannot directly be taken into account for comparing the ice base reflection interpretation. Several studies suggest an ice shelf thickness of about 100 m (Kindermann et al., 2008; Eisen et al., 2010a; Eisen, 2018; Smith et al., 2019 (in press, 2020)). The available data enables the calculation of the ice shelf thickness in two ways: (1) By the two way travel time of the S-wave induced ice shelf reflection; (2) By the difference of the P-wave induced *Multiple* ice base reflection and the seafloor reflection. In contrast to previous studies an ice shelf thickness of 115 – 132 m is estimated within 12 calculations at 6 locations. This leads to uncertainties in the ray path and travel time calculation. An overestimated ice shelf thickness leads to longer ray paths within the ice column. Because the position of the PALAOA hydrophone is assumed to be fix with respect to the ice base (69m above seafloor, information from Eisen et al., 2010a) the relative distance between PALAOA and the seafloor differs. Furthermore there is an annual melt of 0.5 – 1.5 m/a and an ice flow of 140 m/a. This causes further uncertainties of the relative position of PALAOA with respect to the ice base and the seafloor. As the P-wave velocity in ice is high and of S-waves low, a longer travel path in ice by overestimating its thickness increase the time delay of pp-wave and sp-event arrivals in the seismograms. A detailed error analysis with increasing offset is applied in chapter 5.2.

5.2. Seismogram interpretation

As the error analysis of the time ranges of different events show there are uncertainties caused by wide ranges in velocities in the ice shelf that lead to difficulties in interpreting the seismograms. To get an improved view of PALAOA records, a seismic profile is taken into account (Figure 47).

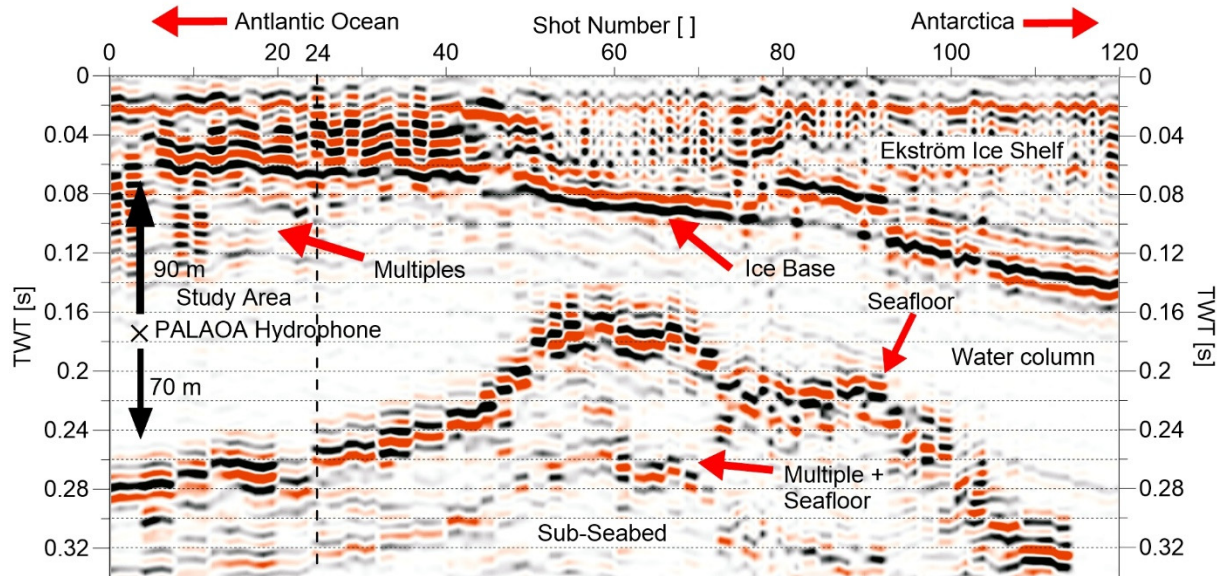


Figure 47: Seismic profile of the Ekström Ice Shelf, Antarctica, processed by E. Smith and C. Hofstede, modified. Data acquired with Vibroseis and 60 channel snow streamer. X-axis shows shot point numbering; y-axis show TWT [s]. The PALAOA hydrophone is located at the edge of the ice shelf on left side in the water column (Study area). Black dotted line indicates the offset of shot number 24 that indicates the largest offset this thesis deals with. Roughly distances: horizontal: 9km, vertical: 300m. Profile is strongly stretched in vertical direction.

The seismic profile shows high complexity. There is a strong reflection at about 0.06 s TWT in the study area that becomes clearer to the right and can be followed along the profile. With respect to the compressional wave velocity the reflection appears at a depth of about 110 m and thus can be interpreted as the ice base reflection. This facilitates the correct analysis and interpretation of the shot gathers with respect to the ice shelf thickness (see chapter 4.1, 5.1). A strong reflection at 0.26 – 0.28 s TWT that is not that sharp can be interpreted as the seafloor. With a given velocity of water of 1451 m/s the water column thickness results to 145 – 160 m that also fortifies initial assumptions. However, the study area depicts several reflections within the ice column and around the ice–water interface. Because surface waves may not be completely deleted, several artefacts disturb the results. Furthermore the formation of several multiples that may reach PALAOA occurs. Even though the ice base seems to be a sharp interface there is a plurality of events. The ice base experiences several processes as it is the contact area of the cryosphere and ocean. Processes of refreezing and melting mentioned in chapter 1.1 may cause a diffuse area that might induce further multiple reflections and refractions. Finally including the interpretation of a seismic profile with respect to the time delay ranges of different events the analysis of the seismograms becomes much more difficult.

5.3. Error analysis of event arrival times

An error analysis is executed in the following to bring different values of previous studies (Eisen et al., 2010b; Polom et al., 2014; Diez et al., 2014) into account to calculate a range in the arrival times of different events. The aim of the error analysis is to get an overview of the timing error of the event arrivals with increasing offsets. Previous analysis show that there are uncertainties regarding to the ice shelf thickness and velocities of the ice shelf.

The ice shelf thickness and P- and S-wave velocities of ice are the basis of ray path and travel time calculations of different events. Differences are caused by errors in calculations and interpretation of the shot gathers. The values differ from other values from previous studies on Ekström Ice Shelf. Particular variations have to be taken into account with respect to their mean values and standard deviation. At first a Gaussian error distribution is applied to get the vertical error of the travel time caused by different P- and S-wave velocities and ice thicknesses (Table 10-12). This gives the vertical error for rays traveling at normal incidence. Because the rays do not travel perfectly vertical but in an angular path, the error analysis of travel times for increasing offsets becomes very complex. To get a range of the time of arrival of all events with increasing offsets, the ray path and travel time calculations of chapter 3.3, 4.2 with the equations 3.3.2 – 3.3.9 are repeated with the minimum and maximum values of velocities and ice thicknesses. This gives a minimum and maximum time of arrival of each event (Figure 47). For the illustration, the values of Table 11 including literature values and calculated values of this work are used.

As mentioned before the P-wave velocity may reach values of 3770 – 3800 m/s at firn - ice transition (Kohnen and Bentley, 1973; Polom et al., 2014). After Holland and Anandakrishnan (2009) the S-wave velocity of firn vary between 500 and 1200 m/s. After Diez (2013) S-wave velocities of pure ice may vary between 1810 – 2180 m/s depending of its propagation angle and anisotropy. Depending on the anisotropy the S_V and S_H wave velocities range between 1800 – 1850 m/s. A value of 1830 m/s is taken into further account. Smith et al. (2019) suggest a compressional wave velocity of 1451 m/s in water. Rosier et al., (2018) determined P-wave velocities at Filchner-Ronne Ice Shelf between 1452-1454 m/s. This value seems to be very accurate thus its small error would not strongly impact further calculations and is not taken into account. To quantify the vertical error at normal incidence caused by parameter variations, the Gaussian error propagation is applied for travel times of compressional and shear waves in the ice shelf. The following Tables sum values used in the error propagation.

Table 10: Minimum and Maximum, mean value and standard deviation of P-, and S-wave velocity [m/s] and ice thickness [m] depending on results of this thesis (compare Table 3, 4):

Parameter	Minimum	Maximum	Mean	Std. Deviation
P-wave Velocity [m/s]	3550	3753	3613.16	66.75
S-wave Velocity [m/s]	1310	1339	1326.33	7.25
Ice shelf thickness [m]	115	132	123.43	4.2

Table 11: Minimum and Maximum, mean value and standard deviation of P-, and S-wave velocity [m/s] and ice thickness [m] depending values of Table 3 including reference values after Polom et al., (2014) ($v_p = 3770$ m/s), Diez (2013) ($v_s = 1830$ m/s) and Eisen et al., (2010b) (ice shelf thickness = 98m):

Parameter	Minimum	Maximum	Mean	Std. Deviation
P-wave Velocity [m/s]	3550	3770	3635.57	82.65
S-wave Velocity [m/s]	1310	1830	1401.14	183.02
Ice shelf thickness [m]	98	132	119.94	9.4

Table 12: Mean values and standard deviation from Table 11 and their precentral errors of P-, and S-wave velocity, and ice thickness and their resulting mean, standard deviation and precentral error of the travel time calculated with the Gaussian error distribution of velocities and ice thickness:

Parameter	v_p [m/s]	v_s [m/s]
Mean +Std. Dev.	3635.57 \pm 82.65	1401.14 \pm 183.02
Error	2.3 %	13.1 %
Ice thickness [m]	119.94 \pm 9.4	119.94 \pm 9.4
Error	7.8 %	7.8 %
Travel time: Mean, Std. Dev.	0.033 \pm 0.0033	0.084 \pm 0.017
Error	10.1 %	21 %

The calculations show errors in the travel time within the ice shelf of 10-21% depending on the wave type. To visualize the travel time range and bring it into account with the seismogram, the calculations of chapter 3.3 are repeated with the maximum and minimum values depending on the standard deviations. The results are illustrated in Figure 47 below.

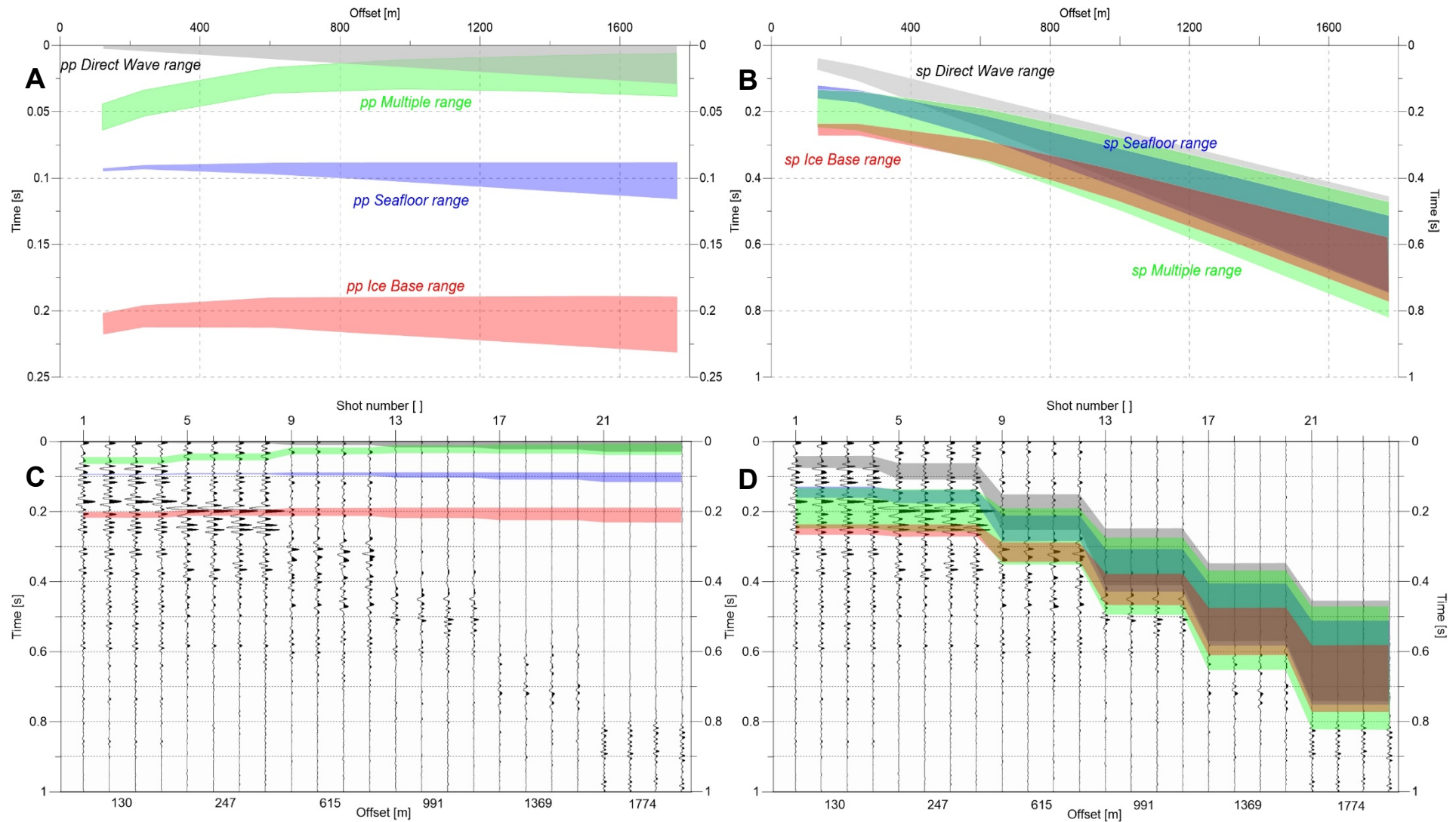


Figure 47: A) Range of pp-event time delays depending on different P-wave velocities of ice and the ice shelf thickness. B) Range of sp-event time delays depending on different S-wave velocities of ice and the ice shelf thickness. C) Travel time ranges of Figure A above inserted into the seismograms. D) Travel time ranges of Figure B above inserted into the seismogram. X axis in A and B show the shot point offset [m]. Upper x-axis in C and D show the shot number 1-24 and the lower x-axis show the shot point offset. Y-axis in all Figures show the travel time [s]. Note that the scaling of A is different for better illustration. Colours of events match with colours of event names in A, B.

Figure 47 above illustrates the error of the travel time of the pp- and sp-events which are analysed in this thesis. To explain the time delays and their errors, *Snell's Law* and the basic geometry has to be taken into account. The time delay between the *pp-Direct* wave and the *pp-Multiple* decreases with further offsets. Snell's Law depends on the media velocities at an interface of two media (see equation 2.2.4). Because compressional waves are about 2.5 times faster in ice than within water (3500 m/s in ice, 1451 m/s in water), their rays break to the lot-line (see also Figure 26-28) so the major part of the travel path continues within the ice. At offsets near to PALAOA the rays travel primarily vertically than in the lateral direction and thus the difference of the ray path of the *pp-Direct* wave (247 m) and *pp-Multiple* (467 m) is high (at 130 m offset) (see Figure 47). With larger offsets the ray paths become predominantly lateral (1774 m offset in contrast to 120 m ice thickness) so the differences of travel paths of these two events become smaller. At a distance of 1774 m the *pp-Multiple* has a travel path of 1866 m and the *pp-Direct* wave has a path of 1832 m so their differences decrease from 47 % to 3.2 % along a horizontal distance of 1654 m. In contrast the time delays of the *pp-Sea-floor* and *pp-Ice Base* do not change with larger offsets. As Figure 48 indicates, the ratio of travel path within the ice shelf of the events except *pp-Multiple* have a rather similar shape. However, the travel times range between 0.025 and 0.045 s at far offset. This can be explained with the variations of the P-wave velocity in the ice shelf that ranges between 3550 and 3753 m/s (in reference to 3770 m/s). There might be impacts by different ice shelf thicknesses but comparing the standard deviations of the P-wave velocity (66–82 m/s) and ice shelf thickness (4–9 m) the main cause of the time range might be the P-way velocity.

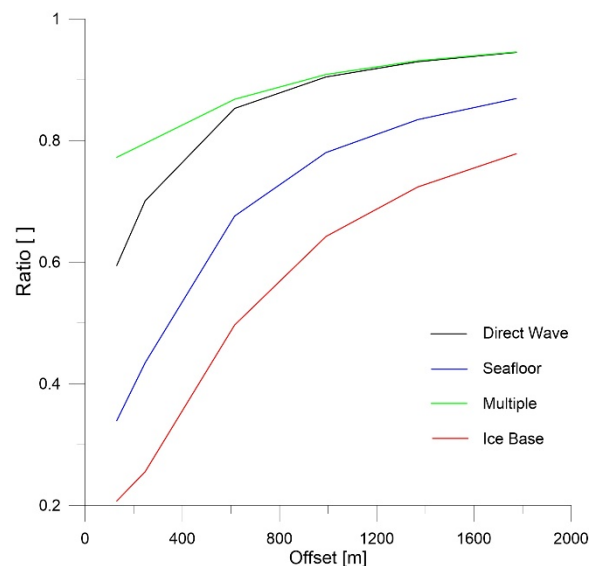


Figure 48: Precentral travel path ratio in ice for pp-events. X-axis shows the shot point offset to PALAOA; y-axis indicates ratio of travel path in ice in ratio to the total path (1 = 100%).

The results show travel time delays of sp-events increasing from 0.005 up to 0.800 ms with an increasing offset. It can be simply explained by one reasons. The shear wave velocity in ice is clearly less than of compressional waves (1330 m/s in contrast to 3500m/s). Even calculations at small offsets to PALAOA show a time delay of the *sp-Direct* wave. This leads to a continuous increase of the travel times with further shot point distances. As Figure 28 indicates the ray paths break in a different angle at the ice–water interface caused by the lower shear wave velocity in ice. This makes the rays travel more vertically within the ice shelf in contrast to P-waves that tend to propagate more horizontally and afterwards vertically in the water column. Therefore,

the precentral amount of the full ray path in ice is less for shear wave so the major part of the travel path appears in the water column. The uncertainties are clearly large in comparison to compressional waves (see Figure 47C, D). This is caused by the wide range of the shear wave velocity (1310 - 1830 m/s) and induces large uncertainties. Thus, with increasing offsets the events may overlap. However, even a wide time range caused by the errors does not make the shear wave events completely match with the main signal and thus indicate that there might be uncertainties that were not taken into account. Finally, the travel time delay increases with a decrease of shear wave velocity that means that even 1330 m/s is too fast to create matching of calculated travel times and seismograms.

5.4. Amplitude interpretation

As pointed out before, there are several uncertainties and errors that hinders the clear identification of individual events. Nevertheless, peaks could be detected along the offsets and the Maximum, RMS-, and average amplitude are calculated.

Disregarding sporadic variations (e.g. *pp-Ice Base* amplitude at shot point 2) all events indicate a strong decrease in their amplitudes with an increasing offset. Because the cross correlation generates a multiplication of amplitudes if the triggered and synthetic seismograms superimpose, the amplitude values are extremely high up to $7 - 10^7$. As these values do not represent the actual soundscape, relative values have to be used and thus the amplitude of the *pp-Direct* wave is set to 100%. This event was clear to identify especially at the first 4 groups of each 4 shots and thus a representative base for further analysis. Shots of larger offsets (= 1369 – 1774 m) are also relatively easy to line up because the time delay of the main signal increases linearly.

There are three processes that cause the continuous reduction in amplitudes of the *pp-Direct* wave event. 1: Spherical divergence, 2: The transmission coefficient at the ice - base interface and 3: attenuation within the ice column. Amplitudes decrease caused by the spherical divergence (see chapter 2.1, 2.2) with a ratio of $1/r$, depending on the ray path r and therefore with an increasing offset the spherical divergence increases. The transmission coefficient (TC) appears at interfaces of two different layers where refraction takes place. At near normal incidences the TC can be calculated in a simplified way (see chapter 2.2). After Holland and Anandakrishnan (2009) equations stay in their simplified validity if the incident angles range near normal incidence and thus between $0 - 10^\circ$. Due to geometrical conditions the lowest angle of incidence is accomplished by the *pp-Multiple* at the first offset. At a lateral distance of 130 m its incident angle becomes 18° and thus equation 2.2.6 is not valid so the more complex *Knott-Zoeppritz* equation has to be taken into account (Aki and Richards, 2002; Dobrin and Savit,

1988). For the solution of the equations, the *Zoeppritz-Magnitude-Plotter* by *Crewes* is used (Margrave and Lamoureux, 2019). The pp-wave reflection (R_{pp}) and pp-wave transmission (T_{pp}) coefficients RC and TC are illustrated in Figure 49. By means of this Figure the transmission coefficient of the *pp-Direct* wave refracting at the ice-water interface can be evaluated and taken into account.

The third factor of amplitude reduction is the attenuation. In glaciology the attenuation is driven by several processes in shapes that range from molecular to grain sizes (Peters et al., 2012). However, the temperature sensitivity plays an important role. As two of three factors are known, information about the attenuation results. The resulting values are listed in Table 13.

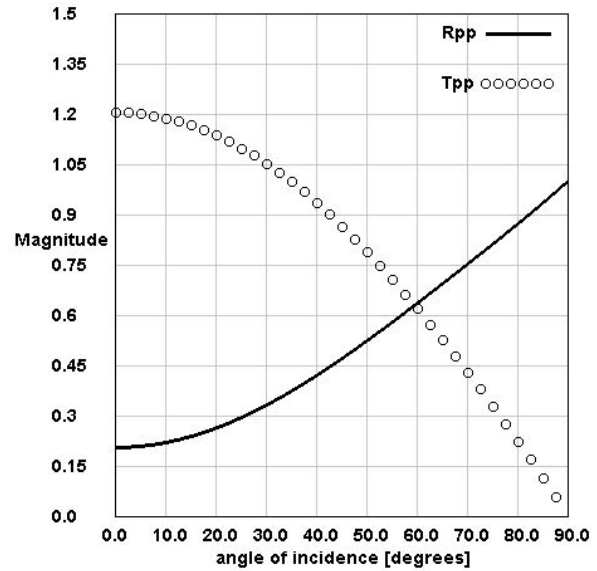


Figure 47: Transmission (T_{pp}) and reflection coefficient (R_{pp}) of P-waves at an ice-ocean interface depending on the angle of incidence. Basic values: $V_p(\text{ice}) = 3650 \text{ m/s}$; $V_s(\text{ice}) = 1400 \text{ m/s}$; $V_p(\text{water}) = 1451 \text{ m/s}$; $\text{density}(\text{ice}) = 918 \text{ kg/m}^3$; $\text{density}(\text{water}) = 1020 \text{ kg/m}^3$. Graph generated with *Crewes Zoeppritz-Magnitude-Plotter* (<https://www.crewes.org/ResearchLinks/ExplorerPrograms/ZoePlot/>; last request: 07.04.2020).

Table 13: Relative amplitude correction of the pp-Direct wave by application of the transmission coefficient at the ice-water interface and spherical divergence. Amplitude values in precentral reference to first offset amplitude. “Reduction” shows the percental decrease of the amplitude along the offsets.

Offset [m]	Full Ray Path [m]	Measured Amplitude	Angle of incidence [°]	Transmission coefficient []	Corrected Amplitude
130	247	1	41	0.9	271.4
247	336	0.4	60	0.62	182.5
615	681	0.15	78	0.25	177.7
991	1052	0.04	83	0.11	91.6
1369	1428	0.01	85	0.05	41.5
1774	1832	0.01	86	0.04	22.7
Reduction		~100%			99.9%

With respect to spherical divergence and transmission coefficient corrections the relative amplitudes still show an extremely strong decrease of 99.91%. Smith (1997) presented values of attenuation that range between $0.005 - 0.05 \cdot 10^{-3}$ 1/m that matches previous values of Kohnen and Bentley (1976). There is a strong sensitivity to the temperature (e.g. Holland and Anandakrishnan; 2009 Gusmeroli et al., 2010; Peters et al., 2010) especially near the melting point (Peters et al., 2010) and further to physical conditions as the pressure and crystal anisotropy (e.g. Toksöz et al., 1979; Peters et al., 2012). Both temperature (near melting point) und crystal anisotropy are partly present and variable within an ice shelf and thus make further estimations to amplitude variations more difficult. After all the strong offset dependent decrease of the amplitude of more than 99% has to be considered with care.

However, information of Eisen et al., (2010b) is taken into account to provide an estimation about soundscape of amplitude values. The following Table is based on information of Eisen et al., (2010b) and lists three kinds of maximum (real state) amplitudes: 1.: Peak = Zero-peak amplitude of the whole event. 2.: RMS (=Root-Mean-Square) amplitude in a time window taken over the whole 10s Vibroseis sweep. 3.: SEL = Sound exposure level = time integrated RMS values. All amplitudes measured in decibel (= dB).

Table 14: Recorded Peak, RMS and SEL sound levels with PALAOA hydrophone from Eisen et al. (2010b). All values in decibel re 1V/ μ Pa.

Shot	Shot Nr []	Offset [m]	Peak [dB]	RMS [dB]	SEL [dB]
PTR001a	1	130	141.0	132.1	152.1
PTR002a	5	247	139.9	130.6	150.6
PTR003a	9	615	125.4	114.3	134.3
PTR004a	13	991	116.3	107.7	127.7
PTR005a	17	1369	117.2	104.7	124.7

It can be assumed that the maximum sound levels match the strongest peaks within the seismograms of the cross correlated data (see Figure 29, 31). Eisen et al., (2010b) give amplitude values for five shots listed in Table 14. The cross correlated amplitude values are taken into account and set into reference to the sound values of Eisen et al., (2010b) so it is assumed that the amplitudes of the strongest peaks in a seismogram (in Table 15 “CC Max Amp”) match the maximum sound level after Eisen et al. (2010b) (in Table 15 “Zero-Peak”). The ratio of pp-Direct wave amplitude (in Table 15 “CC Amp pp-Direct”) (first arriving signal in the seismogram) and the strongest peak (“CC Max Amp”) within a single shot gives estimations of the sound level of the pp-Direct wave (dB) (in Table 15 “Real Amp pp-Direct”). Note that the sixth shot point is not taken into account as there are no sound level values given by Eisen et al.,

(2010b) and that a single amplitude of a single shot is used and not the average value of four shots each shot point location. The average value of the maximum peak is taken into account. The results are listed in Table 15.

Table 15: Zero-Peak Amplitude [dB] of Eisen et al (2010b), cross correlated maximum amplitude of the strongest peak of the seismogram (CC Max Amp), average cross-correlated pp-Direct wave amplitude of the seismogram and decibel related amplitude of pp-Direct wave [dB] (CC = cross-correlated)

Shot []	Offset [m]	Zero-Peak [dB]	CC Max Amp [$\cdot 10^6$]	CC Amp pp-Direct [$\cdot 10^6$]	Real Amp pp-Direct [dB]
PTR001a	130	141.0	68.14	31.32	64.80
PTR002a	247	139.9	63.81	11.32	24.81
PTR003a	615	125.4	14.61	4.64	39.82
PTR004a	991	116.3	7.21	0.6	9.67
PTR005a	1369	117.2	5.49	0.085	1.81
Reduction [%]		16.8	91.9	99.73	97.2

The results show, that the amplitudes of the maximum Zero-Peak do not match with maximum cross correlated amplitude of the seismogram. Whereas the amplitude Zero-Peak amplitude decrease by 16.8 % along the first 5 shot point locations, the related cross correlated maximum amplitude (note that the maximum amplitude is represented as the average value of the entire peak) decreases by 91.9 %. In relation to this amplitudes the percental decrease of the *pp-Direct* wave event shows an amplitude reduction of 97.2 dB along an offset of 1239 m. As the real sound levels of the *pp-Direct* wave shows similar trends as the cross correlated maximum values that is relative to real underwater sound values, it can be assumed that the values for different events act similar with respect to related values. Figure 40 indicates that amplitudes of different events decay exponentially. Including the spherical divergence and transmission coefficient shows slight changes in values (Table 13). Bringing this corrections in connection to further events is beyond the scope and capabilities of a Master-Thesis. As the large amplitude developments between real underwater soundscape and analysed amplitudes are caused during the cross correlation, further analysis in this regard has to be taken into account.

5.5. Critical discussion

The presentation of the results and discussion finally shows, that there are many uncertainties were revealed during the process of this work. The main problem in analysing this data is the superposition of several events within the seismograms. Analysis of shots at near normal

incidence may simplify calculations and further improve abilities in estimations of the attenuation of seismic waves in ice. The thesis finally aims to present the new way of analysing seismic data and to quantify and declare the problems and uncertainties. To focus and become more into detail, further studies have to be done. An outlook in chapter 6 deals with the evaluation of the approach and suggestions for further studies using the PALAOA hydrophone at Ekström Ice Shelf, Antarctica.

Disregarding the uncertainties that complicate analysis of results, there are several conditions that may affect the hydrophone data and should be taken into account. Wei and Phillips (2010) presented different sources that create harmonics during the signal production of Vibroseis shots. These harmonics are also visible in the recordings of PALAOA. Harmonics are seismic waves with total multiple frequencies that occur at the same time. This causes a superimposition of several waves with multiple frequencies that leads to an increase of the cross correlated amplitude.

Furthermore there may be an uncertainty in the data caused by the electrical condition of the hydrophone as itself. After Eisen et al., (2010b), the second (central) hydrophone that was assumed to be the used one for the recordings does not have a pre-amplifier. This causes a problem as the hydrophone may record signals induced by waves that reach and compress the cable of the hydrophone within the ice column that creates noise and so leads to an overestimation of amplitudes. The other active hydrophone in the water is not affected by this problem. At the end of the study another problem was noticed that has to be pointed out and is explained in the following.

The problem of hydrophone choice

One struggle at the beginning of the thesis was to carry out the location and thus the right hydrophone that was used for the data measurements. Originally four hydrophones were stationed at different locations beneath the Ekström Ice Shelf in Antarctica within the water column. Three of the four hydrophones built a shape of a triangle and a fourth hydrophone was stationed in the centre (Figure 5). After Kindermann et al., (2008) two of them were defect so finally the central hydrophone (2) and one in the north eastern direction were still operational. After Eisen et al., (2010a) the central hydrophone and one in north western direction are active so there is a first contrast in the references. Following Figure 21 that is modified after Eisen et al., (2010a) the hydrophone that was used for data acquisition is stationed within the line of shot records. This is proven by the Eisen et al., (2010b) with a map of the locations of the two hydrophones and the first five shot points. The given coordinates of hydrophone (2) that is named PALAOA CTR (=PALAOA central) match with the map of Eisen et al., (2010a) (Figure 21). Two maps and given information by the titles of Figures in Eisen et al., (2010b) prove that

hydrophone (2) as the central hydrophone is stationed within a line of the shot records. It is fortified by the offsets of the observer logs. As the distance between the shot points conduct 375 m it was assumed that the hydrophone within the line of shot records was used because the offsets to the north western hydrophone would not increase in a distance of 375 m due to its lateral displacement to the shot record line but that is additional given in the titles of Figures by Eisen et al., (2010b). Depending on this information the central hydrophone (2) was assumed to be the right one for analysis.

After reviewing different references several arguments pointed out that prove that hydrophone 1 could also be the used one for data acquisition. Several papers that become available during or at the end of the thesis specify a single coordinate for PALAOA that matches with the coordinates of hydrophone 1 (Boebel et al., 2006; Kindermann et al., 2008; Boebel et al., 2017; Eisen, 2018). This coordinates match with shot record coordinates by Eisen et al. (2010a). After reviewing this it became obvious that the coordinates in the map of Eisen et al., (2010a) do not match with other references. So finally it has to be admitted that several basic information differ in their arguments especially while spectating coordinates named in the literature and given maps and thus they provide arguments that both hydrophones could be the one that was used for data acquisition.

This is very important because the geometrical and spatial conditions and finally the technical properties of the hydrophones itself are different. The locations differ and thus the offsets to the shot points that are the base of the ray path calculations. Furthermore do the hydrophones stay in different depths as hydrophone 1 is located 70 m below the ice base and thus about 90 m above the seafloor whereas hydrophone 2 is placed 20 m deeper. Thereby not only the lateral offset differ but also the relative travel paths between separate events because for example the ray path of the direct wave decreases (while spectating the changing of spatial conditions of hydrophone 2 to hydrophone 1) because hydrophone 1 is stationed 20 m above hydrophone 2 but for the same shot point the ray path of the seafloor event increases because the wave travels after reflecting at the seafloor 90 m upwards instead of 70 m as assumed. This fact is realized at the end of the thesis and thus there is no time to take this into account but it has to be mentioned for further works.

6. Conclusion

This thesis provides a new approach in analysing seismic source data in glaciology. The PALAOA hydrophone that is stationed beneath the Ekström Ice Shelf, Antarctica, indicates the ability in recording seismic signals by its sound pressure level.

Altogether the ray path and travel time of eight events triggered at six offsets are calculated. The first arriving signal is identified and interpreted as the direct compressional wave. The seismograms indicate a continuous delay of the main signal that can be explained with sp-converted waves with high amplitudes. However, pp-events show relative constant time delays with respect to the first arriving signal. The main peaks in the seismograms do not match with calculated travel times which indicate large uncertainties caused by varying wave velocities and geometrical conditions. The genesis of multiples superimpose the signal and complicate the detection of analysis that in fact is the largest source of error. However, the amplitudes of all events at calculated arrivals show a strong decrease with further offsets. The maximum amplitude of the whole signal shows a similar reduction along the offsets. Corrections of the spherical divergence and the transmission coefficient show less changes.

Finally, this work is the first approach in analysing seismic data that was recorded by a hydrophone beneath an ice shelf. Different challenges during the evaluation complicated the analysis. However, the hydrophone is estimated as a good application for further studies to decrease basic uncertainties concerning seismic campaigns in glaciology.

7. Outlook

This thesis shows that there are still large uncertainties that complicate a quantification of wave attenuation in the ice that further gives final predictions of the source amplitude. Both values are poorly known in seismic campaigns in glaciology and lead to large uncertainties in detecting and analysing subglacial material. Two main and basic problems induced first uncertainties in data analysing: The shot point offset and the timing of the data. As mentioned in chapter 5.4 there is no shot that triggers waves with near normal incidence angles. Several processes that produce uncertainties in the amplitude and travel path as the angle to c-axis orientation, reflection coefficient and bending ray path caused by firn densification can be minimized if shots were triggered directly above PALAOA. Because there is no coupling between PALAOA and the Vibroseis, the first arrival has to be identified manually. This becomes more difficult with increasing offsets. Analysing individual shots triggered by both hydrophones additionally may improve the interpretation as one shot would be recorded by two receivers at two offsets.

This thesis provides a first approach in using hydrophones as seismic receivers that can be used in campaigns on ice shelves. Finally, the hydrophone can be predicated as a characterful method to analyse seismic data and provide meaningful results to decrease basic uncertainties that seismic observations in glaciology deal with.

8. Bibliography

- Aki, K., & Richards, P. G. (2002). *Quantitative seismology* (2nd ed.). University Science Books, U.S.
- Arnaud, L., Barnola, J. M., & Duval, P. (2000). Physical modeling of the densification of snow/firn and ice in the upper part of polar ice sheets. *Physics of Ice Core Records*, 285–305.
<https://eprints.lib.hokudai.ac.jp/dspace/handle/2115/32472%0Ahttp://www.google.com/search?client=safari&rls=en-us&q=Physical+modeling+of+the+densification+of+snow+firn+and+ice+in+the+upper+part+of+polar+ice+sheets&ie=UTF-8&oe=UTF-8%5Cnpapers2://publication>
- Baeten, G. J. M. (1989). *Theoretical and practical aspects of the Vibroseis method*. Technische Universiteit Delft.
- Benn, D. I., & Evans, D. J. A. (2010). *Glaciers and Glaciation* (2nd ed., Issue 2). Routledge.
- Blunier, T., & Schwander, J. (2000). Gas enclosure in ice: age difference and fractionation. *Physics of Ice Core Records*, 307–326.
- Boebel, O. (2017). The Expedition PS103 of the Research Vessel POLARSTERN to the Weddell Sea in 2016/2017. In *Berichte zur Polar-und Meeresforschung*. http://epic.awi.de/45596/1/BzPM_0710_2017.pdf
- Boebel, O., Kindermann, L., Klinck, H., Bornemann, H., Plötz, J., Steinhage, D., Riedel, S., & Burkhardt, E. (2006). Real-Time Underwater Sounds From the Southern Ocean. *EOS, Transactions, American Geophysical Union*, 87(36), 361–365.
- Booth, A. D., Mercer, A., Clark, R., Murray, T., Jansson, P., & Axtell, C. (2013). A comparison of seismic and radar methods to establish the thickness and density of glacier snow cover. *Annals of Glaciology*, 54(64), 73–82. <https://doi.org/10.3189/2013AoG64A044>
- Braile, L. (2016). *A Short Course in Seismic Reflection Profiling*.
- Brittle, K. F., Lines, L. R., & Dey, A. K. (2001). Vibroseis deconvolution: A comparison of cross-correlation and frequency-domain sweep deconvolution. *Geophysical Prospecting*, 49(6), 675–686. <https://doi.org/10.1046/j.1365-2478.2001.00291.x>
- Brodzikowski, K., & van Loon, A. J. (1990). Glacigenic Sediments. In *Developments in Sedimentology* (Vol. 49). Elsevier. [https://doi.org/10.1016/S0070-4571\(08\)70975-0](https://doi.org/10.1016/S0070-4571(08)70975-0)
- Cuffey, K. M., & Paterson, W. S. B. (2010). *The Physics of Glaciers* (4th ed.). Academic Press.
- Diez, A. (2013). *Effects of cold glacier ice crystal anisotropy on seismic data*. Karlsruher Institut für Technologie.
- Diez, A., Eisen, O., Weikusat, I., Eichler, J., Hofstede, C., Bohleber, P., Bohlen, T., & Polom, U. (2014). Influence of ice crystal anisotropy on seismic velocity analysis. *Annals of*

- Glaciology*, 55(67), 97–106. <https://doi.org/10.3189/2014AoG67A002>
- Dobrin, M. B., & Savit, C. H. (1988). Introduction to geophysical prospecting. 4th edition. In *McGraw-Hill, New York*.
- Eisen, O., Hofstede, C., & Drews, R. (2010a, unpublished). *Limpics - Final Expedition Report*.
- Eisen, Olaf, Hofstede, C., & Kindermann, L. (2010b, unpublished). *Bericht über die durchgeführten Tätigkeiten gemäß der Genehmigung zur Durchführung des Antrags vom 19.06.2009 - "Seismische Messungen im Einzugsgebiet des Ekströmisen"* unpublished.
- Eisen, Olaf, Hofstede, C., Diez, A., Kristoffersen, Y., Lambrecht, A., Mayer, C., Blenkner, R., & Hilmarsson, S. (2015). On-ice vibroseis and snowstreamer systems for geoscientific research. *Polar Science*, 9(1), 51–65. <https://doi.org/10.1016/j.polar.2014.10.003>
- Eisen, Olaf. (2018). *UBA - Nachbericht - Bericht über die durchgeführten Tätigkeiten gemäß der Genehmigung zur Durchführung des Antrags: "Seismic pre-site survey of seafloor geologic stratigraphy for preparation of the sub-EIS-Obs project."* <https://doi.org/10.1017/CBO9781107415324.004>
- Gusmeroli, A., Clark, R. A., Murray, T., Booth, A. D., Kulesa, B., & Barrett, B. E. (2010). Seismic wave attenuation in the uppermost glacier ice of Storglaciaeren, Sweden. *Journal of Glaciology*, 56(196), 249–256.
- Haldar, S. K. (2013). Exploration Geophysics. In *Mineral Exploration* (pp. 73–93). <https://doi.org/10.1016/b978-0-12-814022-2.00006-x>
- Herron, M. M., & Langway, C. C. (1980). Firn Densification: An Empirical Model. *Journal of Glaciology*, 25(93), 373–385. <https://doi.org/10.3189/s0022143000015239>
- Hofstede, C., Christoffersen, P., Hubbard, B., Doyle, S. H., Young, T. J., Diez, A., Eisen, O., & Hubbard, A. (2018). Physical Conditions of Fast Glacier Flow: 2. Variable Extent of Anisotropic Ice and Soft Basal Sediment From Seismic Reflection Data Acquired on Store Glacier, West Greenland. *Journal of Geophysical Research: Earth Surface*, 123(2), 349–362. <https://doi.org/10.1002/2017JF004297>
- Hofstede, Coen, Eisen, O., Diez, A., Jansen, D., Kristoffersen, Y., Lambrecht, A., & Mayer, C. (2013). Investigating englacial reflections with vibro-and explosive-seismic surveys at Halvfarryggen ice dome, Antarctica. *Annals of Glaciology*, 54(64), 189–200. <https://doi.org/10.3189/2013AoG64A064>
- Hogg, A. E., & Gudmundsson, G. H. (2017). Commentary: Impacts of the Larsen-C Ice Shelf calving event. *Nature Climate Change*, 7(8), 540–542. <https://doi.org/10.1038/nclimate3359>
- Holland, C. W., & Anandkrishnan, S. (2009). Subglacial seismic reflection strategies when source amplitude and medium attenuation are poorly known. *Journal of Glaciology*, 55(193), 931–937. <https://doi.org/10.3189/002214309790152528>
- Huang, Z., Peng, X., & Li, G. (2018). Optimization of the dynamic stiffness of the seismic

- vibrator. *Advances in Mechanical Engineering*, 10(11), 1–11. <https://doi.org/10.1177/1687814018809809>
- Jakobs, C. L., Reijmer, C. H., Kuipers Munneke, P., König-Langlo, G., & van Den Broeke, M. R. (2019). Quantifying the snowmelt-albedo feedback at Neumayer Station, East Antarctica. *The Cryosphere*, 13(5), 1473–1485. <https://doi.org/10.5194/tc-13-1473-2019>
- Jiskoot, H. (2011). Dynamics of Glaciers. In *Encyclopedia of Snow, Ice and Glaciers* (pp. 245–255). Springer. <https://doi.org/10.1007/978-90-481-2642-2>
- Kindermann, L., Boebel, O., Bornemann, H., Burkhardt, E., Klinck, H., Opzeeland, I. C., Plötz, J., & Seibert, A.-M. (2008). A perennial acoustic observatory in the Antarctic Ocean. *Computational Bioacoustics for Assessing Biodiversity: Proceedings of the International Expert Meeting on IT-Based Detection of Bioacoustical Patterns, December 7th until December 10th, 2007 at the International Academy for Nature Conservation (INA) Isle*.
- Kishtawal, C. M. (2003). Retrieval of agrometeorological parameters from satellites. In *Satellite Remote Sensing and GIS Applications in Agricultural Meteorology* (pp. 195–211).
- Kohnen, H., & Bentley, C. R. (1973). Seismic Refraction and Reflection Measurements at “Byrd” Station, Antarctica. *Journal of Glaciology*, 12(64), 101–111. <https://doi.org/10.3189/s0022143000022747>
- Kristoffersen, Y., Hofstede, C., Diez, A., Blenkner, R., Lambrecht, A., Mayer, C., & Eisen, O. (2014). Reassembling Gondwana: A new high quality constraint from vibroseis exploration of the sub-ice shelf geology of the East Antarctic continental margin. *Journal of Geophysical Research: Solid Earth*, 119(12), 9171–9182. <https://doi.org/10.1002/2014JB011479>.Received
- Kuhn, M. (1995). The mass balance of very small glaciers. *Zeitschrift Für Gletscherkunde Und Glazialgeologie*, 31(1), 171–179.
- Lindseth, R. O. (1968). 7. Vibroseis. In *Digital Processing of Geophysical Data - A Review* (pp. 7.1-7.14). <https://doi.org/10.1190/1.9781560802310.ch7>
- Lowrie, W. (2007). *Fundamentals of Geophysics* (2nd ed.). Cambridge University Press.
- Lüthi, M. P., Walter, F., Guillaume, J., Werder, M., & Funk, M. (2017). *Physics of Glaciers I*.
- Margrave, G. F., & Lamoureux, Michael, P. (2019). *Numerical Methods of Exploration Seismology: With Algorithms in MATLAB (NMES)*. Cambridge University Press. <https://www.crewes.org/ResearchLinks/FreeSoftware/>
- Marshall, J., & Speer, K. (2012). Closure of the meridional overturning circulation through Southern Ocean upwelling. *Nature Geoscience*, 5(3), 171–180. <https://doi.org/10.1038/ngeo1391>
- Masson-Delmotte, V.; Zhai, P.; Pörtner, H. O.; Roberts, D.; Skea, J.; Shukla, P. R. ., Pirani, A.; Moufouma-Okia, W.; Péan, C.; Pidcock, R.; Connors, S.; Matthews, J. B. R.; Chen, Y.; Zhou, X.; Gomis, M.I.; Lonnoy, E.; Maycock, T. ., & Tignor, M.; Waterfield, T. (eds. .

- (2018). Summary for Policymakers. In: Global Warming of 1.5°C. An IPCC Special Report on the impacts of global warming of 1.5°C above pre-industrial levels and related global greenhouse gas emission pathways, in the context of strengthening the global response. *Journal of Chemical Information and Modeling*, 53(9), 3–25. <https://doi.org/10.1017/CBO9781107415324.004>
- Neckel, N., Drews, R., Rack, W., & Steinhage, D. (2012). Basal melting at the Ekström ice shelf, Antarctica, estimated from mass flux divergence. *Annals of Glaciology*, 53(60), 294–302. <https://doi.org/10.3189/2012AoG60A167>
- Onajite, E. (2013). Understanding Seismic Exploration. In *Seismic Data Analysis Techniques in Hydrocarbon Exploration* (1st ed., pp. 33–62). Elsevier. <https://doi.org/10.1016/b978-0-12-420023-4.00003-4>
- Padman, L., Siegfried, M. R., & Fricker, H. A. (2018). Ocean Tide Influences on the Antarctic and Greenland Ice Sheets. *Reviews of Geophysics*, 56(1), 142–184. <https://doi.org/10.1002/2016RG000546>
- Peters, L. E., Anandakrishnan, S., Alley, R. B., & Voigt, D. E. (2012). Seismic attenuation in glacial ice: A proxy for englacial temperature. *Journal of Geophysical Research: Earth Surface*, 117(2), 1–10. <https://doi.org/10.1029/2011JF002201>
- Polom, U., Hofstede, C., Diez, A., & Eisen, O. (2014). First glacier-vibro-seismic experiment - Results from cold firn of Colle Gnifetti. *Near Surface Geophysics*, 12(4), 493–504. <https://doi.org/10.3997/1873-0604.2013059>
- Pörtner, H. O.; Roberts, D. C.; Masson-Delmotte, V.; Zhai, P.; Tignor, M.; Poloczanska, E.; Mintenbeck, K.; Alegria, A.; Nicolai, M.; Okem, A.; Petzold, J.; Rama, B.; Weyer, N. M. . (eds). (2019). Summary for policymakers. *IPCC Special Report on the Ocean and Cryosphere in a Changing Climate*, vii, 973, 7–22. https://doi.org/http://www.ipcc.ch/publications_and_data/ar4/wg2/en/spm.html
- Rignot, E., Casassa, G., Gogineni, P., Krabill, W., Rivera, A., & Thomas, R. (2004). Accelerated ice discharge from the Antarctic Peninsula following the collapse of Larsen B ice shelf. *Geophysical Research Letters*, 31(18), 2–5. <https://doi.org/10.1029/2004GL020697>
- Rignot, E., Mouginot, J., & Scheuchl, B. (2011). Ice flow of the Antarctic ice sheet. *Science*, 333(6048), 1427–1430. <https://doi.org/10.1126/science.1208336>
- Rosier, S. H. R., Hofstede, C., Brisbourne, A. M., Hattermann, T., Nicholls, K. W., Davis, P. E. D., Anker, P. G. D., Hillenbrand, C. D., Smith, A. M., & Corr, H. F. J. (2018). A New Bathymetry for the Southeastern Filchner-Ronne Ice Shelf: Implications for Modern Oceanographic Processes and Glacial History. *Journal of Geophysical Research: Oceans*, 123(7), 4610–4623. <https://doi.org/10.1029/2018JC013982>
- Safani, J., O'Neill, A., Matsuoka, T., & Sanada, Y. (2005). Applications of love wave dispersion for improved shear-wave velocity imaging. *Journal of Environmental and Engineering Geophysics*, 10(2), 135–150. <https://doi.org/10.2113/JEEG10.2.135>

- Sandhager, H., & Blindow, N. (2000). Surface elevation, ice thickness, and subglacial-bedrock topography of Ekstrom Ice Shelf (Antarctica) and its catchment area. *Annals of Glaciology*, 30, 61–68. <https://doi.org/10.3189/172756400781820723>
- Sheriff, R. E., & Geldart, L. P. (1995). *Exploration seismology* (2nd ed.). Cambridge University Press.
- Smith, A. M. (1997). Basal conditions on Rutford Ice Stream, West Antarctica, from seismic observations. *Journal of Geophysical Research*, 102, 543–552.
- Smith, A. M., Murray, T., Nicholls, K. W., Makinson, K., Adalgeirsdóttir, G., Behar, A. E., & Vaughan, D. G. (2007). Rapid erosion, drumlin formation, and changing hydrology beneath an Antarctic ice stream. *Geology*, 35(2), 127–130. <https://doi.org/10.1130/G23036A.1>
- Smith, Andy M., & Murray, T. (2009). Bedform topography and basal conditions beneath a fast-flowing West Antarctic ice stream. *Quaternary Science Reviews*, 28(7–8), 584–596. <https://doi.org/10.1016/j.quascirev.2008.05.010>
- Smith, E. C., Kuhn, G., Hattermann, T., Kuhn, G., Gaedike, C., Berger, S., Drews, R., Ehlers, T. A., Franke, D., Gromig, R., Hofstede, C., Lambrecht, A., Läufer, A., Mayer, C., Tiedeman, R., Wilhelms, F., & Eisen, O. (2019, in press). Detailed seismic bathymetry beneath Ekstroem Ice Shelf , Antarctica : Implications for glacial history and ice-ocean interaction Detailed seismic bathymetry beneath Ekstr ¨ om Ice Shelf , Antarctica : Implications for glacial history and ice-ocean interac. *Geophysical Research Letters, Preprint, November*. <https://doi.org/10.1002/essoar.10501125.1>
- Steeple, D. W. (2005). Shallow Seismic Methods. In Y. Rubin & S. S. Hubbard (Eds.), *Hydrogeophysics* (pp. 215–251). Springer. https://doi.org/10.1007/1-4020-3102-5_8
- Telford, W. M., Geldart, L. P., & Sheriff, R. E. (1991). Applied Geophysics - Solid Earth Geophysics. In *Cambridge University press* (2nd ed.). <https://doi.org/10.5860/choice.48-1788>
- Toksöz, M. N., Johnston, D. H., & Timur, A. (1979). Attenuation of seismic waves in dry and saturated rocks : I . Laboratory measurements. *Geophysics*, 44(4), 681–690.
- Wei, Z., & Phillips, T. F. (2010). Harmonic distortion reduction on seismic vibrators. *Leading Edge (Tulsa, OK)*, 29(3), 256–261. <https://doi.org/10.1190/1.3353719>
- Yilmaz, Ö. (2001). *Seismic Data Analysis: Vol. I* (2nd ed., Issue 10). Society of Exploration Geophysicists.

9. Appendix A

Resulting ray path and travel times, Offset = 130m

pp-wave events					sp-wave events				
Direct Wave	Seafloor	Multiple	Ice_base		Direct Wave	Seafloor	Multiple	Ice_base	
Teta1	41.331	33.192	18.110	26.236	Teta1	31.304	19.650	15.950	13.531
Teta2	15.660	12.930	7.299	10.410	Teta2	34.560	21.540	17.459	14.800
Offset	130.002	130.089	130.073	130.123	Offset	129.982	130.006	130.079	130.024
x_ice	162.469	145.787	385.076	136.461	x_ice	142.786	129.544	382.097	125.483
x_water	84.123	224.697	81.662	387.376	x_water	98.357	235.443	84.912	394.074
Sum_X	246.592	370.484	466.738	523.837	Sum_X	241.143	364.987	467.009	519.557
time_ice	0.046	0.041	0.108	0.038	time_ice	0.107	0.097	0.288	0.094
time_water	0.058	0.155	0.056	0.267	time_water	0.068	0.162	0.059	0.272
time_all	0.104	0.196	0.165	0.305	time_all	0.175	0.260	0.346	0.366
Diff_t		0.092	0.061	0.202	Diff_t		0.085	0.171	0.191
							0.156		
Offset	130.002	130.089	130.073	130.123	Offset	129.982	130.006	130.079	130.024
Differenz	0.000	0.087	0.071	1.001	Differenz	0.000	0.024	0.096	1.000
%	0.000	1.001	1.001	0.000	%	0.000	1.000	1.001	0.000
X_ice %	0.659	0.394	0.825	0.261	X_ice %	0.592	0.355	0.818	0.242
X_Water %	0.341	0.606	0.175	0.739	X_Water %	0.408	0.645	0.182	0.758
Time_ice %	0.441	0.210	0.658	0.126	Time_ice %	0.613	0.375	0.831	0.258
Time_Water %	0.559	0.790	0.342	0.874	Time_Water %	0.387	0.625	0.169	0.742

Resulting ray path and travel times, Offset = 247m

pp-wave events					sp-wave events				
Direct Wave	Seafloor	Multiple	Ice_base		Direct Wave	Seafloor	Multiple	Ice_base	
Teta1	60.437	54.347	31.880	46.707	Teta1	48.248	33.890	28.330	24.571
Teta2	20.450	19.050	12.248	17.000	Teta2	53.450	36.900	30.730	26.600
Offset	247.045	247.089	247.088	247.042	Offset	247.067	247.050	247.088	247.029
x_ice	249.297	211.022	433.276	179.373	x_ice	184.711	148.172	417.889	135.247
x_water	86.448	231.689	82.887	398.409	x_water	136.015	273.858	94.232	426.101
Sum_X	335.745	442.710	516.163	577.781	Sum_X	320.726	422.030	512.121	561.348
time_ice	0.070	0.059	0.122	0.050	time_ice	0.139	0.112	0.315	0.102
time_water	0.060	0.162	0.058	0.279	time_water	0.095	0.192	0.066	0.298
time_all	0.130	0.221	0.180	0.329	time_all	0.234	0.303	0.381	0.400
Diff_t		0.091	0.049	0.199	Diff_t		0.069	0.146	0.166
							0.173		
Offset	247.045	247.089	247.088	247.042	Offset	247.067	247.050	247.088	247.029
Differenz	0.000	0.044	0.043	1.000	Differenz	0.000	-0.017	0.021	1.000
%	0.000	1.000	1.000	0.000	%	0.000	1.000	1.000	0.000
X_ice %	0.743	0.477	0.839	0.310	X_ice %	0.576	0.351	0.816	0.241
X_Water %	0.257	0.523	0.161	0.690	X_Water %	0.424	0.649	0.184	0.759
Time_ice %	0.537	0.268	0.677	0.153	Time_ice %	0.594	0.368	0.827	0.255
Time_Water %	0.463	0.732	0.323	0.847	Time_Water %	0.406	0.632	0.173	0.745

Resulting ray path and travel times, Offset = 615m

pp-wave events					sp-wave events				
	Direct Wave	Seafloor	Multiple	Ice_base		Direct Wave	Seafloor	Multiple	Ice_base
Teta1	78.037	76.747	57.800	74.887	Teta1	65.072	56.112	52.590	46.966
Teta2	23.064	22.941	19.807	22.743	Teta2	76.980	63.110	58.582	51.750
Offset	615.004	614.934	615.135	615.165	Offset	614.938	614.987	615.064	615.041
x_ice	593.403	536.529	692.468	471.770	x_ice	291.833	220.601	607.393	180.238
x_water	88.037	237.809	86.093	413.121	x_water	359.535	484.214	155.389	615.415
Sum_X	681.440	774.338	778.562	884.891	Sum_X	651.368	704.815	762.781	795.653
time_ice	0.166	0.150	0.194	0.132	time_ice	0.219	0.166	0.456	0.135
time_water	0.062	0.166	0.060	0.289	time_water	0.251	0.339	0.109	0.430
time_all	0.228	0.317	0.254	0.421	time_all	0.471	0.504	0.565	0.566
Diff_t		0.089	0.026	0.193	Diff_t		0.034	0.094	0.095
							0.277		
Offset	615.004	614.934	615.135	615.165	Offset	614.938	614.987	615.064	615.041
Differenz	0.000	-0.070	0.131	1.000	Differenz	0.000	0.049	0.127	1.000
%	0.000	1.000	1.000	0.000	%	0.000	1.000	1.000	0.000
X_ice %	0.871	0.693	0.889	0.533	X_ice %	0.448	0.313	0.796	0.227
X_Water %	0.129	0.307	0.111	0.467	X_Water %	0.552	0.687	0.204	0.773
Time_ice %	0.730	0.475	0.763	0.314	Time_ice %	0.466	0.329	0.808	0.239
Time_Water %	0.270	0.525	0.237	0.686	Time_Water %	0.534	0.671	0.192	0.761

Resulting ray path and travel times, Offset = 991m

pp-wave events					sp-wave events				
	Direct Wave	Seafloor	Multiple	Ice_base		Direct Wave	Seafloor	Multiple	Ice_base
Teta1	82.671	82.191	68.940	81.547	Teta1	67.389	63.122	62.897	57.069
Teta2	23.305	23.278	21.854	23.238	Teta2	83.360	73.690	73.304	64.570
Offset	991.261	991.040	990.763	991.285	Offset	991.137	991.111	991.045	991.204
x_ice	964.245	905.221	1026.867	836.779	x_ice	319.919	272.066	809.936	226.256
x_water	88.196	238.406	87.272	414.638	x_water	700.506	779.819	281.935	887.268
Sum_X	1052.441	1143.627	1114.139	1251.417	Sum_X	1020.426	1051.886	1091.871	1113.524
time_ice	0.269	0.253	0.286	0.233	time_ice	0.241	0.205	0.609	0.170
time_water	0.062	0.167	0.061	0.290	time_water	0.490	0.545	0.197	0.620
time_all	0.331	0.419	0.347	0.523	time_all	0.731	0.750	0.807	0.791
Diff_t		0.089	0.017	0.193	Diff_t		0.019	0.076	0.060
							0.419		
Offset	991.261	991.040	990.763	991.285	Offset	991.137	991.111	991.045	991.204
Differenz	0.000	-0.220	-0.497	1.000	Differenz	0.000	-0.026	-0.092	1.000
%	0.000	1.000	0.999	-0.001	%	0.000	1.000	1.000	0.000
X_ice %	0.916	0.792	0.922	0.669	X_ice %	0.314	0.259	0.742	0.203
X_Water %	0.084	0.208	0.078	0.331	X_Water %	0.686	0.741	0.258	0.797
Time_ice %	0.813	0.602	0.824	0.446	Time_ice %	0.329	0.273	0.756	0.215
Time_Water %	0.187	0.398	0.176	0.554	Time_Water %	0.671	0.727	0.244	0.785

Resulting ray path and travel times, Offset = 1369m

pp-wave events					sp-wave events				
Direct Wave	Seafloor	Multiple	Ice_base		Direct Wave	Seafloor	Multiple	Ice_base	
Teta1	84.732	84.487	74.552	84.168	Teta1	67.613	65.426	66.405	61.592
Teta2	23.403	23.393	22.611	23.380	Teta2	85.673	78.741	81.216	71.545
Offset	1368.954	1369.041	1369.011	1368.887	Offset	1369.125	1369.066	1369.026	1369.080
x_ice	1339.556	1280.224	1385.324	1210.441	x_ice	322.947	295.770	921.880	258.544
x_water	88.261	238.614	87.744	415.079	x_water	1073.578	1121.671	530.438	1203.564
Sum_X	1427.817	1518.838	1473.068	1625.520	Sum_X	1396.525	1417.441	1452.318	1462.108
time_ice	0.374	0.357	0.386	0.338	time_ice	0.244	0.223	0.695	0.195
time_water	0.062	0.167	0.061	0.290	time_water	0.751	0.784	0.371	0.842
time_all	0.435	0.524	0.448	0.628	time_all	0.994	1.007	1.066	1.037
Diff_t		0.089	0.012	0.193	Diff_t		0.013	0.072	0.042
							0.572		
Offset	1368.954	1369.041	1369.011	1368.887	Offset	1369.125	1369.066	1369.026	1369.080
Differenz	0.000	0.087	0.057	1.000	Differenz	0.000	-0.059	-0.099	1.000
%	0.000	1.000	1.000	0.000	%	0.000	1.000	1.000	0.000
X_ice %	0.938	0.843	0.940	0.745	X_ice %	0.231	0.209	0.635	0.177
X_Water %	0.062	0.157	0.060	0.255	X_Water %	0.769	0.791	0.365	0.823
Time_ice %	0.858	0.682	0.863	0.538	Time_ice %	0.245	0.221	0.652	0.188
Time_Water %	0.142	0.318	0.137	0.462	Time_Water %	0.755	0.779	0.348	0.812

Resulting ray path and travel times, Offset = 1774m

pp-wave events					sp-wave events				
Direct Wave	Seafloor	Multiple	Ice_base		Direct Wave	Seafloor	Multiple	Ice_base	
Teta1	85.955	85.809	78.023	85.626	Teta1	65.953	64.837	65.684	62.584
Teta2	23.616	23.611	23.133	23.605	Teta2	86.906	81.760	85.166	76.080
Offset	1774.778	1774.236	1774.046	1774.407	Offset	1774.177	1774.100	1774.368	1774.374
x_ice	1743.707	1683.006	1778.150	1612.607	x_ice	301.846	289.277	896.134	267.128
x_water	88.404	239.009	88.082	415.791	x_water	1500.716	1528.050	961.151	1583.759
Sum_X	1832.111	1922.015	1866.232	2028.399	Sum_X	1802.562	1817.327	1857.285	1850.887
time_ice	0.483	0.466	0.492	0.446	time_ice	0.227	0.218	0.675	0.201
time_water	0.061	0.165	0.061	0.287	time_water	1.034	1.053	0.662	1.091
time_all	0.544	0.631	0.553	0.733	time_all	1.262	1.271	1.338	1.293
Diff_t		0.087	0.009	0.189	Diff_t		0.009	0.076	0.031
							0.728		
Offset	1774.778	1774.236	1774.046	1774.407	Offset	1774.177	1774.100	1774.368	1774.374
Differenz	0.000	-0.542	-0.733	1.000	Differenz	0.000	-0.077	0.191	1.000
%	0.000	1.000	1.000	0.000	%	0.000	1.000	1.000	0.000
X_ice %	0.952	0.876	0.953	0.795	X_ice %	0.167	0.159	0.482	0.144
X_Water %	0.048	0.124	0.047	0.205	X_Water %	0.833	0.841	0.518	0.856
Time_ice %	0.888	0.739	0.890	0.609	Time_ice %	0.180	0.172	0.505	0.156
Time_Water %	0.112	0.261	0.110	0.391	Time_Water %	0.820	0.828	0.495	0.844